A new set of tethered balloon-borne instrument payloads for collocated turbulence and radiation measurements in the cloudy Arctic boundary layer

First applications

Von der Fakultät für Physik und Geowissenschaften
der Universität Leipzig
genehmigte

D I S S E R T A T I O N

zur Erlangung des akademischen Grades

Doktor der Meteorologie
Dr. rer. nat.

vorgelegt von

Dipl.-Ing. Ulrike Egerer

geboren am 3. Oktober 1988 in Forst/Lausitz

Gutachter: Prof. Dr. Manfred Wendisch

PD Dr. habil. Astrid Lampert

Tag der Verleihung: 20. September 2021

UNIVERSITÄT
LEIPZIG

TROPOS
Leibniz Institute for
Tropospheric Research

Diese Arbeit wurde angefertigt zwischen April 2016 und Juni 2021
am Leibniz-Institut für Troposphärenforschung (TROPOS),
Abteilung Experimentelle Aerosol- und Wolkenmikrophysik,
Permoser Str. 15,
04318 Leipzig.

Diese Arbeit wurde betreut von
Prof. Dr. Manfred Wendisch und Dr. Holger Siebert.

Bibliographische Beschreibung

Egerer, Ulrike
Eine neue fesselballongetragene Instrumentennutzlast für Turbulenz- und Strahlungsmessungen in der bewölkten arktischen Grenzschicht – erste Anwendungen
Universität Leipzig, Dissertation
149 Seiten, 198 Zitate, 60 Abbildungen, 8 Tabellen, 2 Anlagen.

Referat Diese Arbeit stellt das neue Fesselballonsystem *Balloon-bornE moduLar Utility for profilinG the lower Atmosphere* (BELUGA) vor, das für die Messung turbulenter Energie- und Strahlungsflüsse in der bewölkten arktischen atmosphärischen Grenzschicht entwickelt wurde. Mit dem Schwerpunkt auf Turbulenz werden der technische Aufbau und die drei Instrumentenpakete von BELUGA sowie Methoden zur Analyse von Turbulenzdaten beschrieben. BELUGA wurde während zweier Feldkampagnen in der Arktis eingesetzt, die auf dem arktischen Meereis im Juni 2017 und in Grönland im März/April 2018 stattfanden. Anhand zweier Fallstudien liefern die BELUGA-Messungen wertvolle Einblicke in die kleinskaligen turbulenten Prozesse und Strahlungsprozesse, die in der arktischen Grenzschicht wechselwirken. Eine erste Studie analysiert eine Inversion der spezifischen Luftfeuchte über einem beständigen Stratocumulus und die turbulente Kopplung zwischen diesen Regionen. Die Ergebnisse zeigen, dass ein turbulenter Austausch von Wärme und Feuchtigkeit zwischen der Feuchteinversion und der Wolke durch die stabile Inversionsschicht hindurch möglich ist, wenn sich die Feuchteinversion direkt über der Wolkendecke befindet. Die Bereitstellung von Feuchtigkeit durch turbulenten Transport trägt wahrscheinlich zur Langlebigkeit der arktischen Wolken bei. Die zweite Studie befasst sich mit einem Grenzschichtstrahlstrom, d.h. einem lokalen Windmaximum in niedriger Höhe, der in der spätwinterlichen stabilen arktischen Grenzschicht beobachtet wurde. Der Grenzschichtstrahlstrom zeigt eine charakteristische Vertikalstruktur von Turbulenzparametern wie lokalen Dissipationsraten, die direkt ober- und unterhalb des Windmaximums erhöht sind. Daraus folgt, dass das Vorhandensein eines Grenzschichtstrahlstromes die vertikale Durchmischung in der stabilen Grenzschicht unterstützt, was sich auf die vertikale Verteilung von advehierter Feuchtigkeit, Aerosolpartikeln und anderen Substanzen auswirken kann. Beide Fallstudien unterstreichen die Bedeutung der kleinskaligen Turbulenz für die Entwicklung der Grenzschicht in einer stabilen thermodynamischen Schichtung. Damit tragen die BELUGA-Messungen zu einem besseren Prozessverständnis in einer sich verstärkt erwärmenden Arktis mit vielfältigen Rückkopplungsprozessen bei.

Bibliographic description

Egerer, Ulrike
A new set of tethered balloon-borne instrument payloads for collocated turbulence and radiation measurements in the cloudy Arctic boundary layer – first applications
Leipzig University, dissertation
149 pages, 198 references, 60 figures, 8 tables, 2 appendices.

Abstract This thesis introduces the new tethered balloon system *Balloon-bornE moduLar Utility for profilinG the lower Atmosphere* (BELUGA) that has been developed for collocated measurements of turbulent and radiative energy fluxes in the cloudy Arctic atmospheric boundary layer (ABL). With a focus on turbulence, the technical setup and the three instrument packages of BELUGA are presented together with turbulence data analysis methods. BELUGA was deployed during two field campaigns in the Arctic, which took place on Arctic sea ice in June 2017 and in Greenland in March/April 2018. By means of two case studies, the BELUGA measurements provide valuable insights into the small-scale turbulent and radiative processes interacting in the Arctic ABL. A first study analyzes a specific humidity inversion (SHI) above a persistent stratocumulus and the turbulent coupling between these regions. The results show that turbulent exchange of heat and moisture between the SHI and the cloud is possible through the stable inversion layer, when the SHI is located directly above the cloud top. Providing moisture via turbulent transport probably contributes to the persistence of Arctic clouds. The second study addresses a low-level jet (LLJ) observed in the late-winter stable Arctic ABL. The LLJ is associated with a characteristic vertical structure of turbulence parameters such as local dissipation rates, with enhanced intensity just above and below the jet core. It is concluded that the presence of a LLJ promotes vertical mixing in the stable ABL, which can impact the vertical distribution of advected moisture, aerosol particles, and other substances. Both case studies highlight the importance of small-scale turbulence for shaping the ABL under conditions of stable thermodynamic stratification. Thus, the BELUGA measurements contribute to an improved understanding of interacting atmospheric processes in Arctic amplification.

Contents

1 Introduction

The effects of global warming are most pronounced in the Arctic. Arctic near-surface air temperatures have increased more than twice as fast as the global average in the last two decades (IPCC, 2019). Since 2014, each annual surface air temperature mean in the Arctic was the warmest or second-warmest since 1900 (Osborne et al., 2018; Richter-Menge et al., 2019; Ballinger et al., 2020). The increased warming of the Arctic is often referred to as Arctic amplification (AA), although, in a more general sense, the term AA includes all processes that contribute to that warming. For example, in addition to near-surface air temperature, AA is also associated with a steady reduction in sea-ice extent and thickness (IPCC, 2019). After the exceptional record-low in sea-ice summer extent in 2012, the year 2020 almost broke this record (around $40\,\%$ below the 1979-2020 mean for both years; Perovich et al., 2020). The sea-ice loss is accompanied, among other indicators for AA, by mass loss from ice sheets and glaciers, a general decrease in snow cover (IPCC, 2019), and increasing sea-surface temperatures (Timmermans and Labe, 2020). The drastic changes are predicted to proceed at an increasing speed and magnitude (IPCC, 2013; IPCC, 2019). At the same time, the Arctic is particularly vulnerable to the effects of amplified global warming through, e.g., thawing permafrost, increasing economic activities, and growing disaster risks to human settlements (IPCC, 2019). Furthermore, changes in the Arctic climate system do not only impact the Arctic region but are also observed to change mid-latitude weather patterns (Coumou et al., 2018). However, the mechanisms behind these teleconnections are still disputed (Cohen et al., 2020).

In recent years, much progress has been achieved in understanding the mechanisms behind AA, although physical processes driving AA are still not fully understood (Smith et al., 2019; Wendisch et al., 2019). A large part of the literature agrees that local, internal feedback mechanisms, rather than external forcings such as atmospheric or oceanic transport, are the main drivers of AA (Stuecker et al., 2018; Feldl et al., 2020). These feedback mechanisms dampen (negative feedback) or enhance local warming effects (positive feedback). The positive ice-albedo feedback and the lapse-rate feedback have been identified as main contributors to AA (Pithan and Mauritsen, 2014; Goosse et al., 2018). The ice-albedo feedback results from the reduced surface albedo due to the melt of sea ice and snow and a related decrease

in reflected solar radiation, which induces further warming. The lapse-rate feedback results from the bottom-heavy warming in the Arctic close to the surface (due to stable stratification and reduced vertical mixing) compared to rather height-uniform or top-heavy warming at lower latitudes and accelerates Arctic warming compared to the lower latitudes (Boeke et al., 2021). Both the ice-albedo feedback and lapse-rate feedback are affected by the presence and properties of clouds, although the importance of clouds in AA is still disputed: while Pithan and Mauritsen (2014) and Goosse et al. (2018) infer the small magnitude of cloud feedbacks (although being subject to major uncertainties), Tan and Storelvmo (2019) point out the substantial contribution of Arctic mixed-phase clouds to AA. However, clouds modulate the thermodynamic vertical structure and, therefore, influence the effect of the lapse-rate feedback.

A large part of the local atmospheric processes contributing to AA is particularly effective close to the surface, within the atmospheric boundary layer (ABL). The ABL connects the surface with the free troposphere as the lowest part of the atmosphere and is characterized by a specific vertical structure of atmospheric parameters, such as temperature, humidity, and wind, which interact with clouds in the ABL. Compared to lower latitudes, the Arctic ABL exhibits numerous particular features, such as persistent mixed-phase clouds, multiple cloud layers often decoupled from the surface, and ubiquitous temperature inversions (Brooks et al., 2017). Together with radiative properties of clouds, the high albedo of the sea-ice surface leads to a characteristic surface energy budget of turbulence and radiation with comparably low energy fluxes (Persson et al., 2002; Sedlar et al., 2011). The ABL structure exhibits a weak diurnal cycle due to Polar day and night in the winter and summer months, but a pronounced seasonal cycle. The typical summertime Arctic ABL is characterized by neutral to stable stratification with persistent mixed-phase clouds capped by temperature inversions, and ABL heights of $300\,\mathrm{m}$ to $1500\,\mathrm{m}$ (Vüllers et al., 2021). ABL conditions are highly variable when atmospheric low-pressure systems pass. The wintertime Arctic ABL typically includes shallow surface-based temperature inversions with stable stratification throughout. If clouds occur, they are associated with a weak and elevated temperature inversion (Pithan et al., 2016).

Turbulence in the Arctic ABL is one of the mechanisms driving the ABL development and cloud evolution. The ABL is predominantly turbulent since thermodynamic differences between the surface and the free troposphere are balanced by turbulent mixing. However, the Arctic ABL is often stably stratified, and mixing is limited. Vertical turbulent energy transport throughout the ABL is described by the turbulent fluxes of heat, moisture, and momentum. Turbulent fluxes constitute a substantial component of the surface energy budget (Walden et al., 2017). It has been observed

that turbulence processes have a cooling effect on the near-surface Arctic atmosphere during winter and a warming effect during summer (Persson et al., 2002). Moreover, turbulence has a direct effect on clouds and their evolution. For example, turbulent mixing can transport moisture into clouds (Solomon et al., 2014), and turbulence favors ice formation in mixed-phase clouds (Bühl et al., 2019).

Clouds are another critical parameter affecting the atmospheric energy budget of the Arctic. The majority of Arctic clouds are located within the ABL. In particular, persistent low-level, mixed-phase clouds are frequently observed in the Arctic ABL, influencing the thermal stratification, atmospheric radiation, and as a consequence, the entire energy budget (e.g., Sedlar et al., 2011; Shupe et al., 2011). Vice versa, the ABL structure and turbulent motions modify the cloud macrophysical and microphysical structure, resulting in complex cloud–radiation–turbulence interactions. Additionally, long-range transport of moisture, heat and aerosol particles can influence cloud properties (Pithan et al., 2018).

Local ABL and cloud processes in the Arctic ABL are complex and not completely understood. However, they are considered an important component to explain the rapid warming of the Arctic region (Wendisch et al., 2019). The lack of understanding the atmospheric and surface processes involved in AA and their interactions causes major uncertainties in model projections of future Arctic climate changes. In most climate models, turbulent and radiative fluxes at low altitudes are poorly represented, contributing to model uncertainties (Vihma et al., 2014). Tjernström et al. (2021) found that global climate models are erroneous in representing turbulent fluxes, which leads to a biased surface temperature and cloud cover in the Arctic. Also, regional climate models show errors in cloud representation and radiative and turbulent surface energy fluxes in the Arctic (Sedlar et al., 2020). Kay et al. (2016) point out that model results must be combined with observations to understand better the role of clouds in the Arctic climate system.

To provide an observational basis, several comprehensive field campaigns in the Arctic have been carried out (Curry et al., 2000; Uttal et al., 2002; Tjernström et al., 2014; Granskog et al., 2018; Wendisch et al., 2019). Much of the current knowledge is based on observations with research aircraft (e.g., Curry et al., 1988; Tetzlaff et al., 2015) and ground-based remote-sensing measurements (e.g., Sedlar and Shupe, 2014). However, particularly the lowermost levels, including fog or low-level clouds, are difficult to probe with crewed aircraft (Wendisch and Brenguier, 2013). These as well as uncrewed aerial vehicles (UAVs; e.g., Bates et al., 2013; Jonassen et al., 2015; Kral et al., 2020) are mainly limited to cloudless situations due to problems in icing conditions. Ground-based remote-sensing measurements were

used to analyze the interactions between atmospheric radiation and turbulence in Arctic mixed-phase clouds (e.g., Sedlar and Shupe, 2014). These studies are limited to a vertical resolution of typically $45\,\mathrm{m}$. Only very few in-situ, small-scale vertical profile observations from surface to the ABL top exist in the Arctic.

Tethered balloon measurements can bridge the gap between surface-based and aircraft measurements by probing the whole vertical profile of the ABL while providing a high vertical resolution. They are less affected by icing, and measurements inside clouds are possible. Tethered balloons have been deployed successfully in many parts of the Arctic (Lawson et al., 2011; Sikand et al., 2013; de Boer et al., 2018; Dexheimer et al., 2019; Creamean et al., 2021), and during the Arctic Summer Cloud Ocean Study (ASCOS) in the central Arctic (Shupe et al., 2012; Kupiszewski et al., 2013). Duda et al. (1991) and Becker et al. (2018) obtained vertical profiles of irradiances and radiative heating rates from tethered balloon measurements. Canut et al. (2016) showed that it is possible to estimate turbulent fluxes from tethered balloon measurements, although the balloon motion is directly affected by the turbulent wind field. However, so far no combined balloon-borne vertical profile measurements of turbulence and radiation in the Arctic have been reported, although the combined analysis of both processes is vital for understanding the role of clouds in the context of AA.

This thesis introduces the new tethered balloon system called Balloon-bornE moduLar Utility for profilinG the lower Atmosphere (BELUGA) for collocated in-situ measurements of turbulence and broadband solar and terrestrial radiation. BELUGA is capable of providing the vertical profile of turbulence parameters in the cloudy Arctic ABL in combination with radiation and further measurements. The first part of the thesis describes the development and calibration of turbulence instruments for BELUGA and turbulence data analysis. Thereupon, the research focus is the vertical structure of the turbulent Arctic ABL and interactions with clouds. Using the new BELUGA system, small-scale and high-resolution measurements help to analyze local ABL processes. BELUGA was first deployed during the ship-based Arctic field campaign Physical Feedbacks of Arctic Boundary Layer, Sea Ice, Cloud and Aerosol (PASCAL) in June 2017 from an ice floe (Macke and Flores, 2018; Wendisch et al., 2019). In a second campaign, a smaller version of the balloon was used to study the wintertime stable Arctic ABL in northern Greenland during the Polar Airborne Measurements and Arctic Regional Climate Model SImulation Project (PAMARCMiP) 2018. In the framework of this thesis, two ABL features typical for the Arctic have been observed and analyzed: (i) a specific humidity inversion (SHI) above Arctic stratocumulus in the summertime ABL, and (ii) the evolution of a low-level jet (LLJ) in winter. For both cases, the role of turbulence is studied.

SHIs are one of the peculiarities typical for the Arctic ABL. In these inversion layers, the specific humidity increases with height, although specific humidity is generally expected to decrease with altitude in mid-latitude ABLs (Nicholls and Leighton, 1986; Wood, 2012). During PASCAL, a SHI was observed above a persistent stratocumulus in a three-day period. The SHIs are analyzed with respect to potential turbulent coupling with the cloud layer below and turbulent transport of moisture from the SHI into the cloud. The second analyzed Arctic-typical feature is a LLJ, meaning increased wind speed close to the surface. LLJs emerge preferably in stably stratified conditions, which are typical for the Arctic. In the Arctic, LLJs are commonly observed in winter and especially over land (Tuononen et al., 2015). During PAMARCMiP, a LLJ in a stable ABL was observed, with a characteristic vertical profile of turbulence. It is analyzed if wind shear-induced turbulent transport from the LLJ region down to the surface is possible. Both SHIs and LLJs are associated with a particularly stable layer, meaning the temperature and humidity inversion capping a cloud or the stable stratification of LLJ conditions. The present work aims to assess if turbulent transport can be observed despite these stable conditions.

The thesis is structured as follows: chapter 2 introduces the theoretical concepts of turbulence, the Arctic ABL, and measurement techniques for turbulence. Chapter 3 presents the technical specifications of the new BELUGA system, followed by the turbulence data analysis methods in chapter 4. Chapter 5 introduces the two field campaigns, where BELUGA was operated and presents exemplary observations from these campaigns. In a first case study (chapter 6), I analyze a persistent SHI above a cloud and their turbulent coupling. The second case study (chapter 7) addresses the turbulence structure of a LLJ. Finally, chapter 8 gives a summary and discusses the limitations and potential for future deployment of BELUGA.

2 Background

This chapter provides some background about turbulence in the Arctic ABL and how it is measured. First, I summarize theoretical concepts of turbulence covering the characteristics of turbulent flows and selected turbulence analysis methods. Next, the concept of the ABL is explained concerning stability, turbulence, and clouds, and the special characteristics of Arctic ABLs are highlighted. Finally, different measurement approaches for turbulence observations in the Arctic ABL are reviewed.

2.1 Fundamental aspects of turbulence

2.1.1 The nature of turbulent flows

Turbulence is the term used to describe the small-scale contributions to atmospheric motions, or more precisely, the fluctuations superimposed on the mean flow. The basic principles of turbulence theory described in this section date back to the late 19th and early 20th century (Reynolds, 1895; Richardson and Shaw, 1920; Taylor, 1938; Kolmogorov, 1941b). Much of the pioneering work, such as Kolmogorov's hypotheses, has been confirmed in the Kansas experiments in 1968 (Kaimal et al., 1972). Since then, significant progress has been achieved in studying turbulent flows, but some problems remain unsolved. The fundamental principles of turbulence are presented here as a basis for the turbulence analysis of this work's observations.

Turbulence commonly refers to fluctuations of the wind velocity vector $\vec{u} = (u, v, w)$, although the principles also apply to the air temperature T, specific humidity q, and other quantities. The turbulent fluctuations can be interpreted as eddies of different sizes coexisting in a turbulent flow. Turbulent fluctuations are of random, non-linear, three-dimensional nature (Batchelor, 1953) and cannot be predicted in detail. A complete deterministic description of turbulence is still an unsolved problem. However, statistical properties of turbulent flows are reproducible (Frisch, 1995) and, therefore, turbulence can be described statistically (Taylor, 1935; Tennekes and Lumley, 1972).

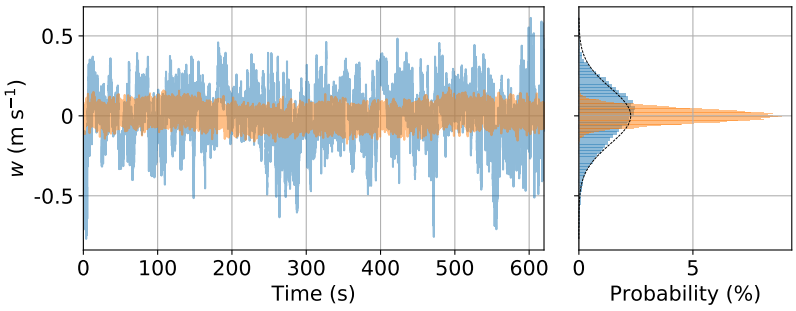

Fig. 2.1.: Time series and probability distribution of a turbulent (blue) and low-turbulence (orange) flow with the vertical wind velocity w.[1] For the distribution of the turbulent fluctuations, a Gaussian approximation is added as a black dotted line.

A component of a turbulent flow u depending on space x and time t can be decomposed into an average (marked with an overline) and the fluctuating deviation from the average (marked with a prime):

$$u(x,t) = \overline{u} + u'(x,t) \tag{2.1}$$

with $\overline{u'(x,t)} = 0$, which is known as Reynolds decomposition (Stull, 1988). It is crucial how the average $\overline{u}$ is determined. Temporal and spatial averages are possible with the aim of approximating an ensemble average (Batchelor, 1953; Pope, 2000). Further, the average must include sufficient data points to achieve statistical convergence (Lenschow et al., 1994).

The probability distribution of the velocity fluctuations $u'(x,t)$ characterizes the turbulent flow (Tennekes and Lumley, 1972). The turbulence properties can be described by the statistical moments of the probability distribution mean, variance, skewness, and kurtosis. Figure 2.1 shows an exemplary time series of the vertical wind velocity w in a turbulent and a low-turbulence flow and the corresponding probability distribution. In the turbulent flow, the amplitude and frequency of fluctuations vary irregularly. The low-turbulence case shows much less variation in magnitude and frequency, which results in a narrower probability distribution. The turbulent fluctuations are distributed around a maximum value close to the average $\overline{w} \approx 0\,\mathrm{m\,s^{-1}}$. The variance of the turbulent flow ($\sigma_w^2 = 0.03\,\mathrm{m^2\,s^{-2}}$) is larger than the variance of the low-turbulence flow ($\sigma_w^2 = 0.002\,\mathrm{m^2\,s^{-2}}$). The probability distribution of the turbulent flow velocity slightly deviates from a Gaussian distribution with a non-zero skewness of -0.46.

[1] The data are 10-minute constant-altitude segments from the PASCAL campaign, 5 June 2017, at $10\,\mathrm{m}$ and $750\,\mathrm{m}$ altitude (Sect. 5.1.2) with a mean horizontal wind of $1.7\,\mathrm{m\,s^{-1}}$ and $0.8\,\mathrm{m\,s^{-1}}$, respectively.

Assumptions for describing turbulent flows Describing a particular turbulence problem, such as atmospheric turbulence, usually requires some simplifying assumptions, which should be assessed carefully before applying turbulence analysis methods. The most commonly applied assumptions are briefly described below.

- In a *stationary* turbulent flow, the statistical properties of the turbulent fluctuations are independent of time (Garratt, 1994). Stationarity in atmospheric turbulence can only be assumed for a short time period in the order of minutes (Foken, 2003).

- In a *homogeneous* flow, the statistical properties do not depend on space (Batchelor, 1953). This does not apply for large scales in the vertically stratified ABL, but horizontal homogeneity might be assumed within defined areas (Garratt, 1994).

- In an *isotropic* flow, the statistical properties of turbulence parameters are generally independent of their direction: $\sigma_u^2 = \sigma_v^2 = \sigma_w^2$ (Tennekes and Lumley, 1972). In practice, atmospheric turbulence at large scales is predominantly anisotropic (e.g., Lovejoy et al., 2007) due to the surface's influence and buoyancy (Garratt, 1994; Biltoft, 2001). When these effects can be neglected, the flow is assumed to be locally isotropic. However, for local isotropy in the inertial subrange (cf. Sect. 2.1.2) the turbulent fluctuations in this region scale as $\sigma_v^2/\sigma_u^2 = \sigma_w^2/\sigma_u^2 = 4/3$ (Kolmogorov, 1941a), which is confirmed by several observations (Kaimal et al., 1972; Siebert et al., 2006; Nowak et al., 2021). In general, strongly turbulent flows are rather isotropic than less turbulent flows (Mauritsen and Svensson, 2007).

- In a stationary and homogeneous flow, the time coordinate t can be easily transferred into a spatial coordinate x (Taylor, 1938):

$$x = \overline{u} \cdot t\,. \tag{2.2}$$

  This is particularly useful when a spatial average is needed, but the measurement setup allows only time averages. The assumption is known as *Taylor's frozen flow hypothesis* and applies for low-turbulence ($u' \ll \overline{u}$), approximately stationary and homogeneous flows (Garratt, 1994). Close to the surface, the hypothesis might not be applicable (Cheng et al., 2017) because the convection velocity of different-sized eddies varies.

Turbulent kinetic energy A turbulent flow has a specific amount of turbulent kinetic energy (TKE), which is a measure of turbulence intensity. The TKE is defined by the variance of the wind velocity vector components σ^2 (Garratt, 1994):

$$\mathrm{TKE} = 0.5 \cdot \left(\sigma_u^2 + \sigma_v^2 + \sigma_w^2\right). \tag{2.3}$$

The variances are averaged over a defined time period. The length of the averaging interval must be large enough to include enough low-frequency fluctuations contributing to the TKE (cf. Sect. 4.2.1).

The TKE budget equation includes different processes that generate or reduce turbulence (Stull, 1988). For increasing the TKE, turbulence can be generated mechanically by wind shear or convectively by buoyancy. The shear production term in the TKE budget (with u being aligned with the mean horizontal wind and w in vertical direction) is given by:

$$\left(\frac{\partial\,\mathrm{TKE}}{\partial\,t}\right)_{\mathrm{s}} = -\,\overline{u'w'} \cdot \frac{\partial \overline{u}}{\partial z} \tag{2.4}$$

and results from the interaction of the covariance $\overline{u'w'}$ with the vertical wind velocity gradient $\partial\overline{u}/\partial z$. Wind shear usually results in production, not loss, of turbulence. The buoyant production or consumption term

$$\left(\frac{\partial\,\mathrm{TKE}}{\partial\,t}\right)_{\mathrm{b}} = \frac{g}{\overline{\theta}_v} \cdot \overline{w'\theta_v'} \tag{2.5}$$

with the acceleration of gravity g and virtual potential temperature θ_v is negative or positive depending on the sign of the covariance of w' and θ_v'. The present work will address these two terms. Additionally, turbulence decays by molecular diffusion at the TKE dissipation rate ε and can be transported with the mean wind. For a complete quantitative description of the TKE budget, I refer the reader to, e.g., Stull (1988).

Scales in atmospheric flows The turbulent energy in the atmosphere is not distributed equally over the eddy sizes of the flow. Instead, the energy in the ABL extends over a wide range (several orders of magnitude) of length and time scales from mesoscale influences up to the size of the ABL depth down to small-scale turbulence in the range of millimeters (Stull, 1988). Beyond that, the atmosphere includes synoptic scales (e.g., weather systems) and planetary scales (e.g., Rossby waves). Each scale is associated with a characteristic amount of kinetic energy. Most of the energy is concentrated on the synoptic and turbulent scales (Fig. 2.2). Synoptic scales and turbulent scales are often, but not always, separated by a spectral gap at

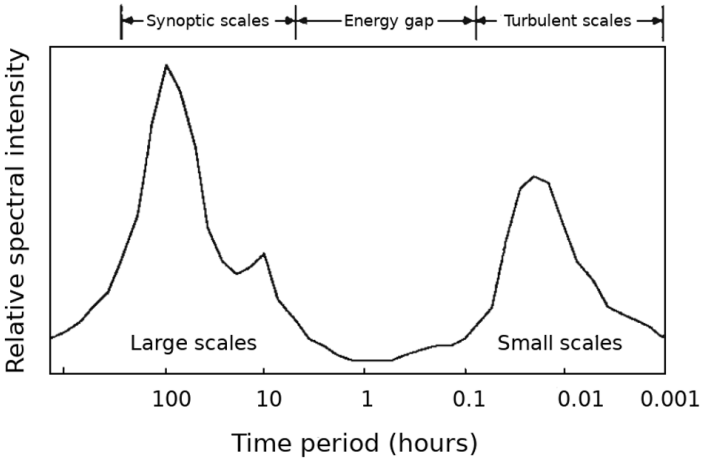

Fig. 2.2.: Schematic spectrum of wind speed on synoptic and turbulent scales with a spectral gap in between. Adapted from Van der Hoven (1957) and Stull (1988).

the mesoscales (Van der Hoven, 1957; Stull, 1988). Especially in the summertime Arctic, the spectral gap is rather a plateau, and mesoscale influences like gravity waves or front-like systems directly influence turbulent motions (Mauritsen, 2007).

2.1.2 Turbulent energy spectrum

The present work focuses on the turbulent part of the energy spectrum. The spectral analysis provides additional conclusions on how the energy is distributed across the eddy sizes and how the energy is exchanged. The exchange of energy is characteristic of a turbulent flow and is known as the energy cascade or Richardson cascade (Richardson, 1922). Triggered by larger scales beyond turbulence, energy is introduced into a turbulent flow at the largest turbulent scales of eddy sizes (Foken, 2003). Inertial forces cause that energy transfers from larger to smaller eddies, just as Lewis F. Richardson described in a poem in 1922:

> *Big whorls have little whorls*
> *Which feed on their velocity,*
> *And little whorls have lesser whorls*
> *And so on to viscosity.*

This is a multistage, nonlinear process: instability in few big eddies produces more smaller eddies down to molecular scales (Garratt, 1994). Finally, the kinetic energy of the smallest eddies is converted into heat by viscous energy dissipation.

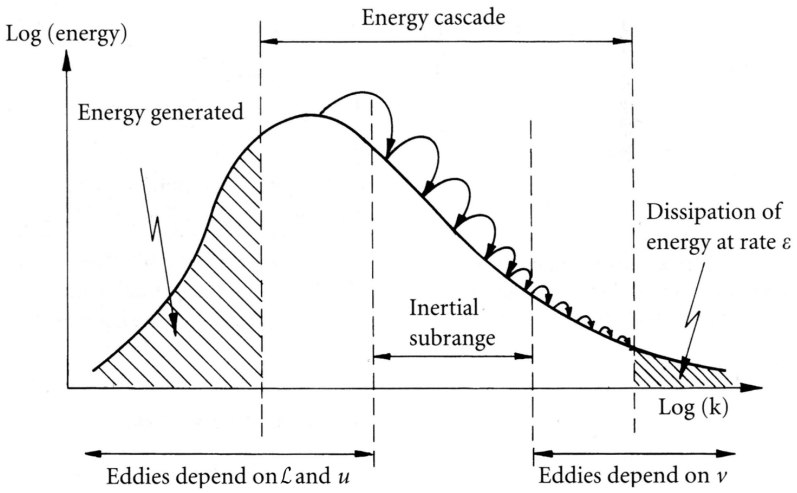

Fig. 2.3.: Schematic representation of the energy cascade: turbulent kinetic energy depending on the wave number k. At the large scales, the eddies depend on the integral length scale $\mathcal{L}$ and the flow velocity u; at the small scales, the eddies depend solely on the kinematic viscosity ν and energy dissipation ε. Modified after Davidson (2004).

The energy spectrum of a turbulent flow allows analyzing the different eddy sizes contained in the flow and their respective spectral energy. The velocity fluctuations in a flow are translated from the spatial or temporal space into the spectral space via a Fourier transform. For the energy spectrum, the spectral energy E contained by an eddy is assigned to its frequency f or to its wave number

$$k = \frac{2\pi \cdot f}{\overline{u}}\,, \tag{2.6}$$

which can be interpreted as the spatial frequency. A schematic of a turbulence energy spectrum with the energy cascade is shown in Fig. 2.3. The schematic can be divided into three characteristic scales (timescales/ frequency ranges or spatial scales/ eddy sizes): large scales around the integral length scale $\mathcal{L}$ at low wave numbers, the Kolmogorov scale η at highest wave numbers and the inertial subrange (or Taylor microscales) for $\mathcal{L}^{-1} \ll k \ll \eta^{-1}$. These characteristic scales are discussed in more detail below.

The energy is introduced to the integral scales with eddy sizes of typically $10\,\mathrm{m}$ to $500\,\mathrm{m}$ (Kaimal and Finnigan, 1994), where kinematic forces dominate. The greatest part of the spectral turbulent energy is concentrated on the integral scales in a range of $0.17\mathcal{L}$ to $6\mathcal{L}$ (Pope, 2000). $\mathcal{L}$ describes the typical size of the largest turbulent eddies in a flow, knowledge of which is crucial for further turbulence analysis. Integral length scales are related to integral time scales via Taylor's frozen

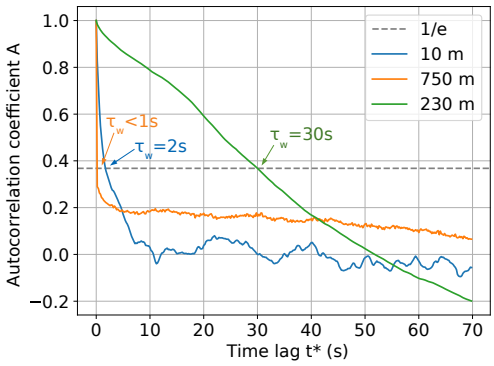

Fig. 2.4.: Autocorrelation function for three exemplary time series of w recorded in different heights.[2] The derived integral time scales τ_w are shown for each time series.

flow hypothesis. The integral time scale (over which a process is highly correlated with itself) can be analyzed with the autocorrelation function

$$A(t^*) = \frac{\overline{u(t)' \cdot u(t+t^*)'}}{\sigma_u^2} \tag{2.7}$$

for a wind velocity component u at time t and shifted by a time lag t^*. The integral time scale τ_u is equal to the integral of the autocorrelation function

$$\tau_u = \int_0^\infty A(t^*)\,\mathrm{d}t^*. \tag{2.8}$$

Usually, the autocorrelation function is analyzed in the temporal space (because of measurements in this domain), but via Eq. (2.2), the integral time scale can be transformed into an integral length scale $\mathcal{L}$. Figure 2.4 gives an example for observed autocorrelation coefficients for the vertical wind velocity w and how the integral time scale τ_w can be derived from the autocorrelation function. As an approximation for Eq. (2.8), τ_w equals the time when the autocorrelation coefficient reaches $A = 1/e$. Non-convergence of the autocorrelation function $(\lim_{t^*\to\infty} \neq 0)$ might result from instationarity or inhomogeneity of the flow (Tennekes and Lumley, 1972) or a trend in the time series.

In the inertial subrange between the integral and Kolmogorov scales, the turbulent flow neither depends on the energy intake nor on the viscosity (Tennekes and Lumley, 1972; Stull, 1988). Instead, the energy spectrum in the inertial subrange has the universal form

$$E(k) = \alpha \cdot \varepsilon^{2/3} \cdot k^{-5/3} \tag{2.9}$$

[2]The data are 10-minute constant-altitude segments as in Fig. 2.1, plus an additional segment in 230 m height.

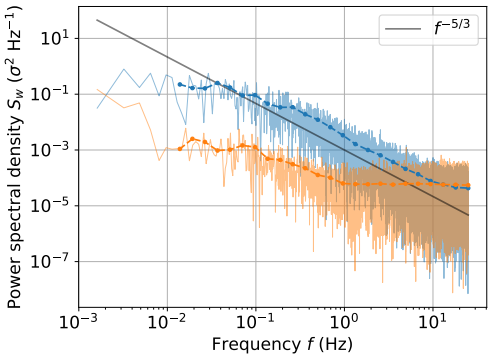

Fig. 2.5.: Power spectral density of vertical wind velocity w for a turbulent (blue) and low-turbulence (orange) flow.[4]

(Kolmogorov, 1941b; Batchelor, 1953) with the energy dissipation rate ε and the Kolmogorov constant for the longitudinal wind velocity $\alpha \approx 0.5$ (Yeung and Zhou, 1997; Högström et al., 2002). This means that in the inertial subrange, the spectrum depends solely on ε. In the double-logarithmic representation of the energy spectrum for a turbulent flow, the inertial subrange features a constant -5/3 slope (Wyngaard, 2010)[3]. In stationary turbulence, the rate of energy input at inertial scales is equal to the energy dissipation at rate ε (Pope, 2000).

At the Kolmogorov scales (at high wave numbers), viscous forces dominate among the smallest eddies. Kolmogorov (1941b) hypothesized that for very high Reynolds numbers the statistics of small scales depend only on the kinematic viscosity ν and ε. This results in the Kolmogorov length scale $\eta = (\nu^3/\varepsilon)^{1/4}$, which is in the order of millimeters for atmospheric conditions (Foken, 2003). According to Kolmogorov's similarity theory (Kolmogorov, 1941b; Pope, 2000), local isotropy and homogeneity can be assumed for an equilibrium range of frequencies, which includes the inertial subrange and Kolmogorov scales.

The concept of the energy spectrum allows for a wide range of applications. The turbulent energy spectrum derived from observations can be applied as a tool to (i) characterize the flow in terms of turbulence and (ii) evaluate the performance of the measurement setup. This will be demonstrated through spectra for the time series in Fig. 2.1. Figure 2.5 shows the turbulence energy spectra $S_w(f)$ for the observed time series. The smoothed spectra result from averaging over logarithmic equidistant bins. The power spectral density (PSD) for the turbulent flow exhibits the characteristic -5/3 slope in the inertial subrange between 10^{-1} Hz and 10^{1} Hz.

[3] In addition to wind velocity, relations similar to Eq. (2.9) are formulated for the energy spectrum of temperature and humidity in the form of $E \propto \varepsilon^{-1/3} \cdot k^{-5/3}$ (Foken, 2003).
[4] Same data basis as in Fig. 2.1.

At lower frequencies, the curve flattens. However, for a statistically robust behavior at the integral scales, a longer averaging time is needed to include more lower-frequency eddies. The low-turbulence flow shows a constant PSD for frequencies greater than $1\,\mathrm{Hz}$ and a slope <-5/3 at lower frequencies. The spectral energy $S(f)$ averaged over all frequencies (or analog for $E(k)$ over all k) equals the variance of the respective wind velocity component:

$$\sigma^2 = \int_0^\infty S(f)\,\mathrm{d}f. \tag{2.10}$$

The spectra in the example case show clearly that the variance of the low-turbulence flow is smaller than that of the turbulent flow.

As a second application, the spectrum derived from measurements reveals the resolution limit of the instrument. The smallest resolved scales depend on the measurement resolution. The PSD plateau (the spectral noise floor) at $f > 10^1\,\mathrm{Hz}$ in Fig. 2.5 results from observed turbulent scales smaller than the instrument resolution. With a spectral noise floor (indicated by $^{(\mathrm{n})}$) of $S_w^{(\mathrm{n})} \approx 4\times10^{-5}\sigma^2\,\mathrm{Hz}^{-1}$ and a Nyquist frequency (half the sampling frequency) of $f_{\mathrm{Ny}} = 25\,\mathrm{Hz}$, the standard deviation due to uncorrelated noise

$$\sigma_w^{(\mathrm{n})} = \sqrt{S_w^{(\mathrm{n})} \cdot f_{\mathrm{Ny}}} \tag{2.11}$$

yields $\sigma_w^{(\mathrm{n})} \approx 0.03\,\mathrm{m\,s^{-1}}$ for the example case.

2.1.3 Structure function and dissipation rate

The energy dissipation rate is of central importance to describe turbulent flows since the spectrum in the inertial subrange is uniquely defined by ε (Kolmogorov, 1941b; Pope, 2000) and the rate of energy dissipation at small scales in a turbulent flow equals the energy input at large scales (Davidson, 2004). One aim of this work is to derive vertical profiles of dissipation rates to describe the ABL structure. Muschinski et al. (2004) and Siebert et al. (2006) discuss different methods to estimate local dissipation rates from airborne in-situ measurements. The methods include, among others, deriving ε from the energy spectrum (Eq. 2.9), the relation between the spectrum and the variance (Eqs. 2.10 and 2.9) at inertial scales, and finally, the structure functions. Structure functions are based on the velocity increment $u(x+r) - u(x)$ between two spatial points separated by the distance r (Davidson, 2004). The structure functions of n^{th} order are the statistical moments n of the flow velocity increments:

$$D^n(r) \equiv \overline{[u(x+r) - u(x)]^n}\,. \tag{2.12}$$

In the inertial subrange, and assuming homogeneous, isotropic, and stationary turbulence, the structure functions scale with r in the form of

$$D^n(r) = C_n \cdot \varepsilon^{n/3} \cdot r^{n/3} \tag{2.13}$$

(Kolmogorov, 1941b; Pope, 2000) with a universal constant C_n, which depends on n and the applied wind vector component. Applying the Taylor hypothesis (Eq. 2.2), the spatial distance r can be transformed into the temporal scale. By evaluating the structure function for a time series of a flow velocity component, the dissipation rate can be retrieved. Mean dissipation rates are related to the average over long time series. In contrast, local dissipation rates are averaged over shorter intervals and, thus, consider intermittency, meaning the small-scale structure of turbulence (Kolmogorov, 1962; Obukhov, 1962). Siebert et al. (2006) concluded that the second-order structure function provides the most robust results for estimating local dissipation rates from observational data.

In this work, the second-order structure function in the temporal space

$$D^2(t^*) \equiv \overline{[u(t-t^*) - u(t)]^2}_\tau = C_2 \cdot \varepsilon_\tau^{2/3} \cdot \left(t^* \cdot \overline{U}_\tau\right)^{2/3} \tag{2.14}$$

with $C_2 \approx 2$ for the longitudinal flow component is applied to estimate the local dissipation rate ε_τ in a time period τ. Averaged parameters in Eq. (2.14) are indicated by an overline and index τ, $u(t)$ is the horizontal wind velocity at the time t, t^* is a time lag, and U is the mean horizontal wind. For each time period τ, the structure function on the left side of Eq. (2.14) is evaluated for time lags t^* in an empirical time range. Fitting this curve to the right side of the equation yields ε_τ for each time period. Knowing ε_τ allows for describing the turbulent structure of a flow.

2.1.4 Turbulent fluxes

The eddies in a turbulent flow are capable of transporting heat, momentum, moisture, and other precursors (Stull, 1988). In the atmosphere, this turbulent transport occurs predominantly in vertical direction[5] and attempts to counterbalance vertical gradients. Turbulent transport is described by the covariance of vertical wind velocity w with a second quantity (e.g., T, q, or u), averaged over a certain time period. This

[5] In the horizontal direction, advective fluxes dominate.

yields the turbulent fluxes of sensible heat H_S, latent heat L and momentum τ_{uw}, which express the vertical exchange of heat, moisture, and momentum:

$$H_{\mathrm{S}} = \overline{\rho} \cdot \mathrm{c_p} \cdot \overline{w'\,\theta'} \tag{2.15}$$

$$L = \overline{\rho} \cdot L_{\mathrm{v}} \cdot \overline{w'\,q'} \tag{2.16}$$

$$\tau_{\mathrm{uw}} = -\overline{\rho} \cdot \overline{w'\,u'} \tag{2.17}$$

with the mean air density $\overline{\rho}$, potential temperature θ, the specific heat capacity of air $\mathrm{c_p} = 1005\,\mathrm{J\,kg^{-1}\,K^{-1}}$, and the latent heat of evaporation $L_{\mathrm{v}} = 2.5 \times 10^6\,\mathrm{J\,kg^{-1}}$. The covariances, as second-order statistical moments, are unknowns in the Navier Stokes equations to describe a turbulent flow. These equations cannot be solved analytically (this is called the turbulence closure problem). Therefore, they must be parameterized (Mellor and Yamada, 1974). To verify and improve the parameterizations, experimental evaluations of turbulent fluxes are of great value.

A widely-applied turbulence closure scheme is the gradient transport theory (e.g., Stull, 1988). This method derives vertical flux profiles from local mean gradients. Based on the classical boundary layer theory (Stull, 1988), the turbulent energy fluxes are related to the vertical mean gradients of the respective parameter x by:

$$\overline{w'x'} = -K_{\mathrm{x}} \cdot \frac{\partial \overline{x}}{\partial z} \tag{2.18}$$

with K_{x} being the turbulent exchange coefficient. The coefficients K_{x} are defined as positive, which means that the flux is directed against the mean gradient. Turbulent transport by very large eddies might result in counter-gradient fluxes; thus, the gradient theory is rather suitable for flows dominated by small eddies (e.g., stable ABLs; Stull, 1988; Garratt, 1994). The exchange coefficient for momentum K_{m} is a function of stability and the flow itself and is assumed to be zero without turbulence while increasing with TKE (Stull, 1988). There exist various parameterizations for K_{m} (an overview is provided by Bhumralkar, 1976). For example, Hanna (1968) suggest relating K_{m} to basic turbulence parameters:

$$K_{\mathrm{m}} = \mathrm{C} \cdot \frac{\sigma^4}{\varepsilon} \tag{2.19}$$

with C = 0.35. The turbulent Prandtl number $\mathrm{Pr_t} = K_{\mathrm{m}}/K_{\mathrm{H}}$ relates the exchange coefficients of momentum and heat. The Prandtl number is a function of vertical thermodynamic stability, but ranges from 0.5 to 1 (Li, 2019). Here, we consider $\mathrm{Pr_t} \approx 0.7$ as suggested by Stull (1988). For heat and moisture, it has been shown that

$K_\mathrm{H} \approx K_\mathrm{Q}$ (Dyer, 1967) for a wide range of stratification. Finally, after calculating K_H and K_Q from K_m, the turbulent fluxes result from

$$H_\mathrm{S} = -\,\overline{\rho} \cdot \mathrm{c_p} \cdot K_\mathrm{H} \cdot \frac{\partial \overline{\theta}}{\partial z}, \tag{2.20}$$

$$L = -\,\overline{\rho} \cdot L_\mathrm{v} \cdot K_\mathrm{Q} \cdot \frac{\partial \overline{q}}{\partial z}, \text{ and} \tag{2.21}$$

$$\tau_\mathrm{uw} = \overline{\rho} \cdot K_\mathrm{m} \cdot \frac{\partial \overline{u}}{\partial z}. \tag{2.22}$$

The vertical profiles of turbulent fluxes, as described by means of the gradient transport theory, significantly shape the structure of the ABL, which will be introduced in the next section.

2.2 The atmospheric boundary layer (ABL)

2.2.1 General concepts

The ABL represents the lowermost part of the atmosphere, connecting the surface with the free troposphere. Garratt (1994) defines the ABL as "the layer of air directly above the Earth's surface in which the effects of the surface (friction, heating, and cooling) are felt directly on time scales less than a day". The ABL can be further divided into the outer (Ekman) layer and the lowest $10\,\%$ of the ABL as the inner (Prandtl) surface layer, where the flow mainly depends on the surface (Foken, 2003). However, the surface influences the entire ABL, for example, thermodynamically through surface heating or cooling and mechanically through surface friction. The vertical temperature profile in the ABL plays a crucial role for its characteristics. Usually, the temperature is thought to decrease with height by the dry or cloud adiabatic lapse rate (neutral thermodynamic stratification). If the temperature decreases less with height or even increases in a region, we refer to this layer as stably stratified. If the temperature decreases at a higher rate, the layer is instable (convective), and mixing is favored. The thermodynamic stability is described by height-conserved variables such as the potential temperature

$$\theta = T \cdot \left(\frac{p_0}{p}\right)^{R_\mathrm{d}/c_\mathrm{p}} \tag{2.23}$$

with the barometric pressure p, the near-surface pressure p_0, and the specific gas constant of dry air $R_\mathrm{d} = 287\,\mathrm{J\,kg\,K^{-1}}$. The ABL is usually capped by a more or less pronounced, stable temperature inversion, which in some cases also caps a cloud in

the ABL. The ABL height varies from a few tens of meters to a few kilometers (Stull, 1988), mainly depending on the stability of the ABL.

The ABL is generally turbulent over a wide range of scales from ABL depth down to the millimeter scale (Garratt, 1994). The turbulent motions allow the ABL to respond to surface forcings and transport heat, moisture, and momentum vertically within the ABL via turbulent energy fluxes. To characterize the turbulent ABL, turbulent and low-turbulent regions might be distinguished by the Richardson number Ri (based on Richardson and Shaw, 1920). This number represents the ratio of buoyancy conversion/ production (with the Brunt-Väisälä frequency N) to wind shear production S:

$$\mathrm{Ri} = \frac{N^2}{S^2} = \frac{g}{\overline{\theta}} \cdot \frac{\partial\theta/\partial z}{(\partial U/\partial z)^2}. \tag{2.24}$$

with the vertical potential temperature gradient $\partial\theta/\partial z$. The gradient Richardson number Ri_g is based on the actual height-dependent temperature and wind velocity gradients. The bulk Richardson number Ri_b refers to temperature and wind differences between the surface and a defined height (Garratt, 1994). Many studies in stable ABLs refer to the surface-referenced Ri_b (e.g., Vickers and Mahrt, 2004; Banta, 2008; Emeis, 2017). The classical approach is that turbulence decays when stratification dominates over shear, thus when $\mathrm{Ri} > \mathrm{Ri}_c$. The critical Richardson number Ri_c was estimated to values between 0.25 and 1 (Miles, 1961; Abarbanel et al., 1984). More recent research suggests that weak turbulence can exist beyond Ri_c (Galperin et al., 2007; Mauritsen and Svensson, 2007). Mahrt et al. (1998) and Mauritsen and Svensson (2007) also classify the dynamic stability based on Ri: very stable flows for Ri>1 (no or low turbulence) and weakly stable flows for Ri<0.1 with a transition zone for 0.1<Ri<1. Further, there seems to exist a hysteresis for Ri_c, depending on whether the transition takes place from stable to turbulent conditions or vice versa (Emeis, 2017).

Figure 2.6 shows an example for vertical profiles of potential temperature, wind speed, and Ri_b for a strongly stable ABL. The temperature profile exhibits a surface-based temperature inversion with less stable stratification above. Because of the strong wind shear inside the inversion layer, the Ri_b is below Ri_c in this layer, and turbulent motions are possible. Above, the stable stratification dominates, and turbulence is suppressed.

The characteristic stratification of a convective ABL and a typical flux profile are shown in Fig. 2.7. The surface layer with instable stratification and the overlying mixed layer with neutral stratification are capped by a stable temperature inversion.

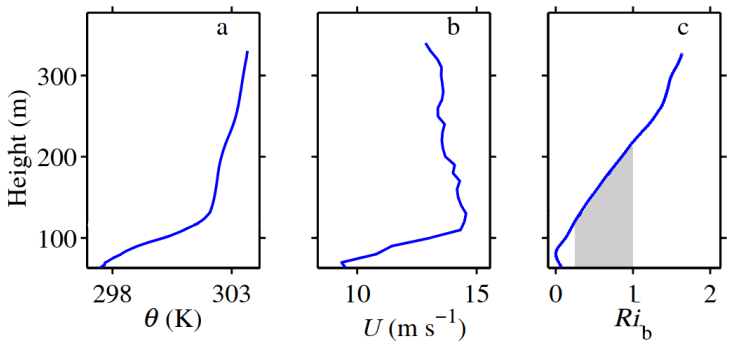

Fig. 2.6.: Example vertical profiles of a strongly stable ABL: **(a)** potential temperature θ, **(b)** horizontal wind speed U, and **(c)** bulk Richardson number Ri_b. The grey shaded area in panel **(c)** denotes the range for $0.25 < \mathrm{Ri}_c < 1$. Modified after Zhang et al. (2014).

The schematic adds the vertical structure of the turbulent sensible heat flux, representing the turbulent exchange of heat energy between the different layers. In the mixed layer, the fluxes are upward directed (positive sign) with maximum values at the surface. The inversion layer is typically associated with a weak downward (negative) flux, which entrains warm air from above the temperature inversion. Above the entrainment zone, the fluxes vanish. In contrast to a convective ABL, the fluxes in stable ABLs are very weak throughout the profile, or idealized zero, with only a small downward flux in the surface-based temperature inversion (Stull, 1988). Generally, turbulent fluxes impact the the ABL less under stable conditions than under instable conditions.

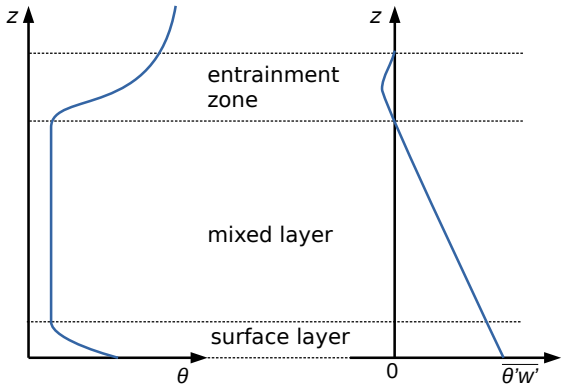

Fig. 2.7.: Typical vertical structure of θ and sensible heat flux $\overline{\theta' w'}$ in a convective ABL. Modified after Driedonks and Tennekes (1984).

2.2.2 Clouds in the ABL

Another key player in shaping the ABL are clouds, which can form at the top of mixed layers in convective ABLs or at the bottom of stable ABLs (Stull, 1988). Clouds in the ABL modify the surface energy budget by reflecting shortwave solar radiation and absorbing or emitting terrestrial longwave radiation (Wild et al., 2019). Depending on the geographic region, season and cloud type and height, they may have a warming or cooling effect on the surface (quantified as the cloud radiative forcing; L'Ecuyer et al., 2019) and hence on the ABL structure.

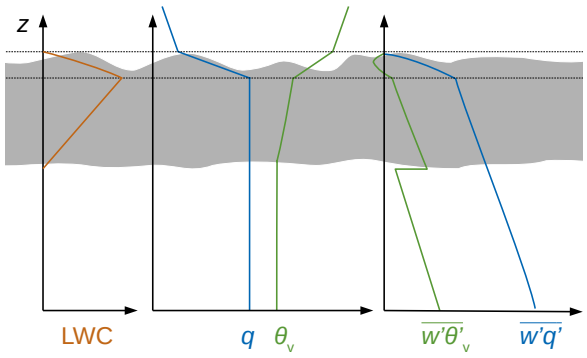

Fig. 2.8.: Idealized vertical profiles of liquid water content (LWC), virtual potential temperature θ_v, specific humidity q, and their turbulent fluxes in a cloudy ABL. Redrawn after Deardorff (1976) and Stull (1988).

One of the most common cloud types in the ABL is stratocumulus, covering large parts of the earth's surface (Wood, 2012). These are convective clouds capped by temperature inversions (Stull, 1988). Figure 2.8 shows idealized vertical profiles in a stratocumulus. Cloud top and bottom are no clear boundaries. Instead, they are heterogeneous and instationary. The amount of liquid water in the cloud, the LWC, is highest near the cloud top and decreases linearly to zero towards the cloud base. Specific humidity and virtual potential temperature are almost constant between the surface and cloud top, but change abruptly within the cloud top region. The sensible heat flux is increased inside the cloud and exhibits a downward flux at the cloud top. The latent heat flux decreases with height. Above the cloud top, both fluxes vanish, and turbulence is expected to decay (Deardorff, 1976).

At the top of the cloud layer, the cloud water droplets radiate to the free atmosphere above, which is known as cloud-top (longwave) radiative cooling (Garratt, 1994). The cloud-top downward heat flux compensates the radiative cooling (Deardorff, 1976). Here, warm and dry air from above the cloud is entrained into the cloud layer. Together with wind shear and buoyancy, cloud-top cooling is a driver of turbulence in the cloud.

By directly influencing the vertical profile of turbulent fluxes, clouds modify the thermal stratification in the ABL. Apart from cloud-radiation-turbulence interactions, evaporation at cloud top, microphysical processes, and precipitation increase clouds' complexity. The idealized case above is typical for mid-latitude clouds. However, clouds play a crucial role in the Arctic ABL, which will be discussed in the next section.

2.2.3 Characteristics of the Arctic ABL

The Arctic ABL differs from lower-latitude ABLs in several ways. It is generally more stable and frequently exhibits one or more temperature inversions (Tjernström et al., 2019). Due to limited mixing in stable ABLs, the Arctic ABL is also vertically thinner, typically below $1\,\mathrm{km}$. The Arctic ABL structure and cloudiness have only a weak or no diurnal cycle due to Polar night and day (Shupe et al., 2011), but a distinct seasonal cycle (Kayser et al., 2017). The typical summertime ABL consists of a shallow mixed layer capped by persistent mixed-phase stratocumulus (Shupe, 2011; Vüllers et al., 2021). These clouds can last for several days, despite the comparably low water content, due to complex interactions between a number of local processes (Morrison et al., 2012). The typical wintertime Arctic ABL is generally stably stratified and either cloudy with weak and lifted temperature inversions or radiatively clear with surface-based temperature inversions (Pithan et al., 2016).

Clouds in the Arctic ABL are of particular importance. Arctic ABL clouds have a predominantly warming effect throughout the year, except a short time period in mid-summer (Shupe and Intrieri, 2004; Kay et al., 2016; Wendisch et al., 2019). Shupe et al. (2011) found that clouds occur $60\,\%$ to $90\,\%$ of the time in the Arctic ABL, least frequently in winter and most often in late summer and autumn. Arctic clouds are frequently of mixed-phase type, meaning they contain both supercooled liquid water and ice (Morrison et al., 2012). The persistence of Arctic mixed-phase clouds is favored by in-cloud turbulence, large-scale advection with cloud-top SHIs, and surface interactions (Morrison et al., 2012). The presence of ice and liquid water has a large impact on radiative fluxes. By modifying the outgoing and incoming irradiances, clouds affect the vertical energy transport and turbulent mixing (Brooks et al., 2017). This feeds back on the clouds, making the cloud–radiation–turbulence interactions an intertwined and complicated system. This complexity increases if the clouds are thermodynamically decoupled from lower atmospheric levels and the surface. In this case, the cloud evolution does not necessarily depend on surface energy fluxes (Curry, 1986; Shupe et al., 2013). For example, during ASCOS this occurred in $40\,\%$ of the time (Sotiropoulou et al., 2014). Multiple cloud layers

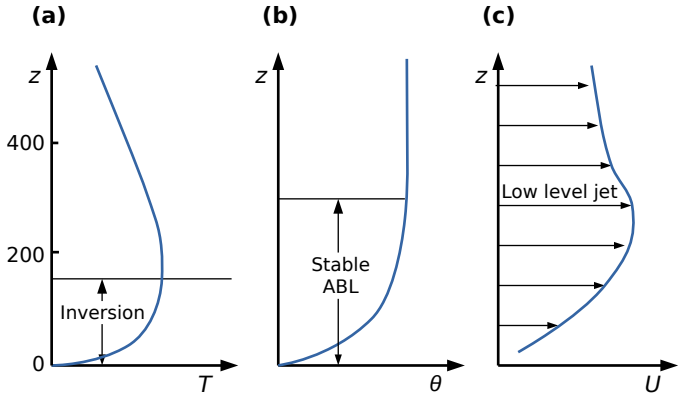

Fig. 2.9.: Typical stable ABL structure with a LLJ: **(a)** temperature T, **(b)** potential temperature θ and **(c)** wind speed U. Redrawn after Stull (1988).

and temperature inversions are possible in the Arctic ABL (Shupe et al., 2013). Shupe et al. (2013) showed that the turbulent ABL structure differs significantly for single-layer and (decoupled) multilayer clouds, indicating that the reduced cloud-top radiative cooling in the multilayer case affects the turbulent fluxes within the lower cloud layer.

The Arctic ABL exhibits numerous particular features compared to lower latitudes. Two of those, SHIs and LLJs, are analyzed in detail in this thesis (chapter 6 and 7). SHIs as one of the Arctic peculiarities are defined as locally increasing q with height. In the Arctic, this often occurs in the region of a cloud-capping temperature inversion, in contrast to lower latitudes with commonly dry air above a cloud (cf. Fig. 2.8; Nicholls and Leighton, 1986; Wood, 2012). The relative frequency of occurrence of low-level SHIs in summer is estimated to be in the range of $70\,\%$ to $90\,\%$ over the Arctic ocean (Naakka et al., 2018). SHIs can be particularly important for Arctic clouds because they might be a source of moisture for the clouds and, therefore, contribute to the longevity of Arctic clouds (Sedlar and Tjernström, 2009; Solomon et al., 2011; Morrison et al., 2012). The second analyzed ABL feature is a LLJ – a pronounced wind maximum at altitudes below $500\,\mathrm{m}$ to $1000\,\mathrm{m}$ (Blackadar, 1957). A LLJ emerges preferably in strongly stable, clear-sky ABL conditions with radiative cooling of the surface. This is the case in Polar winter (Tuononen et al., 2015) or at night at lower latitudes (Banta et al., 2006). In these conditions, a near-surface inversion forms, and vertical mixing is suppressed. The loss of turbulent friction causes an acceleration of air parcels in the mean wind direction and a LLJ forms. Figure 2.9 presents a typical wind speed profile of a LLJ in combination with the potential temperature profile. The LLJ occurs at the top of the surface-based temperature inversion. A LLJ is capable of transporting moisture or any other species

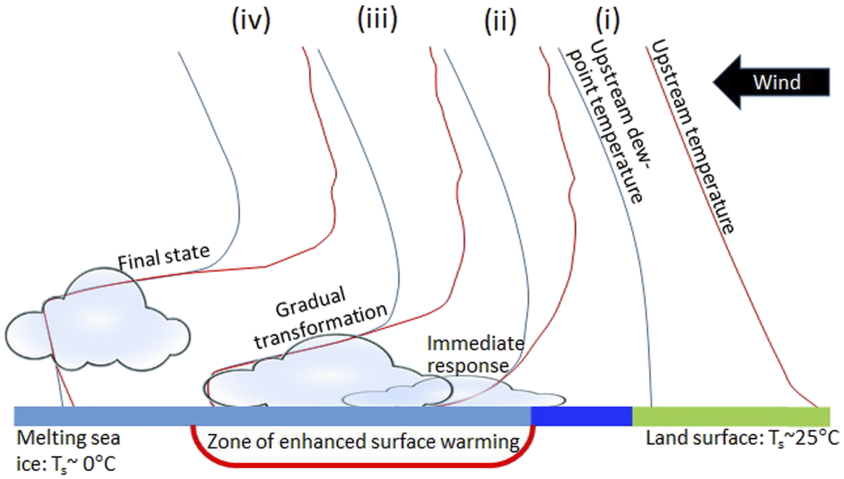

Fig. 2.10.: ABL evolution as a consequence of warm air advection from land (green) over ocean and sea ice (light blue). Adapted from Tjernström et al. (2019).

with the mean flow but also affects the vertical mixing in the ABL. Both phenomena – SHIs and LLJs – have in common that they are associated with strongly stable conditions (a cloud-top and surface-based temperature inversion, respectively). A more detailed description of SHIs and LLJs is given in the respective introductory section of chapter 6 and 7.

Beyond the local ABL processes, the Arctic ABL is influenced by external forcings, which interact with the internal physical processes (Neggers et al., 2019; Tjernström et al., 2019). One example of external forcings are warm air intrusions from the south into the central Arctic. The advection of warm air is often associated with the formation of SHIs. Tjernström et al. (2019) describe a conceptual model for warm air advection from land over sea ice and, as a consequence, the evolution of the temperature inversion (Fig. 2.10): when warm air (state i) is advected over sea ice, it is cooled by the cold surface and a surface-based temperature inversion forms (state ii). The cooling leads to condensation, hence fog or a low-level cloud. Turbulent mixing, produced by both cloud-top buoyancy and surface stress, deepens the ABL. At some point, the cloud disconnects from the surface. This final state (iv) corresponds to the cloud layer capped by a temperature inversion, which has been frequently observed in the Arctic (de Boer et al., 2009; Shupe et al., 2011; Morrison et al., 2012; Sedlar et al., 2012). This example vividly illustrates how large-scale forcings and local processes interact to shape the Arctic ABL. As a local process, turbulence plays a major role in distributing the (advected) energy vertically in the ABL.

2.3 Observations in the turbulent Arctic ABL

2.3.1 Past measurement efforts

In the central Arctic, only few in-situ vertical profile observations of turbulence parameters exist. Vertical profile measurements of turbulent energy fluxes are even less available because they require high-resolution and accurate measurements of the vertical wind velocity. Due to the remote location and harsh conditions, first vertical profile observations of turbulence in the Arctic date back to the 1980s, when aircraft observations have been performed to study the Arctic ABL (Overland, 1985; Curry, 1986). As a pioneering example, Curry (1986) observed the turbulent structure of the cloudy Arctic ABL and the interactions between radiation, turbulence, and cloud microphysics. Curry et al. (1988) categorized different types of the summertime Arctic cloudy ABL and identified some Arctic peculiarities such as humidity inversions above clouds. In the past decades, several aircraft and ship-based field campaigns have been undertaken. Wendisch et al. (2019) provide an overview of such campaigns studying the Arctic atmosphere and surface processes. Two of the outstanding campaigns are the Surface Heat Budget of the Arctic Ocean (SHEBA; Uttal et al., 2002) in 1997–1998 and ASCOS (Tjernström et al., 2014) in 2008. SHEBA studied the annual cycle of the contributions to the surface energy budget, including turbulent surface fluxes, accompanied by aircraft in different heights. ASCOS was based on the Swedish icebreaker *Oden* and focused on the formation and life cycle of Arctic low-level clouds. As one example connected to the present work, balloon-borne vertical profile measurements were combined with radar observations to study the turbulent ABL (Shupe et al., 2012). More recent campaign examples are the aircraft-based Spring-Time Atmospheric Boundary-Layer Experiment (STABLE; Tetzlaff et al., 2015) studying turbulent heat fluxes over leads and the six-month ice drift campaign Norwegian Young Sea Ice Experiment (N-ICE2015; Granskog et al., 2018) studying the atmosphere-snow-ice-ocean dynamics. Many of the campaigns included turbulence observations, some of which are addressed in the next section.

2.3.2 Observational methods

Turbulence in the ABL is measured in situ on different platforms such as aircraft, UAVs, or tethered balloons. On these platforms, common instruments to measure wind velocity fluctuations are ultrasonic anemometers (e.g., Shupe et al., 2012; Canut et al., 2016; Brooks et al., 2017) or hot-wire anemometers (e.g., Frehlich

et al., 2003; Siebert et al., 2007). A summary of the measurement principles is given in Appendix A. As another method, ground-based remote sensing of the vertical wind velocity is based on lidar or radar observations. This section provides an overview of the different methods.

Aircraft and UAVs

Aircraft can carry extensive instrumentation for probing the ABL and can cover a large geographic area. They can probe the ABL from close to the surface up to high altitudes. The downsides of aircraft measurements are that actual vertical profiles are not possible and that the lowest part of the ABL close to the surface cannot be probed. Also measuring in clouds is problematic due to icing problems of the sensors and the aircraft structure. Additionally, the high speed of the aircraft complicates the wind measurement and turbulence analysis. Further, aircraft operation is complex and expensive. However, aircraft observations are an established means to profile the turbulent Arctic ABL.

The studies of Curry (1986) and Curry et al. (1988) are based on aircraft observations over the Beaufort Sea and laid the foundation for understanding turbulent processes in the Arctic ABL. Turbulence was measured on ascents and horizontal legs, which is still a common measurement strategy nowadays. Lenschow et al. (1988) and Tjernström (1993) elaborated techniques to extract vertical profiles of turbulent fluxes from slant profile aircraft measurements. During STABLE, Tetzlaff et al. (2015) used more complicated flight patterns to study vertical turbulent flux profiles above leads in the Arctic sea ice. Aliabadi et al. (2016) tested different turbulence parameterizations against aircraft measurements of turbulent fluxes, taking into account the stable Arctic ABL and anisotropy. Finally, the field campaign PASCAL presented in this study was accompanied by aircraft measurements (Ehrlich et al., 2019) of turbulence, among others.

UAVs are more convenient to operate than crewed aircraft and are increasingly used, especially for turbulence observations. These uncrewed and remotely controlled fixed-wing aircraft or rotorcraft can fly at very low altitudes, which is advantageous for the shallow Arctic ABL (Jonassen et al., 2015). Horizontal traverses are as well possible, although with reduced areal coverage compared to crewed aircraft. Another advantage is the lower flight speed with less impact on the measured quantities. In recent years, great progress has been made in the miniaturization of meteorological sensors and, thus, improving the performance of UAV-based measurements. However, challenges remain especially under harsh Arctic conditions:

reduced battery capacity at low temperatures restricts measuring time, and icing limits the aircraft performance and excludes measurements inside clouds (Lampert et al., 2020). Another major problem is the reduced payload, which limits the capacity for carrying heavy or numerous sensors.

UAVs have been used in the Arctic since around the year 2000 (Curry et al., 2004), and recently more frequently (Bates et al., 2013; Jonassen et al., 2015; de Boer et al., 2018). High-resolution turbulence measurements are possible with UAVs (Kroonenberg et al., 2008; Calmer et al., 2018; Kral et al., 2020) and turbulence parameters have been derived from those measurements (Balsley et al., 2018; Luce et al., 2019). However, UAV observations often provide the one-dimensional horizontal wind velocity relative to the instrument. The lack of the directly measured, earth-referenced vertical wind velocity requires further considerations to estimate turbulent fluxes. For example, Knuth and Cassano (2014) apply an integral method to retrieve the fluxes from mean quantities, or Båserud et al. (2019) derive fluxes from several consecutive vertical mean profiles.

Tethered balloons

Tethered balloons can address some of the shortcomings of crewed and uncrewed aircraft. Tethered balloons are lifting-gas filled balloons with the instrument payload hanging below the envelope, restrained by a tether, and lowered and lifted by a winch on the ground. They are beneficial for profiling the ABL for several reasons:

- Measurements can be taken on a vertical profile or at constant altitude.
- The whole vertical profile of the ABL can be covered: balloon measurements can close the gap between surface-based and aircraft measurements.
- The slow ascent rate enables a high vertical resolution.
- Operation inside clouds and at icing conditions is possible.
- Comparing measurements on the ascent and descent helps to exclude instrument errors.

Tethered balloons are less affected by icing than aircraft because they move at a lower true airspeed resulting in less ice accumulation, and the probability of ice sticking on the balloon is reduced due to its flexible envelope. Depending on the size of the applied balloon, they can lift payloads from a few kilograms up to several tens of kilograms to an altitude of $1\,\mathrm{km}$ or more for up to several hours. The resulting vertical profiles enable to study small-scale local cloud and atmospheric properties,

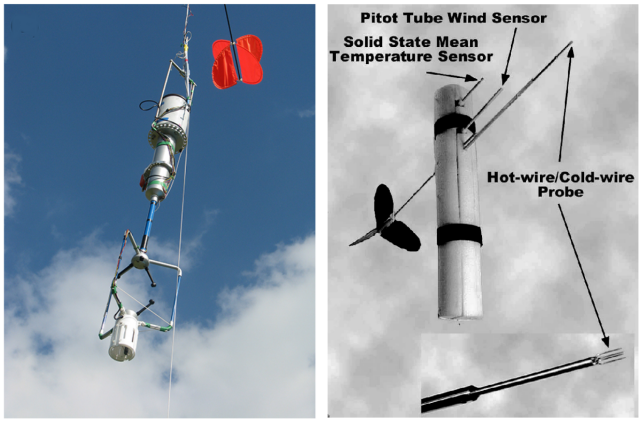

Fig. 2.11.: Balloon-borne turbulence instruments used in previous studies: sonic anemometer (left) and hot-wire anemometer (right). Adopted from Canut et al. (2016) and Frehlich et al. (2003).

which are otherwise smoothed out by the large distances covered by aircraft, which cannot fly true vertical profiles. In addition, tethered balloon systems can observe individual profiles within a single turbulent eddy, whereas aircraft measurements average over at least a few eddies. However, the difference in true airspeed of balloon and aircraft measurements results in variable statistics: an aircraft can probe a much larger area, enabling more robust statistics (assuming horizontal homogeneity). For many research questions, it is crucial to obtain vertical profile measurements starting at the surface level. This is particularly true for the Arctic ABL, which is often shallow and characterized by height-dependent energy fluxes in the lowermost part. To understand complex atmospheric processes interacting at the sea ice–atmosphere interface, it is crucial to measure the lowermost part of the ABL, which can be realized by applying a tethered balloon.

Tethered balloons have been successfully deployed in the Arctic, for example during ASCOS (Shupe et al., 2012; Kupiszewski et al., 2013), in Arctic Alaska (de Boer et al., 2018; Dexheimer et al., 2019; Creamean et al., 2021) and in Ny-Ålesund (Lawson et al., 2011; Sikand et al., 2013; Mazzola et al., 2016; Ferrero et al., 2019). Many of them made use of flying balloons inside clouds for studying Arctic mixed-phase clouds. Mayer et al. (2012) operated a tethered balloon and a UAV simultaneously in Svalbard and concluded that both systems complement each other with the balloon providing higher accuracy below $200\,\mathrm{m}$ due to the low vertical velocity of the balloon. Above, the UAV is more successful in penetrating strong inversion layers. Duda et al. (1991) and Becker et al. (2018) used a tethered balloon to measure vertical profiles of irradiances and derived heating rates from the measurements. Progress in obtaining turbulence profiles was made by Frehlich et al. (2003), who derived dissipation rates and temperature structure parameters from a balloon-borne hot-

wire anemometer (Fig. 2.11). During ASCOS, vertical profiles of dissipation rates in the summertime Arctic ABL were derived from a balloon-borne sonic anemometer (Shupe et al., 2012; Brooks et al., 2017). Canut et al. (2016) showed that it is possible to measure the three-dimensional, geo-referenced wind vector using a tethered balloon, whose motion is directly affected by the turbulent wind field. They used a tethered balloon carrying a sonic anemometer (Fig. 2.11), corrected the measured wind vector for the instrument motion, and estimated sensible heat fluxes from the wind measurements.

Remote sensing

In-situ measurements are frequently complemented by ground-based remote-sensing observations to get a broader picture of the ABL structure. The striking advantage of remote-sensing observations is the time-continuous vertical profile of ABL conditions, which allows studying the temporal ABL evolution. As a disadvantage, the lowest tens of meters are not seen by the instruments, and the vertical resolution is typically $30\,\mathrm{m}$ to $40\,\mathrm{m}$, which might be too coarse for sharp gradients. Turbulence parameters are retrieved from statistical properties of cloud radar or vertically pointing lidar Doppler velocity measurements. In-situ measurements, such as tethered balloon observations, have been used to validate the remote sensing measurements. Shupe et al. (2012) compared dissipation rates derived from radar data and tethered balloon measurements and found in general a good agreement (Fig. 2.12), except modest deviations in particularly low- or high-turbulence regimes.

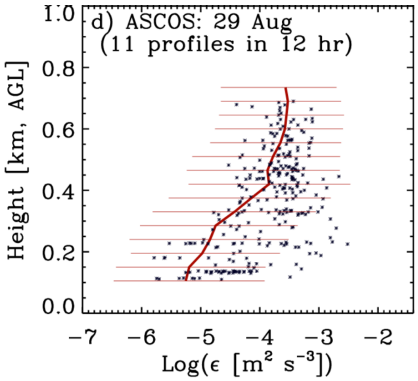

Fig. 2.12.: Dissipation rate derived from radar observations (mean as a red line with range 5th to 95th percentiles) and a tethered balloon (black dots). Adapted from Shupe et al. (2012).

3 The BELUGA tethered balloon system

This chapter presents the new BELUGA tethered balloon system (Sect. 3.1) and describes the particular instrument packages including their technical design and data processing routines (Sect. 3.2 to Sect. 3.5). Two turbulence packages (Sect. 3.2 and Sect. 3.3) are the central instruments for the data analysis of the present thesis. Major parts of this chapter, data analysis methods, and exemplary results from PASCAL have been published in Egerer et al. (2019a).

3.1 The BELUGA platform

3.1.1 Tethered balloon system

BELUGA is based on a helium-filled tethered balloon (Fig. 3.1) with a volume of $90\,\mathrm{m}^3$ with a scientific payload up to $10\,\mathrm{kg}$. The balloon operates in altitudes between the surface and $1500\,\mathrm{m}$ at maximum wind speeds up to $15\,\mathrm{m\,s^{-1}}$. An electric winch retains the balloon with climb and descent rates of typically $1\,\mathrm{m\,s^{-1}}$ to $3\,\mathrm{m\,s^{-1}}$. The balloon is captured by a $3\,\mathrm{mm}$ thick Dyneema® tether with $900\,\mathrm{daN}$ strength. It is equipped with an emergency deflation system in case of tether failure. The tethered balloon system can operate inside clouds and under light icing conditions.

The logistics necessary for the $90\,\mathrm{m}^3$ balloon are complex: five persons are needed to operate the balloon, large amounts of Helium must be shipped and in case of a storm, securing the balloon is difficult. As an alternative, a $9\,\mathrm{m}^3$ tethered balloon can be used as measurement platform. The balloon is made of a thin plastic envelope and can lift up to $6\,\mathrm{kg}$ payload at a maximum wind speed of $12\,\mathrm{m\,s^{-1}}$. The tether ($2\,\mathrm{mm}$ thick, $450\,\mathrm{dN}$ strength) is $2000\,\mathrm{m}$ long and has fixed attachment points for the instruments at $10\,\mathrm{m}$, $15\,\mathrm{m}$ and $19\,\mathrm{m}$ below the balloon junction.

For operation on the tethered balloon, three instrument packages were developed: an ultrasonic anemometer package (UP), a hot-wire anemometer package (HP), and a payload measuring solar and terrestrial broadband irradiances (broadband

Fig. 3.1.: The tethered balloon system on the ice floe next to RV *Polarstern*.

radiation package, BP). The packages are deployed in one of three main configurations, depending on the conditions and requirements for turbulence and radiation measurements (Fig. 3.2): configuration 1 is designed for combined turbulence and radiation measurements in rather low wind conditions up to $10\,\mathrm{m\,s^{-1}}$, when the lift of the balloon allows a larger mass of the payload. It includes the UP for turbulence and one BP for radiation measurements. For strong wind conditions, the payload is reduced to reach a sufficient maximum altitude. This configuration 2 comprises the HP and one BP. Configuration 3 is applied in most favorable conditions (low and uniform wind speed), comprised of the UP and two BPs. In all configurations, an additional separate standard meteorology package routinely measures air temperature, relative humidity, wind velocity and altitude and transmits the data to the ground for online monitoring. The ultrasonic anemometer, with a weight of around $6\,\mathrm{kg}$, is attached at a fixed point at a distance of $20\,\mathrm{m}$ below the balloon; the other more lightweight payloads HP and BP ($<3.5\,\mathrm{kg}$) can be flexibly attached to the tether at any distance from the balloon. With the smaller balloon, only instrument configuration 2 with the light-weight instruments is possible due to the reduced payload. The modular instrument setup allows the adjustment of instruments to different scientific questions.

In addition to the standard meteorology package, all instrument packages are equipped with basic meteorological sensors. For all instrument packages, the barometric altitude is calculated from the barometric pressure p_b by

$$z_\mathrm{b} = \frac{T_0}{\gamma} \cdot \left(1 - \frac{p_\mathrm{b}}{p_0}^{R \cdot \gamma / g}\right), \tag{3.1}$$

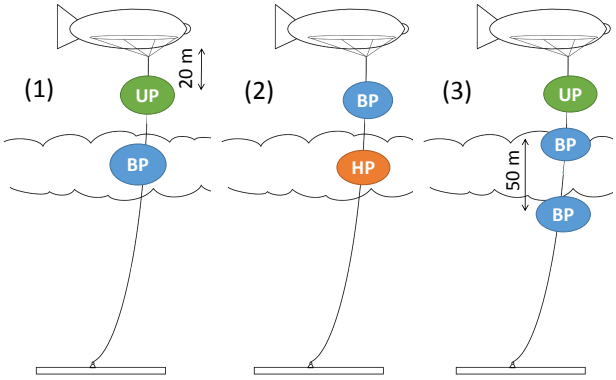

Fig. 3.2.: Three main instrument configurations on the tethered balloon: (i) configuration 1 with an UP and a broadband radiation package (BP), (ii) configuration 2 with a BP and a hot-wire anemometer package (HP), and (iii) configuration 3 with an UP and two BPs. Due to the modular approach, further configurations are possible. Distances and dimensions are not to scale.

with the standard adiabatic lapse rate $\gamma = 6.5\,\mathrm{K\,km^{-1}}$ (Wendisch and Brenguier, 2013). The near-surface pressure p_0 is a $10\,\mathrm{s}$ average of the payload's p_b before the start of the flight. The barometric pressure is corrected for the near-surface pressure change over each flight by subtracting a linear trend, if ground-based measurements are available. The near-surface temperature T_0 is measured at a nearby meteorological mast (for PASCAL) or a $10\,\mathrm{s}$ average of the payload's measurement before the start. This standardized procedure ensures comparable altitudes for the individual instrument packages.

3.1.2 Measurement strategy

The sampling strategy is based on two different approaches. (i) The first approach is keeping BELUGA at a constant altitude for a time period of typically $10\,\mathrm{min}$ to $15\,\mathrm{min}$. In this case, the data provide a statistical basis for turbulent flux estimates or to characterize the time evolution of the radiative cloud properties. (ii) A continuous ascent or descent through the ABL yields a vertical profile to study the vertical distribution of ABL parameters.

Measurements close to the surface are used for a comparison to measurements of ground-based instruments. Figure 3.3 shows an exemplary height record for one complete flight, which includes all elements of the measurement strategy. After an hour-long measurement period near the surface, a continuous ascent is performed. This provides an overview of the boundary layer structure using the online measurements of the meteorology instrument package and is the basis for the

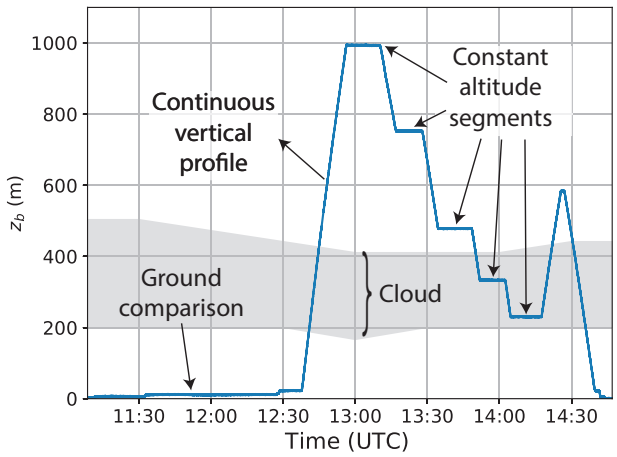

Fig. 3.3.: Measurement strategy illustrated by the balloon altitude time series of 5 June 2017. The two approaches are (1) constant-altitude segments and (2) a continuous vertical profile. The shaded area illustrates the vertical extent of the cloud layer.

measurements of the second part of the flight: levels for continuous measurements at fixed altitudes were defined around the temperature inversion and inside the cloud layer.

3.2 Ultrasonic anemometer package (UP)

3.2.1 Instrument design

The UP (Fig. 3.4) is based on an ultrasonic anemometer and is the central instrument package of this work. Ultrasonic (or sonic) anemometer measurements provide the three-dimensional wind vector and are considered to be unaffected by cloud droplets (Siebert and Teichmann, 2000). A brief description of the measurement principle of sonic anemometers is given in Appendix A. The UP includes measurements of the wind vector $\vec{u}_\mathrm{S}$ and virtual temperature T_v (which is approximately the sonic temperature) with a sampling frequency of $f_\mathrm{s} = 50\,\mathrm{Hz}$, accompanied by a thermometer and a capacitive humidity sensor. The particular instruments and their characteristics are listed in Table 3.1. The attachment point for the UP $20\,\mathrm{m}$ below the balloon allows for rotation around the tether and pitch alignment. A wind vane ensures that the anemometer turns towards the mean wind direction. The UP is complemented by a power supply based on lithium-polymer batteries with $6.4\,\mathrm{A\,h}$ at $12.8\,\mathrm{V}$. This allows for an operation of 4 h in Arctic summer conditions. The data

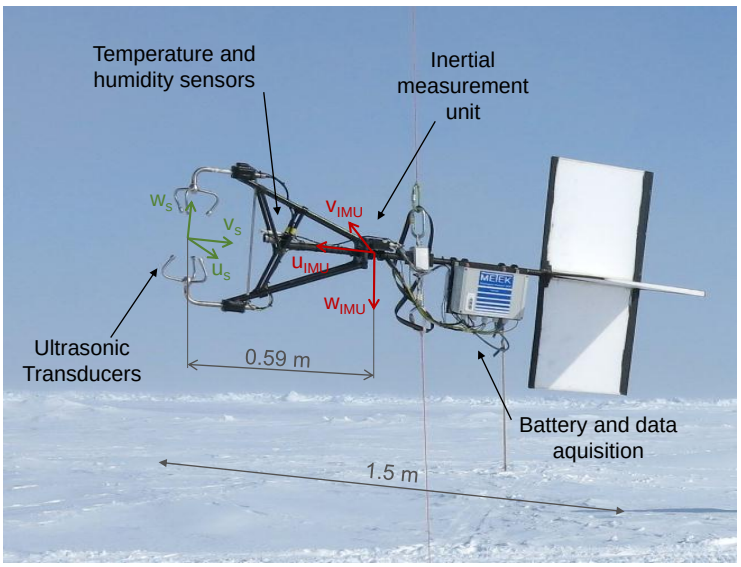

Fig. 3.4.: The ultrasonic anemometer package (UP) with coordinates systems of the instruments.

acquisition consists of a serial data logger recording on an SD card. With all sensors, data acquisition and surroundings the total mass of the UP adds up to $6\,\mathrm{kg}$.

3.2.2 Wind vector

To measure the geo-referenced wind vector from a moving platform such as a tethered balloon, the attitude and motion of the instrument have to be measured precisely and the wind vector measured in the sonic frame has to be corrected for this motion (Canut et al., 2016). The wind measurements are performed using a Metek uSonic-3 anemometer, complemented by a GPS-assisted inertial measurement unit (IMU, Table 3.1) for the attitude and motion correction. A data logger collects the two data streams from the sonic sensor and the IMU via two serial ports. The IMU data are binary data and are converted into text data before post-processing. The IMU and sonic data stream are synchronized by an analog pulse-per-second (PPS) signal, which is sent from the IMU to the sonic data acquisition. A careful temporal synchronization of sonic and IMU measurements is a basic requirement for a successful transformation of the sonic wind vector. The sonic transducers are heated for anti-icing. The IMU's accuracy for roll and pitch angles is 0.1° for angles not exceeding $\pm 10°$. The sonic anemometer has a resolution of $1\,\mathrm{cm\,s^{-1}}$ and $10\,\mathrm{mK}$, respectively.

Tab. 3.1.: Instrument characteristics of the ultrasonic anemometer package (UP).

Instrument	Manufacturer	Quantity	Range	Resolution
Ultrasonic anemometer uSonic-3 Class A, with external PT100	Metek GmbH, Germany	$\vec{u_\mathrm{S}}$, T_v, T	0-20 $\mathrm{m\,s^{-1}}$, $-$35-55 °C	50 Hz
Inertial measurement unit iμVRU+iTILT	iMAR Navigation GmbH, Germany	$\vec{u}_\mathrm{IMU}$, $\vec{\Omega}$, ϕ, ϑ, ψ, p_b	0-100 $\mathrm{m\,s^{-1}}$, 250 $^\circ\,\mathrm{s^{-1}}$	50 Hz
Thermocouple 5TC-TT-KI-10-1M	Omega Engineering, Inc., USA			
Transducer LKM 212 for thermocouple	LKM electronic GmbH, Germany	T	$-$20-80 °C	10 Hz
Humidity sensor EE08	E + E Elektronik GmbH, Austria	RH	0-100 %	1 Hz

Transforming the wind vector, as measured in the sonic framework $\vec{u}_\mathrm{S} = (u_\mathrm{S}, v_\mathrm{S}, w_\mathrm{S})$, into an earth-fixed reference system is a standard procedure for research aircraft (Lenschow, 1986; Vickers and Mahrt, 1997; Wendisch and Brenguier, 2013). In contrast, for a tethered balloon it is more challenging because the turbulence to be measured drives the motion of the balloon with the same frequency range. This instrument motion $\vec{u}_\mathrm{IMU} = (u_\mathrm{IMU}, v_\mathrm{IMU}, w_\mathrm{IMU})$ is measured by the IMU. The geo-referenced wind vector $\vec{u}_\mathrm{E} = (u_\mathrm{E}, v_\mathrm{E}, w_\mathrm{E})$ is obtained by applying the following transformation:

$$\vec{u}_\mathrm{E} = \mathbf{T} \cdot (\vec{u}_\mathrm{S} + \vec{\Omega} \times \vec{L}) + \vec{u}_\mathrm{IMU}, \tag{3.2}$$

with the rotational velocities $\vec{\Omega}$ as measured by the IMU and the lever arm vector $\vec{L} = (59\,\mathrm{cm}, 0, 0)$ between IMU and sonic. The coordinate systems of sonic and IMU are shown in Fig. 3.4. The transformation matrix $\mathbf{T}$ is a function of the Euler angles roll ϕ, pitch ϑ and yaw ψ, which are provided by the IMU:

$$\mathbf{T} = \begin{bmatrix} \cos\psi \cdot \cos\vartheta & -\sin\psi \cdot \cos\phi + \cos\psi \cdot \sin\vartheta \cdot \sin\phi & \sin\psi \cdot \sin\phi + \cos\psi \cdot \sin\vartheta \cdot \cos\phi \\ \sin\psi \cdot \cos\vartheta & \cos\psi \cdot \cos\phi + \sin\psi \cdot \sin\vartheta \cdot \sin\phi & \sin\vartheta \cdot \cos\phi \cdot \sin\psi - \sin\phi \cdot \cos\psi \\ -\sin\vartheta & \cos\vartheta \cdot \sin\phi & \cos\vartheta \cdot \cos\phi \end{bmatrix}.$$

The resulting geo-referenced wind vector $\vec{u}_\mathrm{E}$ is in a right-handed north-east-down coordinate system. However, when presenting results for the vertical wind velocity, the sign of w_E is inverted in order to stay within the conventions of meteorology with a positive upward defined wind speed.

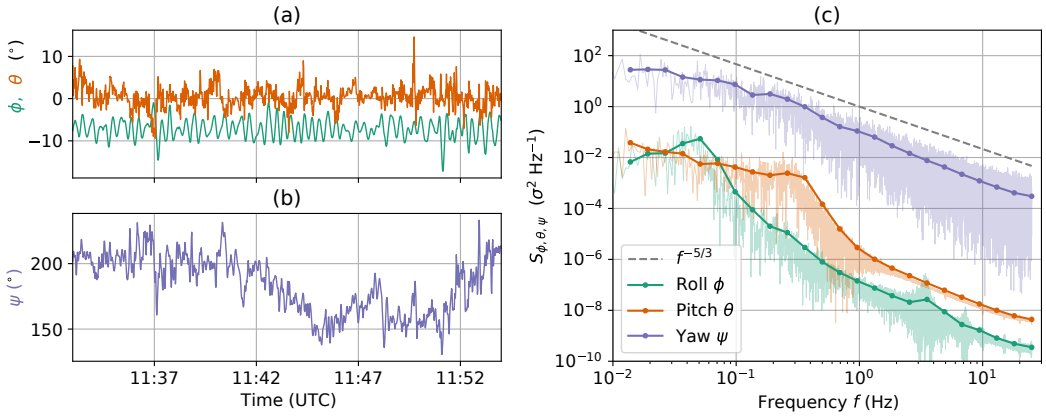

Fig. 3.5.: Time series **(a, b)** and power spectral density S **(c)** of the Euler angles roll ϕ, pitch θ and yaw ψ measured by the IMU on the UP. The time series used for the spectra calculations was recorded on 5 June 2017, 11:33–11:54 UTC, with the balloon kept at $20\,\mathrm{m}$ altitude.

Figure 3.5 illustrates the instrument motion in a $20\,\mathrm{min}$ time series of the Euler angles and the corresponding frequency spectra. The yaw angle spectrum shows almost a $-5/3$ slope indicating inertial subrange scaling. This behavior is due to the fact that the probe can freely rotate about its vertical axis and the yaw angle variations are dominated by the turbulent wind direction rather than the balloon motion. This is different for the roll and pitch angles, showing distinct peaks at $0.05\,\mathrm{Hz}$ and $3\,\mathrm{Hz}$ for the roll angle and $0.3\,\mathrm{Hz}$ for the pitch angle. The roll angle peak is most probably a result of lateral motion of the balloon itself, whereas the pitch angle might be a combination of balloon motion and a pitch motion of the payload. In the time series, the roll angle oscillation is obvious.

The result of a geo-referenced wind vector measurement from a moving platform is furthermore affected by misalignment between the IMU and the wind sensor. Small offset angles in roll $\Delta\phi$ and pitch $\Delta\vartheta$ can be estimated by applying post-processing algorithms. Here, we apply a correction procedure based on Wilczak et al. (2001), who suggest that for a sufficiently long record the mean vertical wind vanishes. First, the roll angle is assumed be negligible for w_E and with $\phi = 0$ the vertical wind velocity component w_E in Eq. (3.2) simplifies to

$$w_\mathrm{E} \equiv 0 = -u_\mathrm{S,I} \cdot \sin(\vartheta + \Delta\vartheta) + w_\mathrm{S,I} \cdot \cos(\vartheta + \Delta\vartheta) + w_\mathrm{IMU}, \tag{3.3}$$

where $\vec{u}_\mathrm{S,I} = \vec{u}_\mathrm{S} + \vec{\Omega} \times \vec{L}$ considers the lever arm component. This equation is solved for $\Delta\vartheta$ with a Levenberg-Marquardt algorithm for a defined test period either near

Tab. 3.2.: Characteristics of the instruments on the $10\,\mathrm{m}$ meteorological and turbulence mast during PASCAL.

Instrument	Manufacturer	Quantity	Range	Resolution
Ultrasonic anemometer USA-1	Metek GmbH, Germany	$\vec{u}_\mathrm{S}$, T_v	0-50 $\mathrm{m\,s^{-1}}$	20 Hz
Thermo-/hygrometer HMHP40	Vaisala Corporation, Finland	T, RH	-40-180 °C, 0-100 %	1 Hz
Barometer PTB220	Vaisala Corporation, Finland	p_b	500-1100 hPa	1 Hz

the surface or in calm air. Considering a small $\Delta\phi$ and the $\Delta\vartheta$ offset, Eq. (3.2) for w_E yields

$$\begin{aligned} w_\mathrm{E} \equiv 0 = &- u_\mathrm{S,I} \cdot \sin(\vartheta + \Delta\vartheta) + v_\mathrm{S,I} \cdot \sin(\phi + \Delta\phi) \cdot \cos(\vartheta + \Delta\vartheta) \\ &+ w_\mathrm{S,I} \cdot \cos(\phi + \Delta\phi) \cdot \cos(\vartheta + \Delta\vartheta) + w_\mathrm{IMU}. \end{aligned} \tag{3.4}$$

This equation is solved for $\Delta\phi$ again with a Levenberg-Marquardt algorithm in the same defined test period. For the PASCAL campaign, $\Delta\vartheta = 0.8\,°$ for pitch and $\Delta\phi = 5.15\,°$ for roll offset are determined in a defined time period of roughly $30\,\mathrm{min}$, where the balloon was kept near the surface. Those angle offsets are applied to all campaign data by adding to the measured angles in $\mathbf{T}$. The resulting geo-referenced horizontal wind velocity components serve to calculate the wind direction: $dd = \arctan\left(\overline{v}_\mathrm{E}/\overline{u}_\mathrm{E}\right)$.

The results of the wind vector calculation are verified by a comparison to mast measurements. During PASCAL, a $10\,\mathrm{m}$ meteorological mast was situated close to the balloon site. On the mast, an ultrasonic anemometer measured the wind velocity with $20\,\mathrm{Hz}$ sampling frequency. Instrument characteristics are listed in Table 3.2. A $20\,\mathrm{min}$ BELUGA data set recorded at around $20\,\mathrm{m}$ altitude is compared to mast measurements in the same time period. Figure 3.6 shows a time series of vertical wind velocity measured by the sonic anemometer installed on the mast and the balloon payload UP, as well as the power spectral densities. The measured vertical wind velocity fluctuates around values close to zero and the standard deviation on the balloon sonic $\sigma_w = 0.19\,\mathrm{m\,s^{-1}}$ is close to the mast sonic $\sigma_w = 0.16\,\mathrm{m\,s^{-1}}$. In the spectra shown in Fig. 3.6b, both curves reveal an inertial subrange with comparable power spectral density values. The curves flatten at frequencies above $5\,\mathrm{Hz}$ for the mast and $10\,\mathrm{Hz}$ for the balloon. This flattening is due to uncorrelated noise. With a spectral noise floor of $S_w^{(\mathrm{n})} \approx 4 \times 10^{-5}\sigma^2\,\mathrm{Hz^{-1}}$ and the Nyquist frequency of

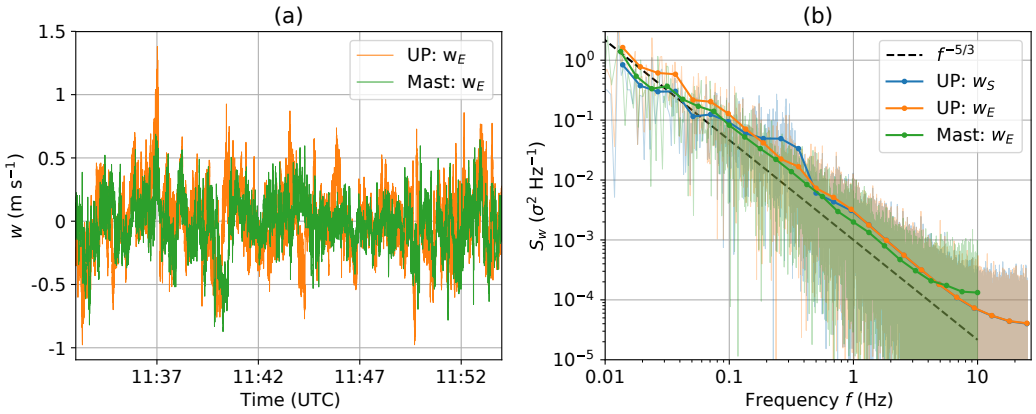

Fig. 3.6.: Time series of the vertical wind velocity w **(a)** and power spectral density S_w **(b)**. Wind velocities are shown for the UP measurements with (orange) and without motion correction (blue, only plotted in panel **b**). As reference, the sonic data measured on the mast at a height of $10\,\mathrm{m}$ are presented (green). The time period is the same as in Fig. 3.5; the mean horizontal wind velocity for this period was $1.7\,\mathrm{m\,s^{-1}}$.

$f_{\mathrm{Ny}} = f_{\mathrm{s}}/2 = 25\,\mathrm{Hz}$, the standard deviation due to uncorrelated noise (Eq. 2.11) of $\sigma_w^{(\mathrm{n})} \approx 0.03\,\mathrm{m\,s^{-1}}$ can be estimated for the balloon UP and $\sigma_w^{(\mathrm{n})} \approx 0.04\,\mathrm{m\,s^{-1}}$ for the mast. The noise level for the UP horizontal wind velocity is 5 times higher than for vertical wind velocity (not shown here). In a revised version of the UP of 2018, $\sigma_w^{(\mathrm{n})}$ could be halved after replacing the sonic transducers. The standard deviation due to uncorrelated noise for the sonic temperature is $\sigma_{T_{\mathrm{v}}}^{(\mathrm{n})} \approx 0.05\,\mathrm{K}$.

In addition to the spectrum of the motion-corrected vertical velocity component w_{E} (orange curve), the spectra for the uncorrected vertical sonic component w_{S} (blue curve) are shown in Fig. 3.6b. The blue curve clearly shows the spectral peak around $0.3\,\mathrm{Hz}$ caused by the pitch motion (cf. Fig. 3.5c). This motion is strongly reduced in the orange curve, indicating a successful correction procedure and a clear power law. However, under certain conditions – in particular near the surface with increased wind fluctuations – the balloon motion cannot be completely eliminated from the sonic measurements and is still visible in the spectrum, especially for the u and v component. This is probably due to the fact that the wind fluctuations which drive the balloon motion are in the same frequency range as the turbulence to be measured.

3.2.3 Temperature

For temperature measurements, the UP includes a PT100 thermometer as reference and a fast-response thermocouple sensor. The temperature readings are sampled

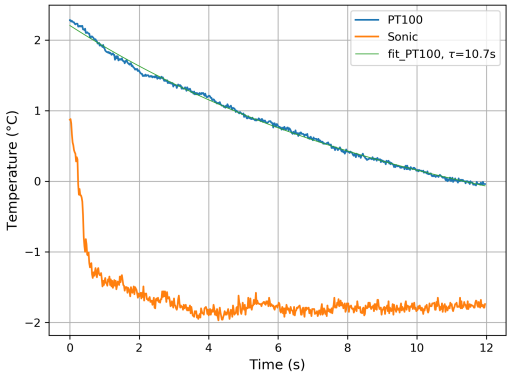

Fig. 3.7.: Temperature step response experiment realized at a sharp temperature inversion.

with 16-bit resolution and $50\,\mathrm{Hz}$ sampling frequency by additional analog inputs of the sonic anemometer. Therefore, temperature and wind velocity data are synchronized. The PT100 provides a slow-response but relatively accurate temperature measurement. As the time response for the temperature measurements is finite, the time-lag error in the temperature signal has to be corrected. Assuming a first-order sensor response, the time dependence of the measured signal $x_\mathrm{m}(t)$ (T in this case) is given by

$$\frac{\mathrm{d}x_\mathrm{m}}{\mathrm{d}t} = \frac{1}{\tau}\left(x_\mathrm{a} - x_\mathrm{m}\right) \tag{3.5}$$

with the e^{-1} time constant τ and the ambient ("true") signal x_a. The time constant τ depends on the temperature and ventilation of the sensor with larger response times at low temperatures and small flow speeds. We assume a constant τ for each sensor. The time constants τ_PT100 $\approx$10 s and $\tau_\mathrm{thermo} \approx 0.64\,\mathrm{s}$ are determined for a rapid temperature change when descending through a sharp inversion layer[1], simulating a first-order step response experiment. The temperature time constants τ result from fitting the temperature step response to the function:

$$T(t) = T_1 + T_2 \cdot e^{\,-t/\tau} \tag{3.6}$$

with the constants T_1 and T_2. Figure 3.7 shows the step response of the PT100 to the temperature change across the inversion together with the sonic temperature (which is supposed to have a negligible time response). For both the thermocouple and the PT100 sensor, the time-response error is corrected similar to McCarthy (1973) by the relation:

$$T_\tau = T + \frac{\partial \widetilde{T}}{\partial t} \cdot \tau. \tag{3.7}$$

[1] PASCAL data of 5 June 2017, 14:31 UTC.

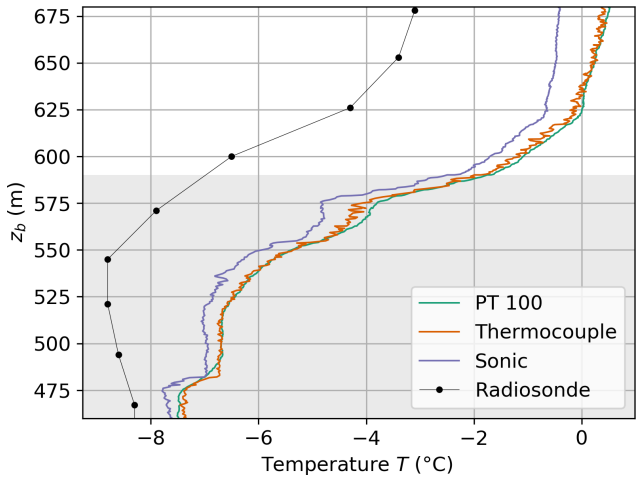

Fig. 3.8.: Comparison of balloon-borne temperature profiles measured with the UP descending at 10:00 UTC on 7 June 2017. The plot shows temperature T as a function of barometric altitude z_b around a temperature inversion capping the cloud layer (shaded area, determined from relative humidity and Cloudnet data). The temperature vertical profile includes the time-response-corrected PT100, corrected and calibrated thermocouple data, and temperature calculated from the sonic temperature. Plotted data are averaged over $0.5\,\mathrm{s}$ intervals. The temperature profile as observed from the radiosonde about $2\,\mathrm{h}$ later is shown for comparison.

The tilde represents a Savitzky–Golay low-pass filtered temperature signal (2nd order, time window of τ). After time-response correction of both thermocouple and PT100, the thermocouple sensor is calibrated for each flight separately from the PT100 sensor via a linear regression. The calibrated and corrected thermocouple signal is temperature signal used for further analyses in this work. The sonic temperature (approximately the virtual temperature) is directly measured by the sonic anemometer with a time response below $20\,\mathrm{ms}$ and therefore serves as a reference. Typically, sonic temperature measurements show an offset due to the measurement principle. This offset is corrected by a calibration with the virtual temperature calculated from temperature and humidity sensors.

In Fig. 3.8, the PT100 and thermocouple temperatures are compared to the temperature calculated from the virtual (sonic) temperature by $T = T_\mathrm{v} \cdot (1 + 0.61 \cdot q)^{-1}$. The thermocouple data resolve small features inside the temperature inversion layer, which are also seen in the sonic temperature. In the time-response-corrected PT100 signal, details and fluctuations are not completely resolved. The comparison with a radiosounding (Vaisala RS92-SGP, Schmithüsen, 2017) illustrates the capability of the BELUGA measurements to resolve small-scale structures. The temperature difference between balloon and radiosonde measurements is probably caused by the 2 h time lag between the measurements.

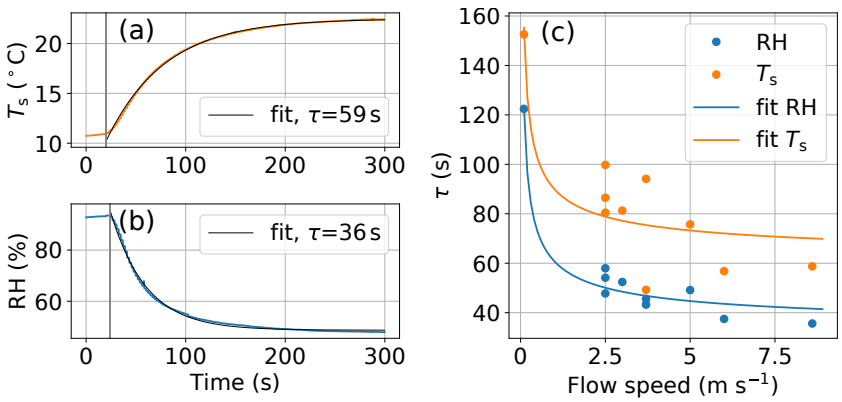

Fig. 3.9.: Time response of the BELUGA humidity sensor to a step function experiment: **(a)** sensor-internal temperature T_s and **(b)** RH at $8.6\,\mathrm{m\,s^{-1}}$ with fitted time constants τ. Panel **(c)** shows the time constants depending on the flow speed. A root fit function is added to the values.

3.2.4 Relative humidity (RH)

Relative humidity (RH) is measured with an EE08 capacitive humidity sensor. Similar to the temperature sensors, the relative humidity signal of the UP is time-response-corrected with $\tau \approx 6\,\mathrm{s}$, as specified by the manufacturer. The correction for sensor inertia improves the resolution of vertical structure in RH, but still the sensor is slow compared to the temperature measurements. A weak point of the capacitive humidity sensor is its deficiency to reproduce values close to saturation in clouds. In contrast, the applied radiosonde type (Schmithüsen, 2017) shows small RH measurement errors being systematically below $4\,\%$ in the high-latitude troposphere (Ingleby, 2017). Therefore, the EE08 sensor is calibrated by comparing to the temporally closest radiosonde by a first-order polynomial regression. With the applied corrections, the measured humidity inside clouds still varies between $95\,\%$ and $100\,\%$.

The time constants of the humidity sensor are re-evaluated when studying humidity inversions (chapter 6), because a remarkable difference in RH between ascent and descent of BELUGA was observed. I determine the time constants for the BELUGA humidity sensor in laboratory experiments by analyzing the sensor response to a step-like change of the surrounding thermodynamical parameters. The sensor is brought from a calm and saturated environment into a sub-saturated airstream with constant T and RH. The flow speed of the sub-saturated air is varied between $2\,\mathrm{m\,s^{-1}}$ and $9\,\mathrm{m\,s^{-1}}$. The housing of the RH sensor, which has a high diffusivity for water vapor, also accommodates a temperature sensor for the sensor-internal temperature T_s, which is determined by a PT-1000.

Figure 3.9a and 3.9b show an example for the time response of the humidity sensor on BELUGA. The time constants τ_{RH} and τ_{T_s} are obtained from an exponential fit to the response function at a constant flow speed of $8.6\,\mathrm{m\,s^{-1}}$. Figure 3.9c summarizes the resulting time constants for different flow speeds. The time constant of a temperature and RH sensor is influenced by the heat and moisture transfer, which scale with the flow speed $\propto 1/\sqrt{U}$ (e.g., Bruun, 1995, for heat transfer). Based on this relationship, a least-square fit to the observations yields the τ values depending on the flow speed. For flow speeds typical for atmospheric observations, time constants of $\tau_{T_\mathrm{s}} \approx 70\,\mathrm{s}$ and $\tau_{\mathrm{RH}} \approx 50\,\mathrm{s}$ are estimated. Similar to Miloshevich et al., 2004, these estimated time constant are multiplied by a factor of 0.8 before the time series reconstruction to avoid potential over-correction.

The re-evaluated time constants are much higher than those for the temperature time response correction (Eq. 3.7). Therefore, I use the direct solution of Eq. (3.5) to correct the time lag with these constants. The time-lag-corrected signal is

$$x_\tau = \frac{\tilde{x}_\mathrm{m}(t) - \left[\tilde{x}_\mathrm{m}(t-\Delta t)\cdot e^{-\Delta t/\tau}\right]}{1 - e^{-\Delta t/\tau}}, \tag{3.8}$$

with Δt being the time step between two consecutive measurement points (Miloshevich et al., 2004). Here, I assume that the time-corrected value (index τ) is equal to the ambient value x_a. The tilde in Eq. (3.8) represents the low-pass-filtered, measured time series of RH.

3.3 Hot-wire anemometer package (HP)

The HP is based on hot-wire anemometer wind measurements. A first version of the HP was deployed during PASCAL. After this campaign, the instrument package was revised and a new data acquisition was included. The instrument design for each version is described in this section. The data processing routines are similar for both versions of the HP.

3.3.1 First version of the hot-wire package

Instrument design

The HP (Fig. 3.10) is used to measure the one-dimensional wind velocity with a temporal resolution of $111\,\mathrm{Hz}$. The centerpiece is a $5\,\mu\mathrm{m}$ hot-wire sensor connected

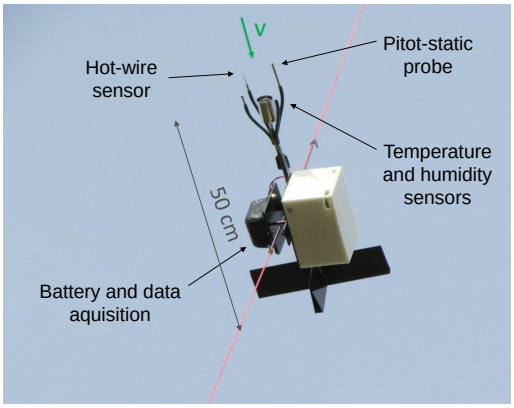

Fig. 3.10.: First version of the hot-wire anemometer package (HP).

to a small constant-temperature anemometer circuit (Dantec MiniCTA). The electrical circuit keeps the temperature of the wire sensor constant; the voltage output of the circuit is related to the wind velocity. The principle of hot-wire anemometry is briefly described in Appendix A. For reference, the dynamic pressure is measured by a pitot-static probe, connected to a differential pressure gauge. The hot-wire and the pitot-static sensors face the mean airflow by means of a wind vane. Icing of the pitot-static probe was observed only for one flight during the PASCAL campaign.

The hot-wire package is complemented by a power supply with $5.2\,\mathrm{Ah}$ at $14.8\,\mathrm{V}$, allowing operating times of more than $5\,\mathrm{h}$. A sensor boom at the tip of the probe ensures undisturbed hot-wire and temperature measurements. A Raspberry Pi single-board computer collects and records the data separately at $111\,\mathrm{Hz}$ for the fast sensors via a 24-bit analog-digital converter and at $2\,\mathrm{Hz}$ for the slow sensors. The slow and the fast data streams are synchronized by GPS time. The total mass of the instrument package is $1.2\,\mathrm{kg}$.

Calibration and data processing

The hot-wire sensor is calibrated for each flight against the wind velocity derived from the pitot-static probe,

$$u_\mathrm{p} = \sqrt{\frac{2\rho}{p_\mathrm{dyn}}}, \tag{3.9}$$

by means of a fourth-order polynomial regression (Jørgensen, 2005). The dynamic pressure p_dyn measured by the pitot-static probe has been calibrated in a wind tunnel against a highly accurate differential pressure gauge. The individual calibration for each flight is necessary to overcome the temperature dependence of the hot-wire reading. For intercomparison, simultaneous measurements of the HP and the UP

Tab. 3.3.: Instrument characteristics of the hot-wire anemometer package (HP) (first version).

Instrument	Manufacturer	Quantity	Range	Resolution
Hot-wire 55P11 with MiniCTA	Dantec Dynamics A/S, Denmark	u	0-50 $\mathrm{m\,s^{-1}}$	111 Hz
Thermocouple 5TC-TT-KI-10-1M	Omega Engineering, Inc., USA			
Transducer LKM 212 for thermocouple	LKM electronic GmbH, Germany	T	−20-80 °C	10 Hz
PT 100 with transducer LKM 467	LKM electronic GmbH, Germany	T	−20-80 °C	1 Hz
Pitot-static probe with differential pressure sensor AMS 5812 0000-D	AMSYS GmbH & Co. KG, Germany	p_{dyn}	0-5.17 hPa	2 Hz
Barometric pressure sensor AMS 5812 0150-B	AMSYS GmbH & Co. KG, Germany	p_{b}	760-1200 hPa	2 Hz
Humidity sensor EE08	E + E Elektronik GmbH, Austria	RH	0-100 %	1 Hz

are analyzed in Fig. 3.11, showing a vertical profile on 8 June 2017. Wind velocity measurements of all instruments agree well (Pearson correlation coefficient $R = 0.94$ between hot-wire and sonic sensors), as illustrated in Fig. 3.11a. Figure 3.11b compares energy spectra of hot-wire wind velocity for three constant-altitude segments. The hot-wire is able to resolve turbulent structures up to the Nyquist frequency $f_{\mathrm{Ny}} = 55\,\mathrm{Hz}$. The spectra are averaged over logarithmic equidistant bins without applying any anti-aliasing or low-pass filtering; therefore, a slight flattening or even an increase in the spectrum is visible at high frequencies. Further, the hot-wire spectra exhibit some irregularities in the frequency range of the balloon movement (around $0.1\,\mathrm{Hz}$), since the HP instrument motion cannot be compensated for. The spectral noise floor of the hot-wire sensor is below $10^{-7}\sigma^2\,\mathrm{Hz^{-1}}$. Therefore, a standard deviation due to uncorrelated noise of below $0.2\,\mathrm{cm\,s^{-1}}$ can be estimated.

Siebert et al. (2007) showed that impacting cloud droplets are visible in a hot-wire data set as sharp signal peaks with a duration of $\sim 0.5\,\mathrm{ms}$ at a given flow speed of $9\,\mathrm{m\,s^{-1}}$. The general influence of impacting droplets on the hot-wire reading is supposed to be smaller for Arctic clouds compared to the cases shown by Siebert et al. (2007) due the lower true airspeed for the balloon in combination with lower

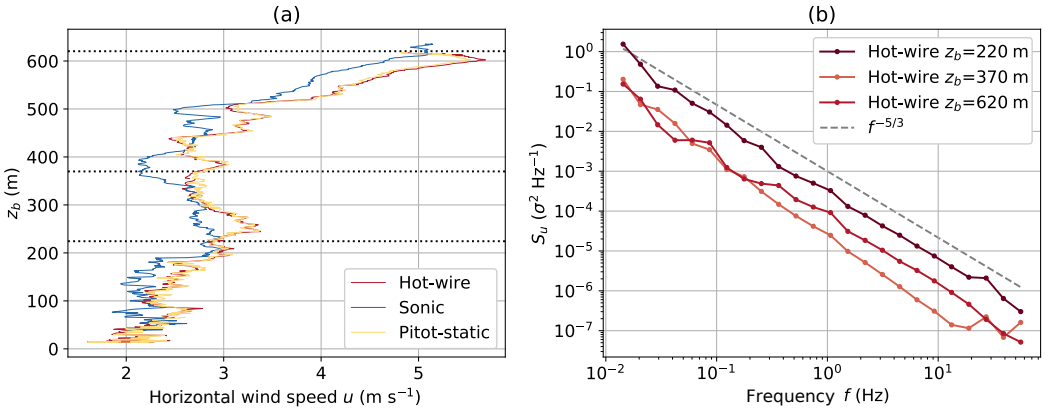

Fig. 3.11.: Horizontal wind velocity u measured on 8 June 2017 with UP and HP simultaneously. Panel **(a)** compares the vertical profile of wind velocity for measurements with the sonic anemometer, hot-wire anemometer and the pitot-static probe. The HP was attached $25\,\mathrm{m}$ below the UP. Panel **(b)** contrasts power spectral densities for horizontal wind velocity S_u measured with the hot-wire anemometer on three constant-altitude segments of $\sim 1000\,\mathrm{s}$ length (dotted horizontal lines in panel **a**). The data for the spectra were sampled during an ascent shortly before the descent profile of panel **(a)**.

droplet number concentrations. Further, the peaks include at maximum one data point because the sampling frequency is much smaller than the length of those spikes. The data spikes due to droplet impacts are eliminated with a simple filter algorithm, removing all single data values exceeding $5 \cdot \sigma_u$. Finally, the same filter algorithm is applied to filter spikes due to a technical problem with the data acquisition system.

Thermodynamic measurements with the HP, including applied corrections, are the same as for the UP (Sect. 3.2.3). Both temperature sensors on the HP show a small number of peaks in the data (on the order of $3\,\mathrm{s}$ to $4\,\mathrm{s}$ length and $1.5\,\mathrm{K}$ magnitude) on two days inside a cloud, possibly due to cloud droplet collisions. For the flight performed on 8 June 2017 (the only flight with simultaneous hot-wire and sonic measurements), the thermocouple data correlate with the sonic virtual temperature measurements with $R = 0.99$. The correlation of the RH measurement on UP with the HP measurement on the 8 June flight is $R = 0.98$, which shows good agreement between UP and HP thermodynamic measurements.

3.3.2 Second version of the hot-wire package

A second version of the HP (Fig. 3.12, Table 3.4) was deployed from 2018 on. The Raspberry Pi of the first version is replaced by an analog data logger to simplify the operation in the field and to make the instrument more robust. Apart from

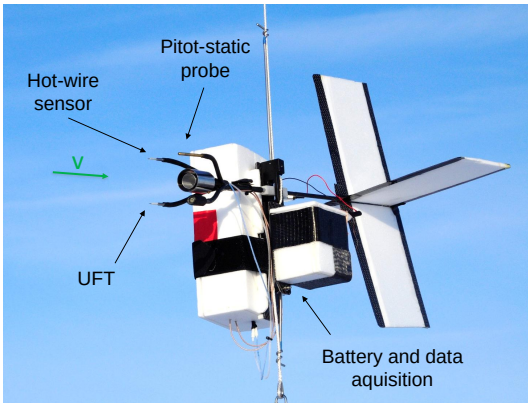

Fig. 3.12.: The hot-wire anemometer package (HP), version 2. The ultrafast thermometer (UFT) is not used in this work.

that, the general instrument setup is similar to the first version with a hot-wire anemometer and a pitot-static probe with a differential pressure sensor. The wind data are sampled by 12-bit analog inputs of the data logger at $500\,\mathrm{Hz}$. The data logger further provides measurements of external barometric pressure, temperature and RH at $1\,\mathrm{Hz}$ and records all data on an SD card. As this version of the HP is intended to operate at very cold temperatures, a heating pad warms the battery and prolongs operating time. An operating time of $3\,\mathrm{h}$ at temperatures below $-30\,^{\circ}\mathrm{C}$ was achieved.

Tab. 3.4.: Instrument characteristics of the hot-wire anemometer package (HP), second version.

Instrument	Manufacturer	Quantity	Range	Resolution
Hot-wire 55P11 with MiniCTA	Dantec Dynamics A/S, Denmark	u	$0\text{-}50\,\mathrm{m\,s^{-1}}$	$500\,\mathrm{Hz}$
Pitot-static probe with differential pressure sensor AMS 5812 0000-D	AMSYS GmbH & Co. KG, Germany	p_{dyn}	$0\text{-}5.17\,\mathrm{hPa}$	$500\,\mathrm{Hz}$
Data logger MSR165	MSR Electronics GmbH, Germany	T, p_{b}, RH	$-55\text{-}125\,^{\circ}\mathrm{C}$, $0\text{-}2000\,\mathrm{hPa}$, $0\text{-}100\,\%$	$1\,\mathrm{Hz}$

The data processing of the wind velocity measurements is performed similarly to the first version of the HP. The only difference is that the dynamic pressure is not calibrated in a wind tunnel, but ratiometrically related to the zero-wind pressure voltage and the maximum voltage of the differential pressure sensor. The HP has a higher temporal resolution than the first version and than the UP. Figure 3.13 shows

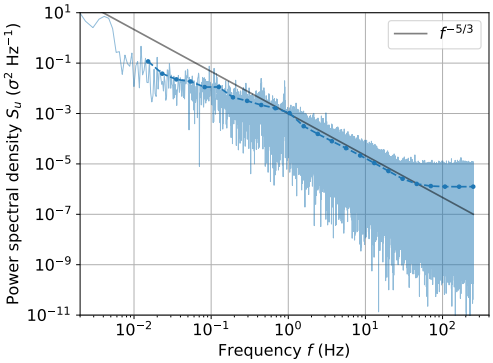

Fig. 3.13.: Second version of the HP: spectrum of a $28\,\mathrm{min}$ time series of hot-wire-based horizontal wind velocity recorded close to the surface.

the spectrum for a $28\,\mathrm{min}$ time series of hot-wire-based horizontal wind velocity, which was recorded close to the surface during PAMARCMiP[2]. The $500\,\mathrm{Hz}$ resolution and the spectral noise floor of $10^{-6}\sigma^2\,\mathrm{Hz}^{-1}$ indicate a standard deviation due to uncorrelated noise of $1.6\,\mathrm{cm\,s}^{-1}$ (Eq. 2.11). The temperature and RH data of the data logger feature very long response times, which smooth out the vertical profiles. Preferably, the temperature and RH measurements of the standard meteorology probe (Sect. 3.5) should be used, which was commonly operated simultaneously.

3.4 Broadband radiation package (BP)

The BP and the radiation data analysis are described by Gottschalk et al. (2018) and Egerer et al. (2019a). This section provides a brief summary. The BP measures solar and terrestrial, upward and downward irradiances (Fig. 3.14). Two downward- and upward-facing Kipp & Zonen CGR4 pyrgeometers cover the irradiance in the terrestrial spectral range between $4.5\,\mu\mathrm{m}$ and $42\,\mu\mathrm{m}$. Two Kipp & Zonen CMP3 pyranometers provide the solar irradiance in the spectral range between $0.3\,\mu\mathrm{m}$ and $2.8\,\mu\mathrm{m}$ in upward and downward direction. The pairs of pyranometers and pyrgeometers are mounted on a glass fiber rod, which is attached and leveled by a flexible mounting to the balloon tether. A wind vane aligns the instrument upwind and damps movement of the sensors. The sampling frequency is $12\,\mathrm{Hz}$ for the radiometers and $10\,\mathrm{Hz}$ for additional standard meteorological parameters. Combined with the housing and the battery, the total mass of the BP is $2.2\,\mathrm{kg}$. The solar and terrestrial irradiances are corrected for time response errors according to Ehrlich and Wendisch (2015). Data affected by icing are excluded from the data

[2] 2 April 2018, 12:25–12:53 UTC

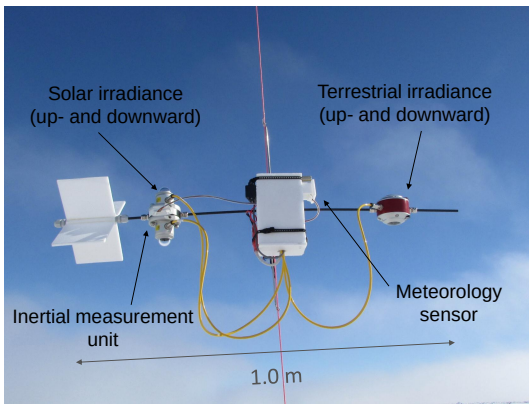

Fig. 3.14.: The broadband radiation package (BP)

analysis. Further, the misalignment of the sensors is considered when the sensors are exposed to direct solar radiation.

Tab. 3.5.: Instrument characteristics of the broadband radiation package (BP).

Instrument	Manufacturer	Quantity	Range	Resolution
CMP3 pyranometer (up- and downward)	Kipp & Zonen B.V., the Netherlands	$F_{\mathrm{net,sol}}$	0.3-2.8 μm	12 Hz
CGR4 pyrgeometer (up- and downward)	Kipp & Zonen B.V., the Netherlands	$F_{\mathrm{net,terr}}$	4.5-42 μm	12 Hz
Inertial measurement unit 10-DOF	Adafruit Industries, LLC, USA	ϕ, ϑ, ψ, p_{b}, T	250 $^\circ\,\mathrm{s}^{-1}$	10 Hz
Meteorology sensor BME280	Bosch Sensortec GmbH, Germany	p_{b}, T, RH	300-1100 hPa	10 Hz

The measured irradiances serve to calculate radiative heating rates. The local radiative heating rate is defined as the temporal change in temperature due to changes in the net irradiance $\partial F_{\mathrm{net}}$ with the altitude ∂z (Wendisch and Yang, 2012):

$$\zeta = \frac{\partial T}{\partial t} = \frac{1}{\rho \cdot c_{\mathrm{p}}} \frac{\partial F_{\mathrm{net}}}{\partial z}. \tag{3.10}$$

The net irradiance F_{net} is defined as the difference of downward and upward irradiance:

$$F_{\mathrm{net}} = F^{\downarrow} - F^{\uparrow}. \tag{3.11}$$

Configuration 3 of the balloon operation (Fig. 3.2) provides two approaches to obtain the radiative heating rate in a discrete layer Δz. The collocated approach

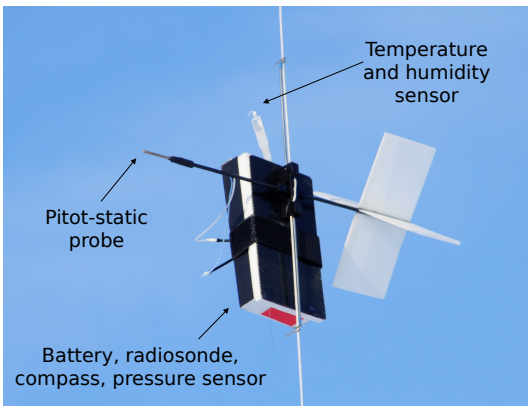

Fig. 3.15.: The standard meteorology package.

uses two identical BPs to calculate the heating rate for the layer between both platforms. The single-platform approach determines heating rates from analyzing the vertical profile of F_{net} measured by a single BP.

3.5 Standard meteorology package

The standard meteorology package is used to monitor the balloon measurements in real time on ground. During PASCAL, this was the only application of the standard meteorology. For PAMARCMiP, the standard meteorology was further developed and the measurements are used to complement the HP and BP with temperature, humidity and wind direction measurements. This version of the standard meteorology, used from 2018 on, is described here.

The basis for the standard meteorology (Fig. 3.15, Table 3.6) is a commercially available GRAW DFM-09 radiosonde, which provides measurements of T, RH, z_b, and GPS position at $1\,\mathrm{Hz}$. The standard radiosonde has the option to integrate a serial data stream via XDATA protocol into the data transmission, which allows to include additional measurements by a Pitot-static probe, a compass, and a small motion package. The digital differential pressure data of the Pitot-static probe together with attitude and heading information are pre-processed by an Arduino processor which creates the serial data stream (XDATA) feeding the radiosonde. This setup has the flexibility to include more sensors in the future, limited only by the small bandwidth allowed by the XDATA protocol. The wind velocity is derived from the dynamic pressure p_{dyn} of the differential pressure sensor. The Pitot-static probe is directed into the mean wind by a wind vane and the wind direction, derived from the compass, is calibrated towards true north (taking magnetic declination into

account). However, the measured wind direction must be treated with caution at locations close to the magnetic poles. The radiosonde and the additional sensors are included into a custom-made housing with a separate heated battery. For monitoring, all measured data are transmitted to a GRAW ground station, where they are also processed and recorded.

Tab. 3.6.: Instrument characteristics of the standard meteorology package.

Instrument	Manufacturer	Quantity	Resolution
GRAW DFM-09 radiosonde	Graw Radiosondes GmbH & Co. KG, Germany	T, RH, z_b, GPS position	1 Hz
HMC6343 Compass Module	Honeywell International Inc., USA	dd	1 Hz
Pitot-static probe with differential pressure sensor AMS 5812-0000-D	AMSYS GmbH & Co. KG, Germany	p_{dyn}	1 Hz

4 Application of turbulence data analysis methods

After introducing turbulence data analysis methods in chapter 2 and measurements with BELUGA in chapter 3, this chapter discusses how the data analysis methods are applied to the BELUGA measurements and how vertical profiles of turbulence parameters and turbulent fluxes are derived.

4.1 Determination of turbulent fluctuations

Determining the turbulent fluctuations in a time series is crucial for the subsequent turbulence analysis. The BELUGA measurement strategy introduced in Sect. 3.1.2, based on constant-altitude legs and vertical profiles, results in two methods to derive vertical profiles of turbulence parameters or turbulent fluxes. (i) Averaging over data segments at constant altitude yields a limited number of data points on the vertical profile, but a reasonable statistical basis for each data segment. The vertical resolution depends on the number of constant-altitude segments. (ii) A vertical profile with less statistical significance can be estimated from averaging over a certain time period or equivalent height range ("slant profiles") on a slow, continuous ascent or descent. The definition of the time period is a trade-off between vertical resolution and statistical robustness.

For the constant-altitude segments, turbulent fluctuations (according to Eq. 2.1) are obtained by removing any trend of the data time series. On the slant profile, turbulent fluctuations are determined using a high-pass 20th-order Bessel filter. The cutoff frequency for the filter

$$f_\mathrm{c} = \frac{U}{z_\mathrm{c}} \tag{4.1}$$

is given by the cloud layer thickness z_c and mean horizontal wind velocity U, and is in the range of $0.009\,\mathrm{Hz}$ to $0.025\,\mathrm{Hz}$ for PASCAL measurements. When turbulent motions at smaller scales are studied, a filter window of $10\,\mathrm{s}$ is applied, as proposed by Tjernström (1993) and Lenschow et al. (1988), who estimated turbulent fluxes from aircraft-based slant profiles. This can be particularly useful, when strong

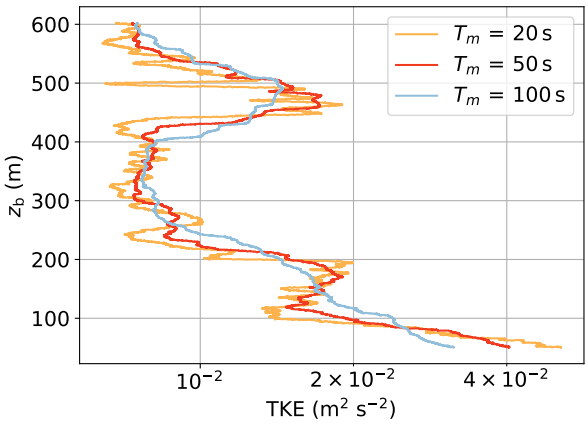

Fig. 4.1.: Comparison of averaging intervals T_m of $20\,\mathrm{s}$, $50\,\mathrm{s}$, and $100\,\mathrm{s}$ for TKE.

inversions occur because a filter with a large window might fail when gradients change rapidly.

4.2 Derivation of turbulence parameters

4.2.1 Turbulent kinetic energy

The vertical profile of TKE represents the stratification of turbulence in the ABL. The magnitude of the TKE (Eq. 2.3) depends on the averaging time for the wind velocity variances σ^2, since with a longer averaging time more larger, energy-containing eddies are sampled. On the slant profiles, TKE is calculated in a rolling window of a defined time span. Before, the low-frequency contributions to the signal are excluded by high-pass filtering as described in Sect. 4.1. Figure 4.1 compares the vertical profile of TKE derived from UP measurements for different averaging intervals of $20\,\mathrm{s}$, $50\,\mathrm{s}$, and $100\,\mathrm{s}$.[1] The general vertical structure of TKE is similar for all averaging intervals, with a finer vertical resolution for shorter averaging times. The magnitude of TKE is well represented with an averaging window of $50\,\mathrm{s}$. The averaging time of $50\,\mathrm{s}$ to $60\,\mathrm{s}$ is used as a standard for deriving TKE from slant profiles.

If with the HP only the horizontal wind velocity is available (instead of the three-dimensional wind vector with the UP), the variance of the horizontal wind σ_u^2 is regarded as an alternative for TKE. This is a valid assumption for stable ABLs, where the vertical σ_u^2 structure is equivalent to TKE profiles (Banta et al., 2006).

[1] The vertical profile data are from the same flight as in Fig. 3.11.

4.2.2 Dissipation rate

Section 2.1.3 introduced how the dissipation rate is retrieved from the structure function of a wind velocity time series. For BELUGA measurements, local dissipation rates ε_τ are derived using the second-order structure function (Eq. 2.14) for non-overlapping time periods of τ. A number of 200 measuring points per averaging period is common for determining ε_τ (Frehlich et al., 2003). Therefore, an averaging time of $\tau = 2\,\mathrm{s}$ to $\tau = 10\,\mathrm{s}$ (depending on the desired resolution of ε) is defined, which is shorter compared to the averaging time for the wind velocity variance. This is due to the fact that the dissipation rate is a small-scale, local parameter, whereas variances are influenced by the largest contributing eddies. The time periods τ can be from constant altitude legs or slant profiles. Time lags t^* in Eq. (2.14) are set to an empirical range between $0.1\,\mathrm{s}$ and $1\,\mathrm{s}$. For an inertial subrange behavior, the structure function is supposed to scale as $\varepsilon^{2/3}$. For the structure function in a time period τ, fitted exponents in the range between 0.3 and 0.9 are assumed to be close to inertial subrange behavior. If the fitted exponents are outside this range, no dissipation rate can be derived. Hence, the turbulent structures are too small to be resolved with the applied sensors. The minimum resolvable dissipation rate results when assuming that in Eq. (2.13) the structure function equals twice the standard deviation due to uncorrelated noise $D^2(r)_{\mathrm{min}} = \left(2 \cdot \sigma^{(\mathrm{n})}\right)^2$ at the minimum resolvable spatial distance $r_{\mathrm{min}} = U/f_s$:

$$\varepsilon_{\mathrm{min}} \approx 2.8 \cdot \left(\sigma^{(\mathrm{n})}\right)^3 \cdot \frac{f_s}{U}\,. \tag{4.2}$$

Thus, the minimum resolvable dissipation rate depends on the instrument characteristics and on the mean wind speed. Figure 4.2 shows an exemplary $6\,\mathrm{s}$ time series of w and the corresponding second order structure function. The t^* fit range for ε is step-wise reduced until the slope of the logarithmic fit is within the accepted range: here the slope is 0.49 within $0.1\,\mathrm{s} < t^* < 0.33\,\mathrm{s}$. Fitting Eq. (2.14) to the orange curve yields $\varepsilon = 4.8 \cdot 10^{-4}\,\mathrm{m^2\,s^{-3}}$ for the exemplary time series.

For the HP, local dissipation rates are calculated by applying the second-order structure function to the measured horizontal wind vector $u(t)$. For UP measurements, the vertical wind component $w(t)$ turned out to be yield more robust results for local dissipation rates. Figure 4.3 compares vertical profiles of local dissipation rates estimated from the HP and UP[2] for time segments of $2\,\mathrm{s}$ and $10\,\mathrm{s}$. The horizontal wind component u of the UP yields very few results for ε on the vertical profile and the values seem to be overestimated. The results for the UP w component

[2]The vertical profile data are as in Fig. 3.11 and Fig. 4.1.

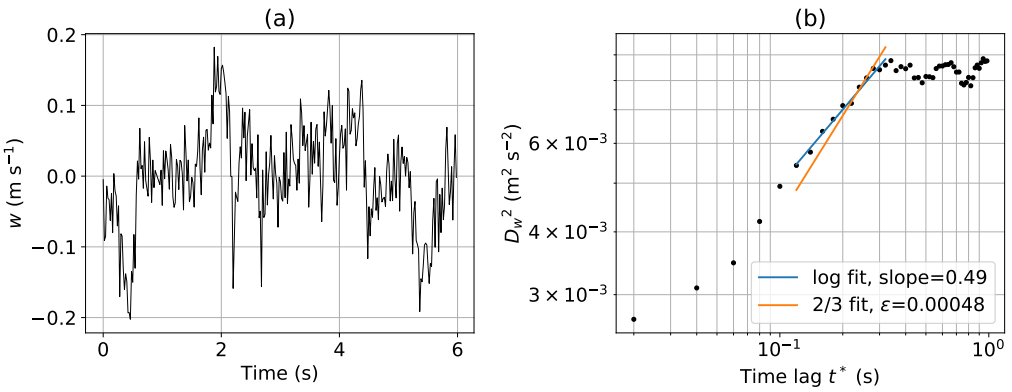

Fig. 4.2.: Exemplary time series of w **(a)** and determination of the local dissipation rate ε from the second-order structure function ${D_w}^2(t^*)$ **(b)**. The blue curve is a logarithmic fit with a variable slope, the orange curve represents a logarithmic 2/3 fit.

and for the HP agree well at stronger turbulence below $300\,\mathrm{m}$ altitude, although the estimates for UP are slightly higher (less than one order of magnitude). In the less turbulent region above $300\,\mathrm{m}$, the UP cannot resolve dissipation rates below $\sim 3 \cdot 10^{-4}\,\mathrm{m^2\,s^{-3}}$. Much lower dissipation rates down to $10^{-7}\,\mathrm{m^2\,s^{-3}}$ are resolved with the HP due to the higher measurement resolution. These values are close to the theoretical minimal resolvable dissipation rate (Eq. 4.2) of $7 \cdot 10^{-4}\,\mathrm{m^2\,s^{-3}}$ for the UP and $5 \cdot 10^{-7}\,\mathrm{m^2\,s^{-3}}$ for the HP at $U = 5\,\mathrm{m\,s^{-1}}$. Further, Fig. 4.3 compares averaging intervals of $2\,\mathrm{s}$ and $10\,\mathrm{s}$ for the HP. Both perform equally well in representing the vertical structure of ε. Because the dissipation rate depends on the smallest eddies in a flow, short averaging times are sufficient.

4.3 Turbulent energy fluxes

In Sect. 2.1.4, turbulent fluxes were introduced as a vertical energy exchange mechanism in the turbulent ABL. For BELUGA observations, the direct estimation of fluxes (the eddy covariance method) is combined with the gradient transport theory to obtain the vertical profile of turbulent virtual sensible heat fluxes and latent heat fluxes. Further, Sect. 4.3.2 discusses flux estimation errors of the eddy covariance method.

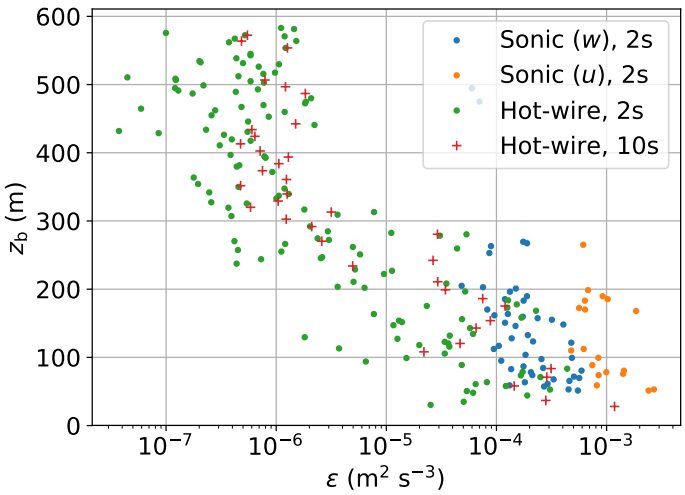

Fig. 4.3.: Vertical profiles of dissipation rates estimated from the HP and UP (from u and w wind velocity component) in averaging intervals of $2\,\mathrm{s}$ and $10\,\mathrm{s}$.

4.3.1 Estimation of turbulent fluxes

The eddy covariance method is used for estimating turbulent fluxes from BELUGA measurements. The turbulent fluxes of sensible heat H_S, latent heat L and momentum τ_uw result directly from the covariance of the measured fluctuations of vertical wind velocity w and the second quantity (Eqs. 2.15 to 2.17). The eddy covariance method is an established approach to estimate turbulent fluxes from masts or aircraft-based turbulence measurements. In the present work, I use the turbulent virtual heat flux H (Angevine et al., 1993), since the virtual temperature is directly measured by the sonic anemometer. The turbulent virtual heat flux, which is proportional to the buoyancy flux, results from the covariance of vertical wind velocity w and potential virtual temperature θ_v:

$$H = \rho \cdot c_\mathrm{p} \cdot \overline{w' \cdot \theta'_\mathrm{v}}\,. \tag{4.3}$$

The covariances are averaged over a defined time period T_m. On BELUGA, turbulent energy fluxes are estimated from measurements with the UP, since vertical wind vector component measurements are included. However, the eddy covariance method does not provide results for the latent heat flux L due to the lack of fast-response humidity measurements.

Applying the eddy covariance method requires sufficient long, stationary, and homogeneous records to provide time-averaged estimates of the covariances with statistical significance (Stull, 1988; Lenschow et al., 1994). Data records on constant-altitude

segments are assumed to be stationary and homogeneous and provide a single flux value for each altitude segment of typically $10\,\mathrm{min}$ length. In addition to averaging over time periods with constant altitude, the slant profile approach can be used by separating a continuous vertical profile into segments with a shorter averaging time. Here, I use $T_\mathrm{m} = 50\,\mathrm{s}$ for the slant profiles, which is similar to the values proposed by Tjernström (1993) and Lenschow et al. (1988). The slant profile method is based on the assumption that for a certain height (or time) range the profile data are considered as a homogeneous record and Eq. (4.3) can be applied. Instantaneous values of H are estimated for a defined height range, defining also the length scales contributing to the flux. Using this approach, the magnitude of calculated fluxes cannot be compared to fluxes with a longer averaging time, but they provide an idea about the vertical structure.

As an alternative to the eddy covariance method, the turbulent fluxes can be estimated with the flux gradient method (Eqs. 2.20 and 2.21) with the turbulent exchange coefficients K_H and K_Q. The prerequisite for applying the gradient method of a stable ABL with only weak turbulence is commonly fulfilled in the Arctic. The gradient method is particularly useful to estimate L from BELUGA measurements. Values of K are derived by directly applying Eq. (2.20) with the eddy-covariance H, yielding K_H. With $K_\mathrm{Q} \approx K_\mathrm{H}$ and the mean humidity gradient $\partial\overline{q}/\partial z$, combining Eqs. (2.21) and (2.16) results in L. The combination of the eddy covariance method and the gradient method allows to obtain vertical profiles of sensible and latent heat fluxes without a fast-response humidity sensor on BELUGA.

4.3.2 Turbulent flux errors

The estimation of turbulent fluxes with the eddy covariance method is prone to different errors. Vickers and Mahrt (1997) differentiate three main error sources:

- Systematic errors arise because parts of the spectrum (typically the larger scales) are systematically omitted when calculating the flux.
- Random errors result from a record which is not large enough for robust statistical evaluation.
- Inhomogeneity and non-stationarity will lead to incorrect flux estimates.

Lenschow et al. (1994) define the systematic errors as “systematic difference between the true flux and the ensemble average of the time means” and the random error as “variance of the time mean of the flux”. The averaging time T_m contributes to all

sources of error and, therefore, it is crucial to carefully define T_m. This averaging time for applying Eq. (4.3) is restricted by external factors, but at best is long enough to capture the largest eddies contributing to the covariance. For a given sampling time T_m, the systematic error ΔH and the random error ς_H of the flux calculation can be estimated using integral time scales τ_x and the correlation coefficient R (Lenschow et al., 1994):

$$\Delta H(T_\mathrm{m}) \leq \frac{2}{R} \cdot \frac{(\tau_{\theta_v} \cdot \tau_w)^{1/2}}{T_\mathrm{m}} \tag{4.4}$$

$$\varsigma_H(T_\mathrm{m}) \leq \frac{2}{R} \cdot \left(\frac{\min(\tau_{\theta_v}, \tau_w)}{T_\mathrm{m}} \right)^{1/2}. \tag{4.5}$$

More recent research (Petty, 2021), reviewing flux errors with large-eddy simulations (LES), show that the error estimates of Lenschow et al. (1994) are realistic approximations.

When averaging over the constant-altitude segments of typically $10\,\mathrm{min}$ to $15\,\mathrm{min}$, it is not possible to estimate statistically robust time averages of the turbulent fluxes. According to Eq. (4.5) and the conditions for the observation period (e.g., a low wind case with a mean horizontal wind speed of $2\,\mathrm{m\,s^{-1}}$ and integral timescales in the order of $\tau_w = 25\,\mathrm{s}$), averaging over around $200\,\mathrm{min}$ would be necessary to keep the statistical random error below $10\,\%$. Such long averaging times would result in very few results due to the limited total flight time. Therefore, the constant-altitude segments are restricted to relatively short time records of $T_\mathrm{m} = 620\,\mathrm{s}$ with the advantage of better resolving the vertical structure at a given time, instead of providing ensemble averages.

For the present work, typical integral time scales τ_w are around $25\,\mathrm{s}$ for turbulent regions and $2\,\mathrm{s}$ for less turbulent regions[3]. With $T_\mathrm{m} = 620\,\mathrm{s}$ for the height-constant periods and the correlation coefficient R, systematic flux errors range between $5\,\%$ for the less turbulent layers and $10\,\%$ for the more turbulent cloud and sub-cloud layers. Random flux errors are between $37\,\%$ and $48\,\%$. With averaging times of $T_\mathrm{m} = 50\,\mathrm{s}$, the systematic errors are up to $120\,\%$ and the random errors up to $170\,\%$. These numbers show, that especially the slant profile method is suitable for assessing the vertical structure of turbulence rather than actual flux magnitudes. The comparison also shows that it is difficult to directly compare the results for the eddy covariance method applied to slant profiles and constant altitude legs. Instead, it shows that an instantaneous measurement can deviate significantly from longer time averages. Further, both slant profile fluxes and constant altitude fluxes

[3] For PASCAL data of 5 June 2017, see Fig. 2.4.

might be impacted by mesoscale influences such as gravity waves or violations of a homogeneous and stationary sample, which are difficult to quantify.

5 Field campaigns

In the framework of the present thesis, BELUGA was operated during the two field campaigns PASCAL and PAMARCMiP in the Arctic. The campaigns are introduced in this chapter. For PASCAL, exemplary BELUGA measurements in three typical weather situations are presented to illustrate the potential of the new setup.

5.1 PASCAL (June 2017)

5.1.1 Overview

BELUGA with its three modular instrument packages was first deployed during the ship-based Arctic field campaign Physical Feedbacks of Arctic Boundary Layer, Sea Ice, Cloud and Aerosol (PASCAL; Macke and Flores, 2018), which is part of an extensive observational effort aiming at understanding atmospheric processes related to Arctic amplification (Wendisch et al., 2019). In the framework of the PASCAL campaign, the RV *Polarstern* (Knust, 2017) accessed the sea-ice-covered area north of Svalbard in June 2017, and drifted during a two-week period attached to an ice floe. PASCAL included substantial instrumentation from different research groups (Macke and Flores, 2018; Wendisch et al., 2019) and is associated with the concurrent aircraft campaign Arctic CLoud Observations Using airborne measurements during polar Day (ACLOUD; Ehrlich et al., 2019). During PASCAL, the $90\,\mathrm{m}^3$ tethered balloon was operated from an ice floe at around $81.8\,^\circ$ N from 5 to 14 June 2017. On the ice floe, the balloon site was established $200\,\mathrm{m}$ from the ship, close to a $10\,\mathrm{m}$ high mast for continuous meteorology and turbulence measurements. The tethered balloon was launched 16 times within nine operating days in clear-sky and cloudy conditions. During the first application of BELUGA at the PASCAL campaign, the operation of the balloon was not seriously affected by icing. A small amount of riming could be removed mechanically by hand and by the deflection pulleys ahead of the winch. In situations with more icing, the payload weight was reduced accordingly, resulting in more free lift, compensating for the additional accumulated weight of ice or snow on the balloon envelope. The same holds true for stronger wind conditions, where more free lift of the balloon resulted in more stable flight conditions. Typically,

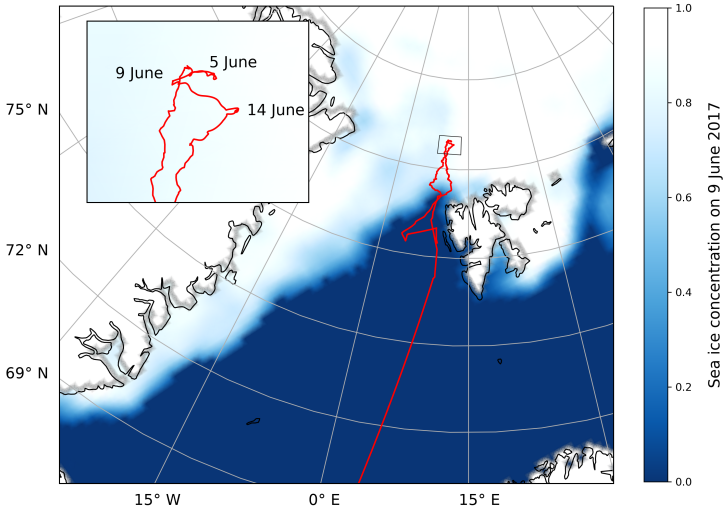

Fig. 5.1.: Track of RV *Polarstern* during PASCAL from Bremerhaven to the ice floe camp north of Svalbard, at around 81.8° N, 10.5° E. The ship drifted with the ice floe in the time period 3–16 June 2017. Sea ice conditions are plotted for 9 June (sea ice data from Maslanik and Stroeve, 1999a).

30 % of the free lift at ground (about 8 kg payload with a free lift of 25 daN for the balloon) was used for the instrumental payload under strong wind conditions, whereas in almost calm wind conditions the payload could be increased up to 10 kg to 12 kg. A list of all launches showing the individual configuration and the general meteorological conditions is given in Appendix B. The balloon and mast data are available via open-access (Egerer et al., 2019b; Egerer and Siebert, 2019). The balloon measurements are complemented by radiosoundings launched every six hours (Schmithüsen, 2017) and by ship-based remote sensing observations from a vertical-pointing, motion-stabilized cloud radar (Griesche et al., 2020c), a lidar (Griesche et al., 2020d), and a microwave radiometer of the OCEANET platform (Griesche et al., 2020a), which were processed with the synergistic instrument algorithm Cloudnet (Griesche et al., 2020b).

The observation period on the ice floe was characterized by a warm maritime air mass advected from the south and was influenced by a high-pressure ridge east of Svalbard (Knudsen et al., 2018). The sea-ice edge in the Fram strait was constant throughout the ice-floe period with an anomalously high sea ice extent. Cloud conditions were highly variable with an average cloud fraction of 65 %. Temperature and humidity inversions were present in most *Polarstern* radiosoundings during the ice-floe period. Figure 5.2 provides an overview of near-surface meteorological parameters and balloon flights during the ice-floe period. The period was characterized by relatively

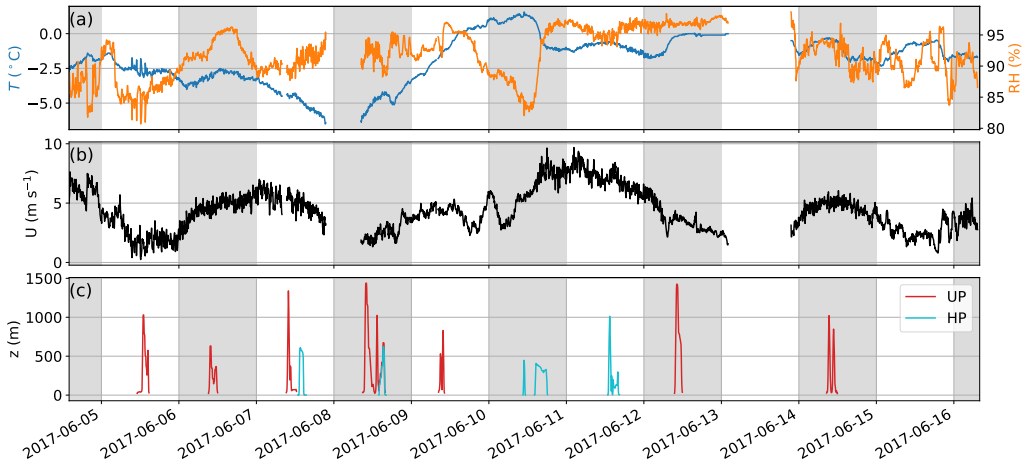

Fig. 5.2.: Time series of near-surface meteorological parameters and balloon flights during the ice floe period of PASCAL: **(a)** temperature T, RH and **(b)** wind velocity U from the $10\,\mathrm{m}$ mast and **(c)** flight altitude of the balloon flights with the UP and HP. Data gaps are due to power shortages on the ice floe.

stable conditions between 5 and 7 June, with a low-level cloud layer, temperatures ranging from $-1\,^{\circ}\mathrm{C}$ to $-4\,^{\circ}\mathrm{C}$, high RH, and low wind. Afterward, conditions were more variable, with changing temperature, RH, and wind due to changes in surface pressure (Knudsen et al., 2018). On 10 June, a distinct transition in temperature and RH took place although not associated with a frontal passage. This day also exhibits a maximum in wind velocity. Throughout the period, the near-surface temperature remained close to $0\,^{\circ}\mathrm{C}$ (despite warm air advection) due to the ongoing ice and snowmelt (Knudsen et al., 2018). The tethered balloon was operated under a variety of meteorological conditions. In the next section, three exemplary vertical profile measurements within the measurement period are presented to contrast different ABL and cloud conditions and to demonstrate the potential of the new BELUGA setup. The period 5–7 June with a layer of increased specific humidity above the persistent stratocumulus deck is analyzed in more detail in chapter 6.

5.1.2 Three measurement examples

A single-layer cloud: 5 June 2017

The first case analyzed here comprises an ABL with a single stratocumulus layer, which was typical for most days of the measuring period. For the presented case observed on 5 June, instrument configuration 1 (Fig. 3.2) with the UP and one BP was applied. The time series of the balloon altitude is shown in Fig. 3.3; it includes

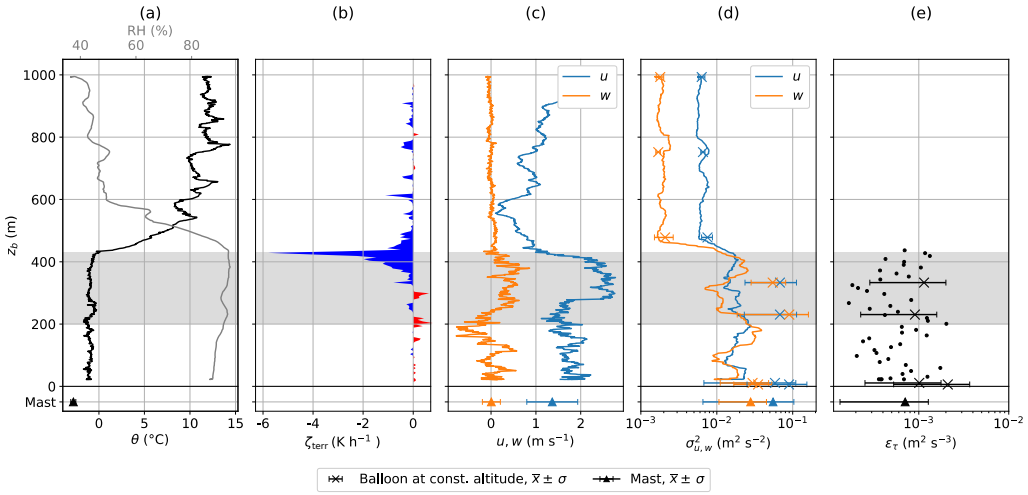

Fig. 5.3.: Vertical profiles observed on 5 June 2017 with a single-layer stratocumulus: potential temperature θ and relative humidity RH **(a)**, terrestrial heating rate ζ_{terr} **(b)**, horizontal wind u and vertical wind w **(c)**, local wind velocity variance $\sigma^2_{u,w}$ **(d)**, and the local dissipation rate ε_τ **(e)**. Solid lines and small dots show slant profile data measured during the ascent ($60\,\mathrm{s}$ running time window for variances, non-overlapping time segments of $10\,\mathrm{s}$ for dissipation rate). Crosses and corresponding horizontal bars in panels **(d)** and **(e)** show mean and standard deviation of dissipation rate and variances for measurements at constant altitude (segments of typically $10\,\mathrm{min}$) obtained during the descent. Averaged ground-based measurements at the meteorological mast are shown as triangles with the standard deviation indicated by horizontal bars. The cloud extent is indicated by gray shading.

a continuous profile followed by constant-altitude segments. The ABL stratification is characterized by a single, $200\,\mathrm{m}$ to $300\,\mathrm{m}$ thick stratocumulus layer close to the surface. The cloud base and top heights varied during the observation period due to spatial and temporal cloud heterogeneities. Therefore, it is challenging to exactly determine cloud top and base heights by the profiles of the balloon observations only. A combination of Cloudnet data (Griesche et al., 2020a), the relative humidity, and the location of the maximum cloud-top cooling from the balloon observations is used to define the cloud extent for the vertical profiles.

The vertical structure of the ABL and the derived turbulent and radiative parameters are shown in Fig. 5.3. The vertical profiles result from the first continuous ascent from the surface up to $1\,\mathrm{km}$ altitude. The ABL is characterized by a strong potential temperature inversion of $\sim$10.5 K within a $120\,\mathrm{m}$ thick vertical layer, capping the cloud layer and a nearly neutral sub-cloud layer. Above the inversion, the mean potential temperature slightly increases with height but shows several layers with temperature variations. Relative humidity is around $90\,\%$ below the cloud and decreases to $40\,\%$ above the cloud layer.

The terrestrial heating rate calculated by the single-platform approach is shown in Fig. 5.3b. A maximum cloud-top cooling of $5.5\,\mathrm{K\,h^{-1}}$ is observed at the cloud top. The colder cloud layer loses radiative energy to the warmer free troposphere above. At cloud base, weak warming of the lowest $30\,\mathrm{m}$ of the cloud layer by $1\,\mathrm{K\,h^{-1}}$ is observed. This cloud base heating indicates that at the cloud base, the terrestrial radiation emitted by the warmer underlying surface exceeds the emission by the colder cloud base.

Horizontal wind velocity is generally low with values around $2\,\mathrm{m\,s^{-1}}$ inside the cloud and $1\,\mathrm{m\,s^{-1}}$ above. A wind velocity maximum is observed in the upper half of the cloud, where the vertical wind velocity is positive (directed upward), whereas it turns negative at the cloud base. Figure 5.3d shows the vertical profile of horizontal and vertical wind velocity variances obtained from the continuous ascent (solid lines) and measurements at the constant-altitude segments (crosses). Variances are averaged over $60\,\mathrm{s}$ for both methods (consecutive intervals on the $10\,\mathrm{min}$ segments), resulting in a similar vertical structure and comparable magnitude. Maximum variances are observed below the inversion layer, with local maxima near the cloud top, cloud base, and surface. The difference between in-cloud and above-cloud variance for vertical wind velocity is one order of magnitude. Variances for vertical and horizontal wind velocity show similar values below the inversion, suggesting local isotropy. Within and above the inversion layer, the horizontal and vertical variances are close to the resolution limit, and no conclusion can be drawn about isotropy.

Figure 5.3e presents local dissipation rates ε_τ calculated for the slant profile, the constant-altitude segments, and the mast data. Below the inversion, ε_τ is in the order of $10^{-3}\,\mathrm{m^2\,s^{-3}}$ with the same vertical structure as wind velocity variances, but with higher variability. Above the inversion, ε_τ is below the resolution limit (cf. Sect. 4.2.2) and cannot be reasonably estimated. The majority of data derived from the slant profile are within the standard deviation of the measurements on constant-altitude segments. This indicates that the measurements of slant profiles are applicable to estimate local dissipation rates.

The combined turbulence and radiation measurements allow comparing irradiances and turbulent heat fluxes and calculating turbulent and radiative terms of the energy budget at different altitudes. For this purpose, the vertical profile of the net solar and terrestrial irradiances and the virtual heat flux observed on 5 June 2017 are shown in Fig. 5.4. The radiative fluxes are substantially larger than the turbulent fluxes and dominate the energy balance. In contrast to Eq. (3.11), here the net irradiance is defined as positive for upward-directed fluxes to maintain consistency for both

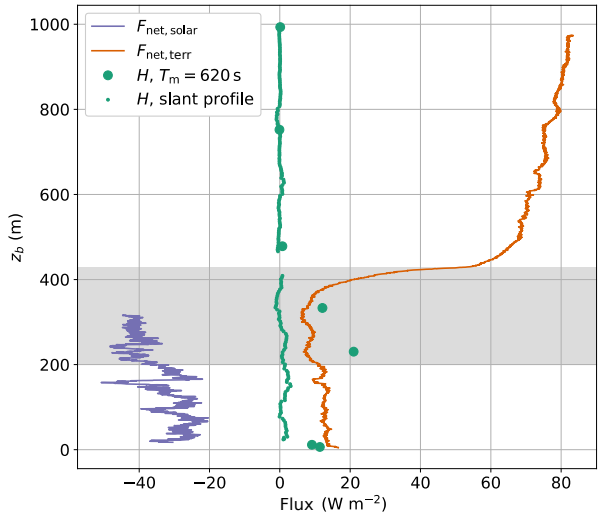

Fig. 5.4.: Vertical profile of virtual heat flux H and solar and terrestrial net irradiance F_{net} on 5 June 2017. Balloon-borne virtual heat fluxes (Eq. 4.3) are calculated from $620\,\mathrm{s}$ time periods at constant altitudes (big filled circles) and the slant profile with $T_{\mathrm{m}} = 50\,\mathrm{s}$ (dots). Positive values indicate upward-oriented fluxes.

radiative and turbulent fluxes. The upward-directed net terrestrial irradiance is almost constant between the surface and close to the cloud top. At cloud top, the net terrestrial irradiance increases from $10\,\mathrm{W\,m^{-2}}$ to $50\,\mathrm{W\,m^{-2}}$, and then slowly continues increasing with height. The solar irradiance is fairly constant below and within the cloud in a range between -20 and $-50\,\mathrm{W\,m^{-2}}$. The virtual heat flux obtained from the constant-altitude segments is most pronounced inside the cloud with a maximum near cloud base of $20\,\mathrm{W\,m^{-2}}$. Above the cloud, the virtual heat flux is close to zero. Near the surface, the virtual heat flux is around $10\,\mathrm{W\,m^{-2}}$. A sequence of virtual heat flux estimates on the mast with the same averaging time results in a similar mean value of $13\,\mathrm{W\,m^{-2}}$, but with high temporal variability (σ_{H} $=15\,\mathrm{W\,m^{-2}}$). The magnitude of the virtual heat flux derived from the slant profile is significantly smaller than the fluxes measured at constant altitude. Positive heat fluxes of up to $3\,\mathrm{W\,m^{-2}}$ are measured within the whole mixed layer. The cloud top region is excluded from the virtual heat flux calculation. Due to the strong change in the temperature gradient at the transition from the well-mixed layer to the inversion, the filter algorithm (Eq. 4.1) creates artificial fluctuations in this region, which results in unrealistic fluxes.

In the single-layer cloud case, turbulence is increased below and inside the cloud layer with upward-directed turbulent fluxes. Around cloud top, the increased turbulence can be explained by the cloud-top cooling. Inside the cloud and close to the surface, turbulence is induced by wind shear (the shear term in Eq. 2.24

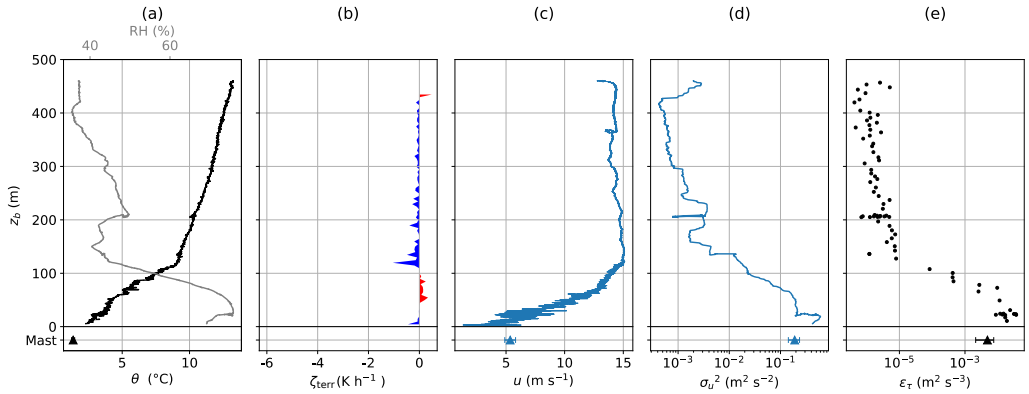

Fig. 5.5.: Same as Fig. 5.3, but for an ascent on 10 June 2017 in cloud-free conditions. The HP was applied to measure the horizontal wind velocity $\vec{u}$ and no constant-altitude segments were recorded.

dominates over the buoyancy term in these regions). Above the inversion, the stable stratification suppresses turbulent motions. The cloud layer substantially shapes the vertical profile of turbulence and radiation.

Cloudless case: 10 June 2017

For comparison, measurements collected during a cloudless day with strong wind speeds are presented. Due to the strong wind, only the HP and one BP (configuration 2) were deployed to reduce the payload. The balloon drifted horizontally around $500\,\mathrm{m}$ while not exceeding $500\,\mathrm{m}$ altitude.

Figure 5.5 shows the vertical profile of measured and calculated parameters obtained during a continuous ascent. The ABL exhibits a constant surface-based potential temperature inversion of $7\,\mathrm{K}$ in the lowermost $120\,\mathrm{m}$. The layer above still exhibits a stable stratification up to the maximum altitude. Relative humidity is around $80\,\%$ near the surface and decreases within the inversion to $40\,\%$.

Terrestrial heating rates are close to zero throughout the whole vertical profile with a change in sign at the inversion layer top height. Above the inversion, a weak radiative cooling is observed with a maximum of $1\,\mathrm{K\,h^{-1}}$ at the top of the inversion layer. Within the inversion layer, a slight warming of $0.5\,\mathrm{K\,h^{-1}}$ is present.

The horizontal wind velocity increases from $5\,\mathrm{m\,s^{-1}}$ near the surface to $15\,\mathrm{m\,s^{-1}}$ within the inversion layer and is nearly constant above. In contrast, the wind velocity variance constantly decreases with altitude. Turbulent dissipation is about $0.1\,\mathrm{m^2\,s^{-3}}$ near the surface and decreases inside the inversion down to $10^{-6}\,\mathrm{m^2\,s^{-3}}$. The layer

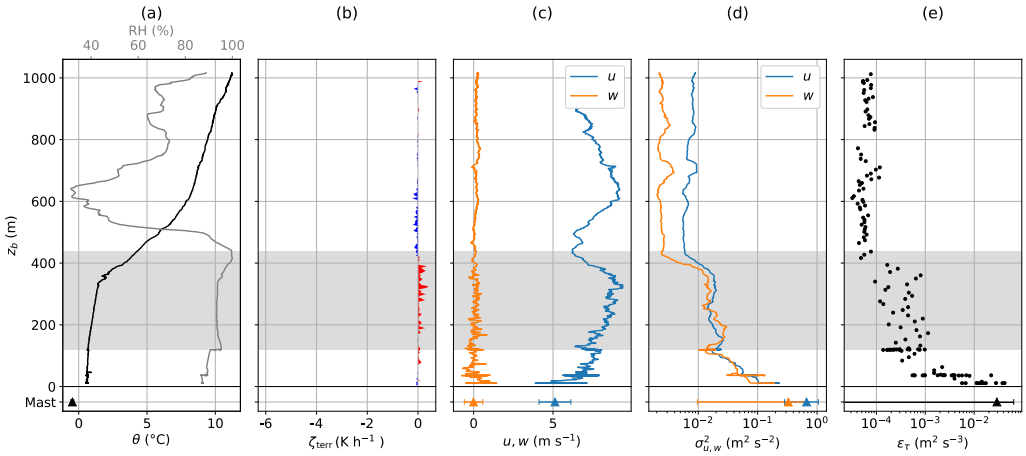

Fig. 5.6.: Same as Fig. 5.3, but for an ascent on 14 June 2017 with multiple cloud layers above $1\,\mathrm{km}$ height. No constant-altitude segments were recorded.

above reveals very weak turbulence, despite the high wind velocity. This example demonstrates the capability of the hot-wire probe to resolve energy dissipation rates down to below $10^{-6}\,\mathrm{m^2\,s^{-3}}$. As measurements were taken with the HP, no turbulent flux estimation is available.

In the cloudless case, the ABL exhibits a highly turbulent layer within the ground-based temperature inversion. The increased turbulence is induced by wind shear since the shear term exceeds the buoyancy term by an order of magnitude. For the layer above, the high wind velocity without significant wind shear and the stable stratification allow only little turbulence. Because no cloud is present, the turbulence profile is shaped almost exclusively by wind shear.

Multilayer clouds: 14 June 2017

On 14 June, a low-level stratocumulus layer up to a height of $500\,\mathrm{m}$ was observed together with multiple cloud layers extending from $1.2\,\mathrm{km}$ to $4\,\mathrm{km}$ altitude and topped by a cirrus cloud (detected by remote sensing data). The UP and two BPs (configuration 3) were applied to measure two continuous vertical profiles up to $1000\,\mathrm{m}$ between 09:00 and 11:00 UTC.

The boundary layer structure and derived turbulence and radiation parameters are shown in Fig. 5.6. The lower stratocumulus cloud is topped by a $7\,\mathrm{K}$, $250\,\mathrm{m}$ thick inversion layer. However, the relative humidity profile suggests that the cloud penetrates into the inversion layer. Terrestrial heating rates fluctuate close to zero

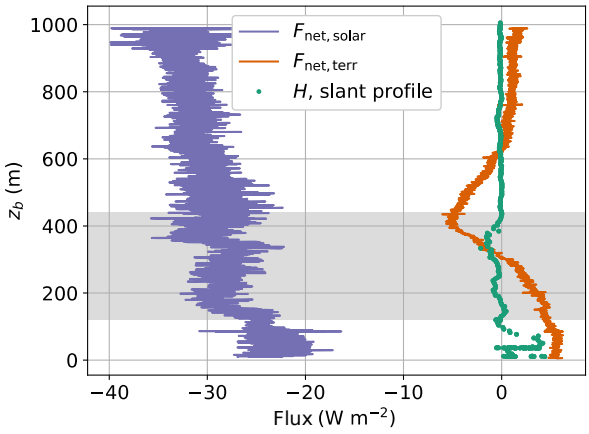

Fig. 5.7.: Solar and terrestrial net irradiance F_{net} and virtual heat flux H on 14 June. The virtual heat fluxes are based on the slant profile. The shaded area represents the lower cloud layer.

throughout the whole profile, with a slightly positive tendency below cloud top and a negative tendency above. This indicates slight warming of the layer below cloud top, similar to the warming of the inversion layer in the cloudless case.

The horizontal wind velocity increases from $6\,\mathrm{m\,s^{-1}}$ near the surface to a maximum of $8\,\mathrm{m\,s^{-1}}$ shortly below cloud top. A second maximum is observed in $600\,\mathrm{m}$ just above the inversion layer. In contrast to wind velocity, its variance decreases from the surface to cloud top with comparable values for the horizontal and vertical wind velocity variance. The vertical structure is similar for the dissipation rate with maximum values of almost $10^{-1}\,\mathrm{m^2\,s^{-3}}$ in the lowermost $30\,\mathrm{m}$, relatively constant values inside the cloud and less than $10^{-4}\,\mathrm{m^2\,s^{-3}}$ above the cloud. Between the surface and $380\,\mathrm{m}$ height, wind shear clearly dominates the buoyancy and produces turbulence with a maximum at the surface. Above $380\,\mathrm{m}$, the temperature inversion takes effect and limits turbulence.

Figure 5.7 illustrates the vertical profile of turbulent fluxes and net irradiances. Solar and terrestrial irradiances are smaller and less influenced by the low cloud layer than on 5 June 2017. The terrestrial irradiance shows an upward-directed flux of $5\,\mathrm{W\,m^{-2}}$ near the surface, and decreases towards cloud top to negative values. Above the cloud, the terrestrial flux is close to zero. Due to the cloud layer above, the terrestrial radiation emitted by the top of the lower cloud layer and by the base of the upper cloud layer is almost balanced. The virtual heat flux fluctuates around zero with a negative tendency inside the cloud, changing to positive values near the surface.

In the multilayer cloud case, turbulence in the lowest cloud layer is not induced by cloud-top cooling due to the other cloud layers aloft. Instead, increased turbulence at the surface level is the consequence of wind shear. Radiative fluxes are weaker than in the single-layer case, and the turbulence profile is mainly shaped by wind shear.

To conclude the three typical ABL situations, ABL clouds have the highest impact on the ABL structure when they are single-layer clouds and induce cloud-internal turbulence by cloud-top cooling. In cloudless situations or when higher cloud layers top low-level clouds, the turbulence profile is shaped by the relation between thermodynamical stratification and wind shear. For these cases, commonly surface-based wind shear induces the highest turbulence close to the surface. In the presence of higher cloud layers, the lower cloud layer has a significantly smaller influence on radiative and turbulent parameters compared to single-layer clouds. In all three cases, the net radiative fluxes are much higher than turbulent fluxes. The BELUGA measurements during these three atmospheric situations emphasize the value of collocated turbulence and radiation measurements with a high vertical resolution.

5.2 PAMARCMiP (March–April 2018)

For the second time, BELUGA was operated during the Polar Airborne Measurements and Arctic Regional Climate Model SImulation Project (PAMARCMiP) in the transition from winter to spring (Herber, 2019). PAMARCMiP was carried out in the period 10 March 2018 to 7 April 2018 at Villum Research Station (VRS), located at the Danish military base Station Nord, in northern Greenland ($81\,^\circ\,36\,'$ N, $16\,^\circ\,40\,'$ W). VRS is located at the Greenlandic mainland's coast between the Greenland ice sheet and the Arctic ocean, which is sea-ice covered almost all year round at this location. The campaign aimed at understanding the interaction between sea ice, aerosol particles, and clouds. Ground-based measurements at VRS were combined with tethered-balloon profiling and aircraft observations (Donth et al., 2020; Hartmann et al., 2020; Adachi et al., 2021). The tethered balloon was operated between 21 March and 4 April 2018 close to the Flygers hut at VRS (Fig. 5.8). This work focuses on a combination of BELUGA and ground-based measurements.

During the balloon operation period, the synoptical situation was influenced by high-pressure systems over central Greenland and the Northpole. The meteorological conditions were characterized by almost clear-sky conditions and were quite constant in terms of temperature, wind speed, and wind direction (Fig. 5.9). Near-surface temperatures were constantly below $-25\,^\circ$C, and RH was around $70\,\%$. The wind

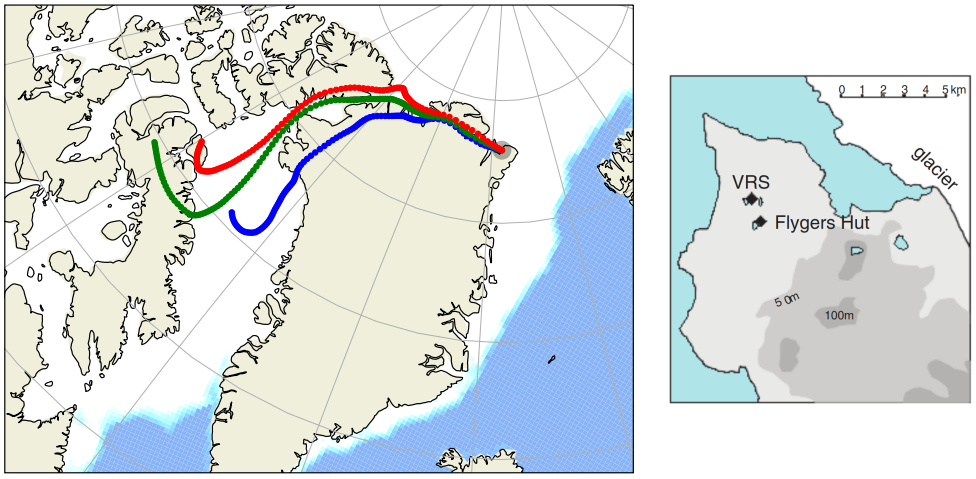

Fig. 5.8.: Location of Villum Research Station at Station Nord, Greenland, and detailed view of the station site. The sea ice extent is plotted for 29 March 2018 (Maslanik and Stroeve, 1999b). HYSPLIT back trajectories (Stein et al., 2015) are shown for 29 March 2018 (10 UTC) in altitudes of $50\,\mathrm{m}$ in blue, $100\,\mathrm{m}$ in green and $300\,\mathrm{m}$ in red. Station map adapted from Gryning et al. (2021).

speed was mostly below $5\,\mathrm{m\,s^{-1}}$ from the west. The westerly winds agree with back trajectory analyses for 29 March 2018 (Fig. 5.8), which show advection of air from the Canadian Arctic Archipelago. The influence of the high-pressure systems increased throughout the campaign. PAMARCMiP took place within the transition between Polar night and day, with a diurnal cycle in incoming solar radiation becoming stronger towards the end of the campaign.

In the measurement period, 49 BELUGA flights up to an altitude of $1500\,\mathrm{m}$ were conducted. Appendix B provides an overview of all flights. All data sets recorded during PAMARCMiP are available (Egerer et al., 2019c). BELUGA included the $9\,\mathrm{m^3}$ balloon and for each flight one HP or BP, accompanied by the standard meteorology package. The BELUGA instruments generally performed well under the cold conditions, and the instrument operating time (with heated batteries) was sufficient to endure several flights. A problem was the strong temperature difference between the environment of setting up the instruments inside the hut and outside conditions. The temperature and radiation sensors required some time to recover from the abrupt temperature change. Condensation or icing was not an issue due to the dry conditions. Occasionally thin clouds were present above $1000\,\mathrm{m}$ (ceilometer data; Gryning et al., 2021), but they were not sampled with BELUGA. A continuous surface-based temperature inversion up to $10\,\mathrm{K}$ in the lowest $100\,\mathrm{m}$ characterized the thermodynamic stratification observed with BELUGA. However, the vertical wind profile varied with wind maxima either below or above the inversion.

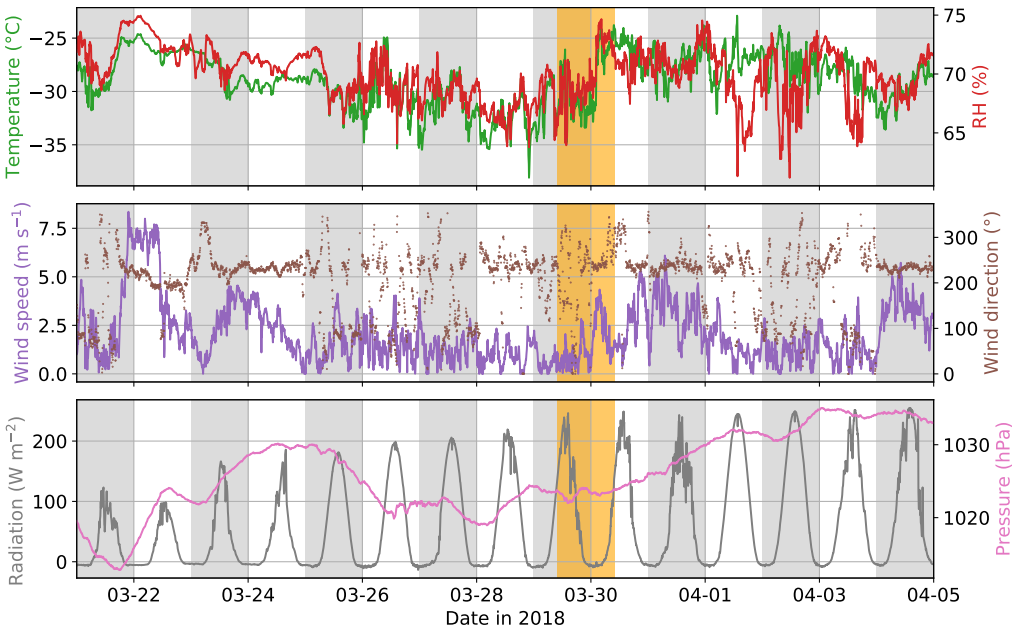

Fig. 5.9.: Meteorological conditions during the PAMARCMiP 2018 balloon operation period: temperature, RH, wind speed and direction (all at 9 m altitude), incoming solar radiation and surface pressure measured at VRS (Villum Research Station, 2018). The 24 h experiment is marked as orange shading.

A highlight of the BELUGA measurements is a 24 h profiling experiment on 29/30 March 2018. Radiation and turbulence instruments were deployed in turn on 15 BELUGA flights. Unfortunately, the night measurements (sunset at 21:30, sunrise at 05:00) were interrupted by some technical problems, but the profiling covers almost the entire diurnal cycle of the ABL structure. The vertical profiles for turbulence and radiation are one-of-a-kind data sets to characterize the cloud-free stable Arctic ABL. These data are analyzed in more detail in terms of a LLJ development in chapter 7.

6 Increased specific humidity above Arctic stratocumulus

In this chapter, a three-day period of a persistent layer of increased specific humidity above a stratocumulus is analyzed, as observed during PASCAL. Observed SHIs in a cloudy and cold environment might be influenced by measurement errors. Therefore, the SHIs measured with BELUGA are carefully validated. The vertical ABL structure around the SHI and the turbulent coupling of the SHI with the cloud layer is discussed. Finally, the impact of the SHI on the cloud is discussed using LES. This chapter is adapted and slightly modified after Egerer et al. (2021).

6.1 Specific humidity inversions (SHIs) in the Arctic

The phenomenon of SHIs, meaning specific humidity increasing locally with altitude, has been observed in all parts of the world but is particularly common in the Arctic. A number of studies on the climatology of SHIs have been published (e.g., Devasthale et al., 2011; Brunke et al., 2015; Naakka et al., 2018). SHIs occur most frequently over the Arctic ocean and are strongest in summer. In the lower troposphere, they often appear in conjunction with temperature inversions and high relative humidity but are also linked to the surface energy budget (Naakka et al., 2018). Formation processes and interactions of SHIs with clouds have been investigated in LES. For example, Solomon et al. (2014) showed that a specific humidity layer becomes important as a moisture source for the cloud when moisture supply from the surface is limited. Pleavin (2013) studied how the SHIs support the mixed-phase clouds to extend into the temperature and humidity inversion.

Mostly, the formation of the summertime SHIs is attributed to large-scale advection of humid air masses. In the Arctic, especially over sea ice, moisture advection is the critical factor for cloud formation and development (Sotiropoulou et al., 2018). SHIs form when warm, moist air is advected over the cold sea-ice surface and moisture is removed through condensation and precipitation from the lowest ABL part. This and further simplified formation processes are discussed by Naakka et al. (2018). When a SHI is located closely above an Arctic stratocumulus, it can provide

moisture that may drive the cloud evolution due to cloud-top entrainment. In contrast, in the typical marine sub-tropical or mid-latitude cloud-topped ABL, dry air from above is entrained into the cloud (Albrecht et al., 1985; Nicholls and Leighton, 1986; Katzwinkel et al., 2012). However, SHIs are not well represented in global atmospheric models, where the SHI strength is typically underestimated (Naakka et al., 2018), or the SHIs are not reproduced (Sotiropoulou et al., 2016).

Arctic SHIs have been observed during past field campaigns (Sedlar et al., 2012; Pleavin, 2013), e.g., during SHEBA and ASCOS. Sedlar and Tjernström (2009) used radiosondes and remote sensing to show that humidity inversions coincide with temperature inversions capping the cloud layer in the lower Arctic troposphere. For ASCOS, it has been shown that the depth of clouds penetrating into the temperature inversion correlates with the strength of the SHI (Pleavin, 2013).

The previous studies on SHIs have been based on radiosoundings, remote sensing observations, reanalysis data, or LES. Most observational studies rely on profiles of mean thermodynamic parameters from radiosoundings, which might be influenced by sensor wetting after cloud penetration in the SHI region. A systematic bias in radiosonde humidity measurements due to sensor wetting or other error sources is a serious concern when studying SHIs, particularly under moist and cold conditions. Therefore, one aim of this study is to carefully assess the validity of the SHI observations to exclude systematic biases. Moreover, the limited time resolution of radiosonde measurements does not allow for turbulence observations to analyze the exchange processes between the SHI and cloud top. To date, very few data are available to characterize and quantify the turbulent and radiative energy fluxes at SHIs. However, in particular the vertical turbulent exchange of mass and energy is necessary to understand the importance of SHIs for cloud evolution and lifetime.

To investigate the exchange processes between the cloud layer and the SHI, I analyze BELUGA high-resolution vertical profile measurements of turbulence and radiation in a three-day period during PASCAL. The observations are complemented by LES for the same period. I focus on a detailed case study with a persistent SHI above a stratocumulus deck to answer the research question: how are the SHI and the cloud top connected by turbulent mixing?

6.2 Specific humidity measurements in a cloudy environment

Before addressing the research question, the validity of measured SHIs is reviewed. A cold and moist environment poses considerable challenges for the measurement of specific humidity. This can lead to measurement artifacts in the region of the SHI. To exclude measurement artifacts as the cause of the observed SHIs, in this section, I discuss the measurement of specific humidity with BELUGA and radiosondes as well as possible sources of error and their effects. Specific humidity q is derived from air temperature T and RH using

$$q = \frac{R_\mathrm{d}/R_\mathrm{v} \cdot e_\mathrm{s}(T) \cdot \mathrm{RH}}{p - (1 - R_\mathrm{d}/R_\mathrm{v}) \cdot e_\mathrm{s}(T) \cdot \mathrm{RH}}\,, \tag{6.1}$$

with the static pressure p, the ratio of specific gas constants of dry air and water vapor $R_\mathrm{d}/R_\mathrm{v} \approx 0.622$, and the temperature-dependent saturation vapor pressure $e_\mathrm{s}(T)$. In this study, the measurements of RH and T are obtained by regular radiosoundings (Vaisala RS92-SGP) and observations with the BELUGA system. Both methods use capacitive RH sensors, suffering from several limitations (Wendisch and Brenguier, 2013).

6.2.1 Measurement issues in high-humidity conditions

Several studies address the associated systematic errors of radiosonde RH and T measurements and identify three main sources, (i) wet-bulbing, (ii) solar heating, and (iii) time response errors:

i. Wet-bulbing occurs when a water film develops on the sensor during cloud penetration, with subsequent evaporative cooling under sub-saturated conditions above the cloud. This effect leads to an overestimation of RH and underestimation of T in the sub-saturated environment until the water film has completely evaporated. Jensen et al. (2016) show that wet-bulbing is an issue for the radiosonde type used during PASCAL. However, the error induced by wet-bulbing is difficult to quantify (Dirksen et al., 2014).

ii. Exposure of an RH sensor to direct sunlight above a cloud causes a radiation dry bias (measured RH is too low) of up to $5\,\%$ in the lower troposphere (Miloshevich et al., 2009; Wang et al., 2013). The error is corrected in the radiosonde data processing algorithm (Jensen et al., 2016). However, this

correction is intended for cloud-free conditions. Solar heating also influences temperature measurements (Sun et al., 2013), but the effect on radiosonde temperature is negligible at low altitudes. For BELUGA, the temperature and RH sensors are shielded against direct solar radiation, but the sensor surroundings might warm and influence the measurements.

iii. Furthermore, the time response for RH and T measurements is finite. Compared to the effects (i) and (ii), this part of the sensor behavior can be quantified by the time constant τ. Assuming a first-order sensor response, the time dependence of a measured signal $x_{\mathrm{m}}(t)$ (RH or T in this case) is given by Eq. (3.5). The time-lag-corrected signal results from Eq. (3.8) (Miloshevich et al., 2004).

Although radiosonde data processing routines consider the time response error, fast humidity changes in cold conditions are still affected (Smit et al., 2013; Edwards et al., 2014). The time constants for the BELUGA RH sensor were estimated in a laboratory study (see Sect. 3.2.4) and are $\tau_{\mathrm{RH}} \approx 50\,\mathrm{s}$ for RH and $\tau_{T_{\mathrm{s}}} \approx 70\,\mathrm{s}$ for the sensor-internal temperature. The time constant for the T measurements based on the thermocouple on BELUGA was found to be below $1\,\mathrm{s}$ (Sect. 3.2.3) and, thus, has a minor influence on the vertical temperature profile compared to the humidity observations.

6.2.2 Sensitivity of specific humidity to the RH and temperature profile

Sensitivity studies are performed to analyze how the three error sources (Sect. 6.2.1) for T and RH measurements combine and influence the derivation of q. The errors are simulated as T and RH deviations from a synthetic reference case (grey line in Fig. 6.1), representing a simulated measurement of a temperature inversion combined with a decrease in RH. The temperature linearly increases by $6\,\mathrm{K}$ in the $200\,\mathrm{m}$ thick inversion layer, whereas RH linearly decreases from $100\,\%$ to $40\,\%$ in the same height range, resulting in monotonically decreasing specific humidity without a SHI.

First, I consider the influence of possible measurement errors in the temperature inversion region for the T and RH sensor separately. That is, only one sensor will be influenced by an increased or decreased signal while keeping the other sensor reading at the reference value. The magnitude of the simulated deviations (Fig. 6.1a

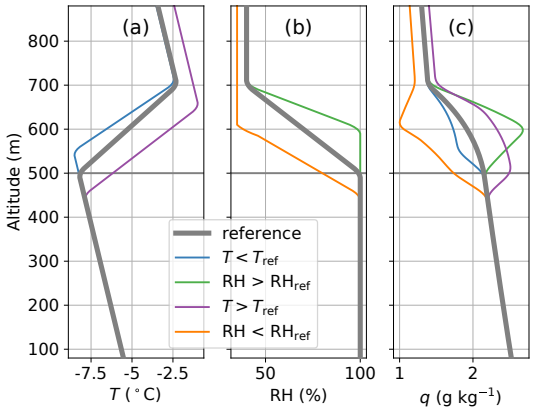

Fig. 6.1.: Sensitivity of the vertical q profile to a deviation of T and RH compared to a reference case (grey line). Only one parameter (T or RH) experiences a deviation in the inversion region; the other parameter is unchanged. Underestimated temperature (blue) or overestimated RH (green) might result from wet-bulbing. Overestimated temperature (purple) or underestimated RH (orange) might result from solar heating. A slow-response RH sensor overestimates RH on the ascent (green) and underestimates RH on the descent (orange).

and b) is arbitrary, but the qualitative profile of the affected signal is according to the error sources, as discussed in Sect. 6.2.1.

The effect of the four errors (T or RH too high or too low in the temperature inversion region) on the specific humidity profile is shown in Fig. 6.1c. An artificial humidity layer above the cloud can emerge when the RH sensor overestimates the moisture due to wet-bulbing (but keeping the temperature sensor unaffected), or when the temperature sensor is heated in the inversion region, but the humidity sensor is unaffected. Vice versa, q shows a deficit compared to the reference when one of the sensors indicates underestimated values compared to the reference scenario. If a single phenomenon affects both the temperature and RH sensor (e.g., solar heating results in underestimated RH and overestimated temperature), the errors in the determination of q have an opposite effect and, therefore, the overall error in q is reduced.

As a second step, I simulate the influence of different time constants τ_{RH} and τ_T for the RH and temperature measurements. If both time constants have similar values; the resulting q does not change significantly in magnitude, but the vertical structure shifts upwards or downwards for an ascent or descent. With a slow-response RH sensor ($\tau_{\mathrm{RH}} \gg \tau_T$), the measured RH in the SHI region is overestimated on the ascent and underestimated on the descent with the effects on q as shown in Fig. 6.1c and with an artificial SHI on the ascent.

As a result of these sensitivity studies, the error in q is reduced when both the temperature and humidity sensors are affected by the same error source (e.g., solar heating on both sensors), and when both sensors have comparable time constants. Under these conditions, a detected SHI can be considered as most likely real and does not need to be interpreted as an artifact.

6.2.3 SHIs measured with BELUGA and radiosondes: natural feature or artifact?

This section aims to verify that the SHIs measured during PASCAL with radiosondes and BELUGA represent a natural feature and not a measurement artifact. A simple and convincing test of the possible influence of the error sources on the SHI observations is profiling in opposite direction, that is, a descent from the free troposphere through the SHI into the cloud layer. This is commonly impossible in case of standard radiosoundings but feasible for the BELUGA observations. Figure 6.2 shows vertical profiles of RH, T, and q as measured by radiosounding and BELUGA on 5 June 2017. Qualitatively, the measurements of both platforms show a similar vertical structure with a sharp temperature inversion capping the cloud layer. The cloud top (estimated from the observed downward terrestrial irradiance) is situated close to the temperature inversion base. However, the cloud top height derived from radiation observations should be treated with caution due to the vertical separation of the radiation and thermodynamic sensors by about $20\,\mathrm{m}$, corresponding to a temporal shift between the observations of about $20\,\mathrm{s}$ during profiling. In the measurement period of almost 2 h, the temperature inversion base and the cloud top remain at almost constant altitude. The radiosonde observation shows a layer of increased q between $400\,\mathrm{m}$ to $550\,\mathrm{m}$ altitude just above the temperature inversion base. The increased specific humidity emerges from RH remaining high within the temperature inversion, before decreasing to the free troposphere level well above the inversion base.

Before comparing the q measurements from the radiosonde to BELUGA observations, I illustrate the effect of the applied RH correction and the consequences for the q profile. Figure 6.2a shows the uncorrected and time-response corrected RH for an ascent and descent. The uncorrected RH ascent profile deviates strongly from the descent in the cloud top region. While descending through the cloud, the sensor requires a $150\,\mathrm{m}$ height difference for rising from $55\,\%$ to $95\,\%$ RH. The RH hysteresis around the cloud top is visible as a systematic deviation in all observed flight data (not shown). A comparison to Fig. 6.1 (orange lines) suggests that the major part of

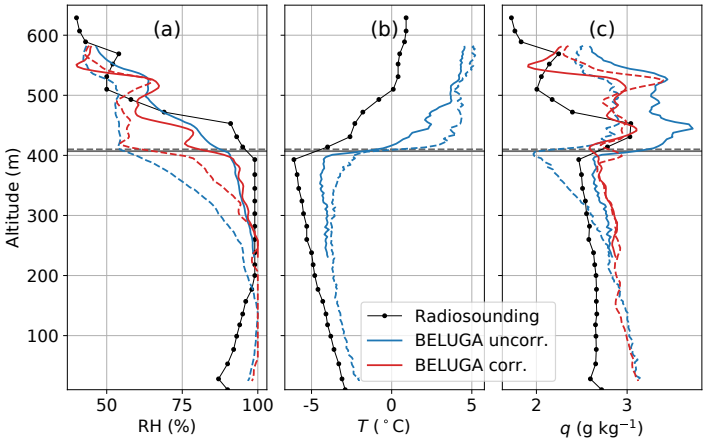

Fig. 6.2.: Vertical profiles of **(a)** relative humidity RH, **(b)** temperature T, and **(c)** specific humidity q measured by a radiosonde and BELUGA on 5 June 2017 (second profile). RH and q for BELUGA are shown before and after the corrections. The radiosonde was launched at 16:50 UTC; the balloon flew a continuous ascent and descent from 14:27 to 14:40 UTC. The cloud top (from BELUGA radiation data) is shown as horizontal lines. Solid and dashed lines represent the BELUGA ascent and descent, respectively.

the error is due to a slow RH sensor. Furthermore, the sensor underestimates RH in the cloud on the descent, which might indicate solar heating. After applying the time lag correction, the RH profile shows a significantly reduced difference between ascent and descent. The remaining difference is qualitatively consistent with the temperature observations, as shown in Fig. 6.2b. The temperature profiles show a warming of the cloud top and inversion region between $300\,\mathrm{m}$ and $500\,\mathrm{m}$ during the descent leading to a reduced RH.

The “uncorrected” specific humidity in Fig. 6.2c is calculated from the uncorrected RH and the temperature measured with the fast-response thermocouple. The resulting q profiles show a SHI on the ascent and the descent of the BELUGA flight with a similar structure and location compared to the radiosonde data. The q profile as observed during the descent is shifted to lower q values in the region of the hysteresis of the uncorrected RH.

The corrected q results from the RH and the sensor-internal temperature T_s after correcting both signals for the time lag error according to Eq. (3.8). Low-pass filtering in Eq. (3.8) is realized by a Savitzky–Golay filter with a window length of the time constant τ. This low-pass filtering is necessary to avoid amplification of gradients caused by signal noise or digitization steps (Miloshevich et al., 2004). For calculating q, I argue that using T_s should be preferred instead of the thermocouple readings because RH and T_s have similar time constants, and RH is measured

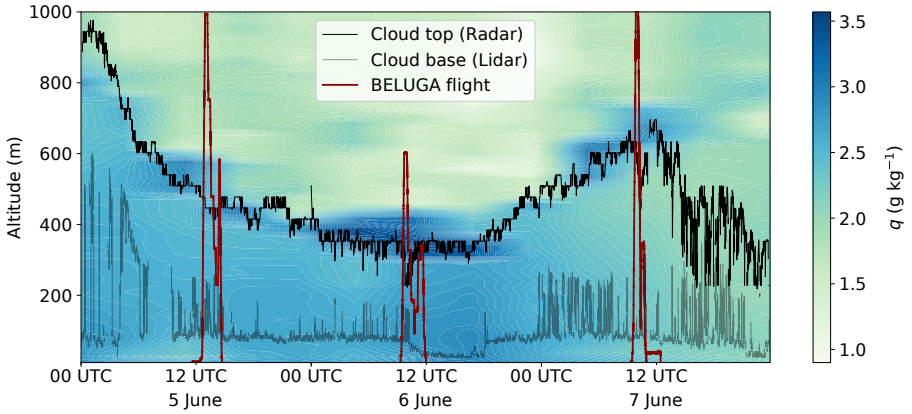

Fig. 6.3.: Temporal development of the specific humidity vertical profile observed by radiosondes. The radar-retrieved cloud top height is depicted as a black line; the cloud base height derived from the lidar near-field channel is indicated as a grey line. The red lines represent the BELUGA flight profiles.

at T_s instead of the temperature of the atmospheric environment. The ambient temperature and T_s differ slightly due to the thermal inertia of the sensor housing.

After applying the corrections, the maximum value of the SHI, as observed during the BELUGA ascent, is reduced by about $0.6\,\mathrm{g\,kg^{-1}}$ compared to the uncorrected q maximum. After correction, all BELUGA profiles and the radiosonde data exhibit the SHI with similar structure and amplitude. This consistency suggests that the observed SHI is a natural feature instead of an instrumental artifact. Wet-bulbing can be excluded as the main reason for the observed SHIs because the SHI is also present during the descent. The influence of solar heating and time-lag errors is minimized. The conclusion also strengthens the confidence in SHIs as frequently observed by radiosondes.

6.3 Observation period

6.3.1 Observed humidity inversions

The present study is based on measurements with BELUGA during PASCAL in the period 5 to 7 June 2017, complemented by radiosoundings and ground-based remote sensing. The observational basis is a layer of increased specific humidity above a persistent single-layer stratocumulus deck which was present throughout the observation period. Figure 6.3 illustrates the temporal development of the vertical specific humidity profile derived from radiosonde measurements. Cloud top and

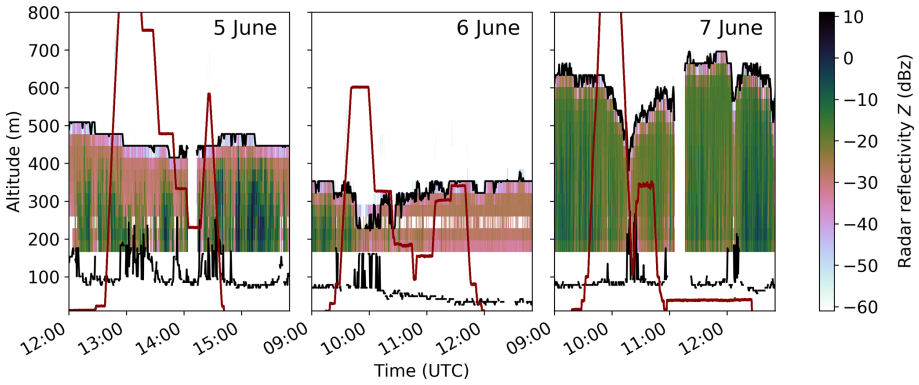

Fig. 6.4.: BELUGA flight profiles for 5, 6, and 7 June (red lines) with the radar reflectivity Z and cloud boundaries (black lines, as in Fig. 6.3).

bottom and the time–height curves of the corresponding BELUGA flights are added for the investigated period. The BELUGA flights were conducted around noon on each of the three consecutive days. A local maximum of specific humidity is observed above the cloud top throughout almost the entire period, with a slight diurnal cycle peaking at noon and a maximum specific humidity on 6 June. It is worth noting that the observations show a well-defined layer of increased specific humidity, hereafter referred to as the humidity layer, rather than a distinct and sharp SHI with only a slight decrease above.

The cloud top and base height in Fig. 6.3 are estimated from the cloud radar and lidar (near-field channel) data, averaged over $30\,\mathrm{s}$ and with a vertical resolution of $30\,\mathrm{m}$. Throughout the three-day period, cloud height and thickness decrease to a minimum at noon of 6 June, and thereafter increase again. The cloud is almost permanently of mixed-phase type with a maximum LWC between $0.15\,\mathrm{g\,m^{-3}}$ and $0.6\,\mathrm{g\,m^{-3}}$ and an estimated ice water content (IWC) of about $0.03\,\mathrm{g\,m^{-3}}$ derived from Cloudnet data (not shown here).

Figure 6.3 suggests high variability in cloud top and bottom heights. To illustrate the cloud situation around the BELUGA flights in more detail, Fig. 6.4 shows the radar reflectivity and cloud boundaries for the particular three balloon flights. On 5 June, the cloud top height is approximately constant, whereas on 6 June the cloud top fluctuates between $350\,\mathrm{m}$ and $230\,\mathrm{m}$ in the course of the flight. During the 7 June flight, the cloud layer thins by $110\,\mathrm{m}$ starting from the cloud top.

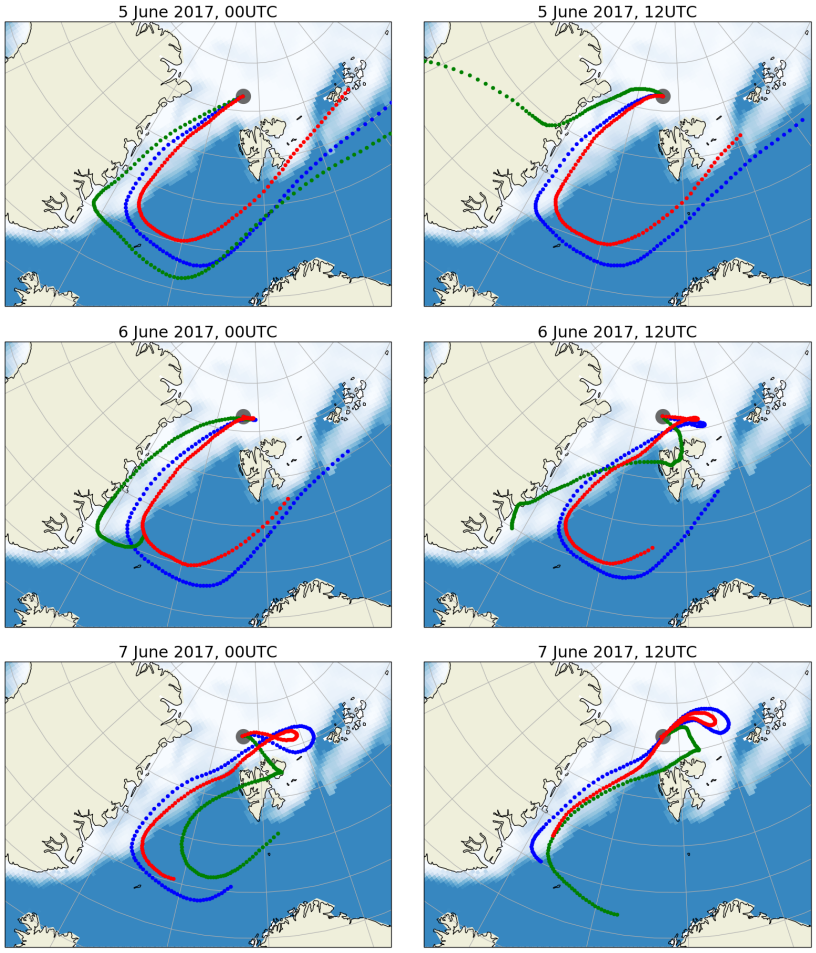

Fig. 6.5.: Five-day back trajectories ending at RV *Polarstern* (gray dot) at 00:00 and 12:00 UTC between 5 and 7 June 2017 in altitudes $50\,\mathrm{m}$ (red), $250\,\mathrm{m}$ (blue) and $1000\,\mathrm{m}$ (green). The trajectories are calculated using HYSPLIT (Stein et al., 2015).

6.3.2 Air mass origin

Before exploring the interactions of the SHIs with clouds, I briefly discuss the possible formation of the SHIs, which is commonly associated with warm and moist air advection. The conceptual model of Tjernström et al. (2019) for air mass transformation during moist and warm air advection over open water and sea ice (Fig. 2.10) describes how the well-mixed ABL with a persistent cloud layer develops, which has been frequently observed in the Arctic. During the air mass transformation, the cooling within the ABL results in condensation and subsequent precipitation, which reduces the specific humidity. Specific humidity above the ABL is not affected and, as a result, a SHI at the top of the ABL forms.

Figure 6.5 shows back trajectories of the air masses for the study period between $50\,\mathrm{m}$ and $1000\,\mathrm{m}$ altitude. The trajectories are calculated using the Hybrid Single-Particle Lagrangian Integrated Trajectory model (HYSPLIT; Stein et al., 2015). The air mass during the study period originates further south in the Arctic ocean and is advected over open water and sea ice. Towards the end of the period, the air mass resides locally over the sea ice after being advected.

If the conceptual model of Tjernström et al. (2019) is applied to the air mass history in the study period, the state at RV *Polarstern* corresponds to the final state with an elevated temperature and humidity inversion above the mixed layer and a cloud deck. Also, Knudsen et al. (2018) describe the ice floe period as climatologically warm with advected warm and moist maritime air masses. I conclude that the formation of the humidity layer is probably a result of warm air advection over sea ice.

6.4 Vertical profiles of mean ABL parameters

6.4.1 Normalized temperature and humidity profiles

Throughout the observation period, a persistent layer of increased specific humidity was observed above the cloud layer. One of the governing questions of this analysis is to understand how observed SHIs relate to the general ABL structure and, in particular, to the temperature inversion. Figure 6.6a and b show vertical profiles of potential temperature θ and specific humidity q recorded in the period of 5–7 June 2017. Both parameters are normalized with their near-surface values and plotted in relation to the base height of the temperature inversion z_i. The cloud boundaries are shown in Fig. 6.6c for reference.

All measurements show a similar vertical structure of θ within the ABL. Below the temperature inversion base z_i, the stratification is near-neutral to weakly stable. Above the inversion, the thermodynamic stability is higher and exhibits more variability compared to below the inversion. No systematic difference between ascents and descents is visible. The ABL is thermodynamically coupled to the surface, which makes normalizing to surface values meaningful.

Within the mixed layer below z_i, specific humidity decreases slightly with height but increases when reaching z_i. Above z_i, the normalized specific humidity exhibits more variability compared to the normalized temperature. The descent of 7 June $09\mathrm{h}$ shows a temperature inversion with some internal structure in the form of two smaller “steps” in θ. I define z_i at the lower step, with the SHI base being located

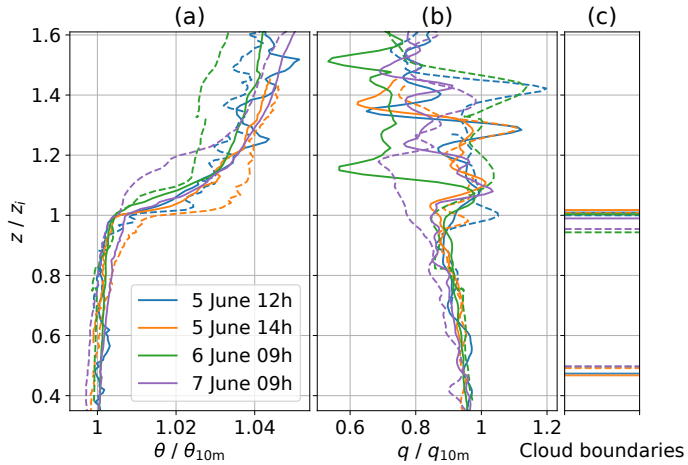

Fig. 6.6.: Balloon-borne vertical profiles of **(a)** potential temperature θ, **(b)** specific humidity q, and **(c)** cloud boundaries for four ascents (solid lines) and descents (dashed lines) on 5, 6, and 7 June 2017. The altitude z is normalized with the temperature inversion base height z_i. Potential temperature θ and the specific humidity q are normalized with their near-surface values. The cloud top is derived from the irradiance profile; the cloud base is derived from Cloudnet data. The profiles are named after the start time (cf. Fig. 6.4).

clearly above at the upper step at $z \approx 1.2 \cdot z_\mathrm{i}$. For this case, a deficit in q is observed below the SHI, which is plausible because between ascent and descent cloud top had decreased to about $0.95 \cdot z_\mathrm{i}$.

For most profiles, the cloud top coincides with z_i, and the increased humidity is observed above the cloud layer. Only for two profiles (both descents on 5 June), the lower bound of the SHI is already located below the cloud top. Clouds penetrating into the temperature inversion are not observed, although such situations frequently occurred in previous studies (e.g., Sedlar et al., 2012; Pleavin, 2013; Shupe et al., 2013; Sedlar and Shupe, 2014; Brooks et al., 2017). However, two of the descent profiles (6 June 09 h and 7 June 09 h) show situations where the cloud top had decreased between ascent and descent, and the SHI is vertically separated from the cloud top.

6.4.2 Cloud-top height variability versus SHI height

The cloud top variability, here defined as the cloud top height difference between ascent and subsequent descent for each profile, is related to z_i and the lower boundary of the SHI. For all three days, a descending cloud top is observed between the ascent and subsequent descent with a cloud top height difference of $50\,\mathrm{m}$ to $100\,\mathrm{m}$. This cloud top variability is indicated by in-situ irradiance and thermodynamic

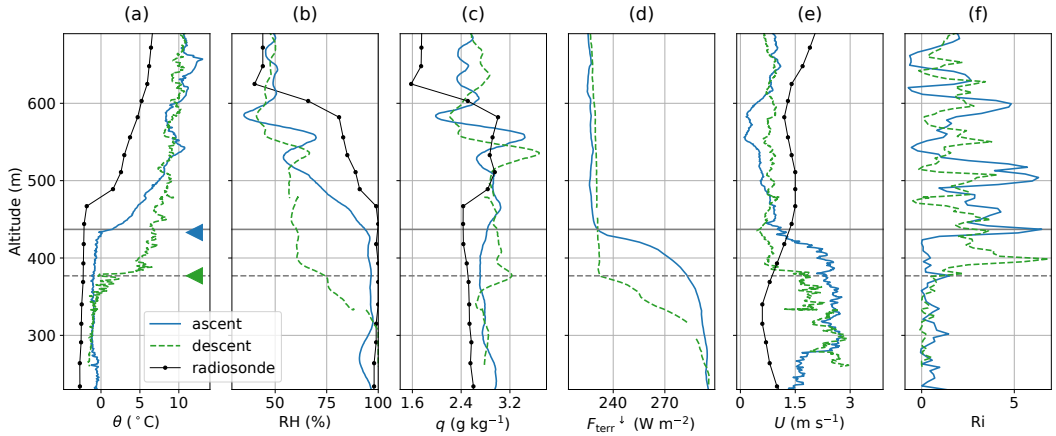

Fig. 6.7.: Boundary layer observations around the cloud top on 5 June 2017, first profile: vertical profiles of **(a)** potential temperature θ, **(b)** RH, **(c)** specific humidity q, **(d)** downward terrestrial irradiance $F^{\downarrow}_{\text{terr}}$, **(e)** horizontal wind velocity U, and **(f)** Richardson number Ri for BELUGA ascent and descent and the radiosonde launched at 11:00 UTC. The triangles indicate where z_{i} is defined. The cloud top is shown as horizontal lines (solid for ascents and dashed for descents).

measurements and also confirmed by radar reflectivity (cf. Fig. 6.4). To illustrate the relation of cloud top height, SHI, and other ABL parameters, Figs. 6.7–6.9 show profiles of mean θ, RH, q, downward terrestrial irradiance $F^{\downarrow}_{\text{terr}}$, horizontal wind velocity U, and gradient Richardson number Ri as measured during ascents and descents on 5, 6, and 7 June, respectively. I analyze only continuous profile data without longer breaks at certain heights for the first profile of each day. The cloud top height is defined by the discontinuity of the $F^{\downarrow}_{\text{terr}}$ profile and marked with horizontal lines, whereas z_{i} is indicated with triangles. The Richardson number is the ratio between thermodynamic stability and wind shear and, therefore, a measure for the ability of turbulence generation ($\text{Ri} \leq 1$) or dissipation ($\text{Ri} \geq 1$).

On 5 June (Fig. 6.7), z_{i} lowers from $430\,\text{m}$ to $380\,\text{m}$ in the course of the BELUGA flight. The temperature difference across the inversion of $\Delta\theta \approx 9\,\text{K}$, which is also the strongest observed during our flights, stays constant during ascent and descent. The RH decreases within the temperature inversion, accompanied by an increase in q above z_{i} of about $0.25\,\text{g}\,\text{kg}^{-1}$ (ascent) and $0.5\,\text{g}\,\text{kg}^{-1}$ (descent). The radiosonde, launched around 2 h prior to the BELUGA flight, shows a higher z_{i} but qualitatively a similar vertical structure of θ, RH, and q. The cloud top agrees well with z_{i} for the ascent and descent. The horizontal wind velocity U is around $2\,\text{m}\,\text{s}^{-1}$ inside the cloud layer and decreases to $1\,\text{m}\,\text{s}^{-1}$ in the free troposphere, resulting in horizontal wind shear. During the ascent, the wind shear zone is clearly located below z_{i} with a sudden increase in Ri to values greater than 1 above z_{i} and cloud top. During the descent, the strongest wind shear is observed around z_{i}, and the resulting increase

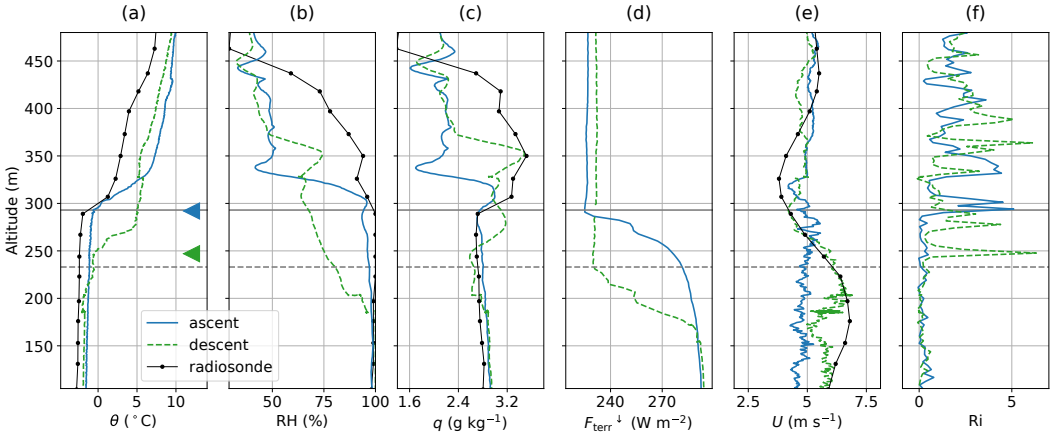

Fig. 6.8.: Same as Fig. 6.7, but for 6 June 2017 (first profile).

in Ri is slightly above z_i. This vertical shift suggests a slightly stronger turbulent coupling between cloud top and the SHI above, as compared to the ascent.

The general ABL structure observed on 6 June (Fig. 6.8) in terms of the profiles of θ, RH and q is quite similar to the 5 June observations, showing a decreasing cloud top height during the balloon operation. Here, z_i decreases from $290\,\mathrm{m}$ during the ascent to about $230\,\mathrm{m}$ during the descent. The radiosonde, launched $1.5\,\mathrm{h}$ after the BELUGA flight, shows a similar z_i to the balloon ascent, indicating that z_i and cloud top recover between BELUGA descent and radiosounding. This is in agreement with the radar observations in Fig. 6.4. The lower bound of the SHI with $\Delta q \approx 0.3\,\mathrm{g\,kg^{-1}}$ on the ascent and $0.7\,\mathrm{g\,kg^{-1}}$ on the descent is coupled to z_i in both cases. On the ascent, z_i coincides with the cloud top. During the descent, the cloud top is almost $20\,\mathrm{m}$ below z_i, which could result from cloud top heterogeneity. However, the temperature gradient is smoother compared to the ascent, which leads to a less clear determination of z_i. The humidity structure above the cloud layer observed by the radiosonde exhibits a distinct SHI with a lower bound coupled to the temperature inversion. Peak values of q are comparable with BELUGA observations made during the descent. The horizontal wind velocity is about $5\,\mathrm{m\,s^{-1}}$ and almost height-constant for the entire ascent but increases by about $2\,\mathrm{m\,s^{-1}}$ inside the cloud layer during the descent. The radiosonde provides a similar picture to the balloon descent. For the ascent, the sharp increase in Ri is connected to z_i, whereas for the descent, this increase in Ri is – similar to the previous day – about $20\,\mathrm{m}$ above cloud top, allowing for some turbulent exchange between the cloud and the SHI above.

On 7 June, a clear SHI develops with a lower boundary at around $580\,\mathrm{m}$, which is similar in the two BELUGA and the radiosonde profiles (Fig. 6.9). For the BELUGA ascent and the radiosonde profile, this boundary agrees well with z_i and cloud

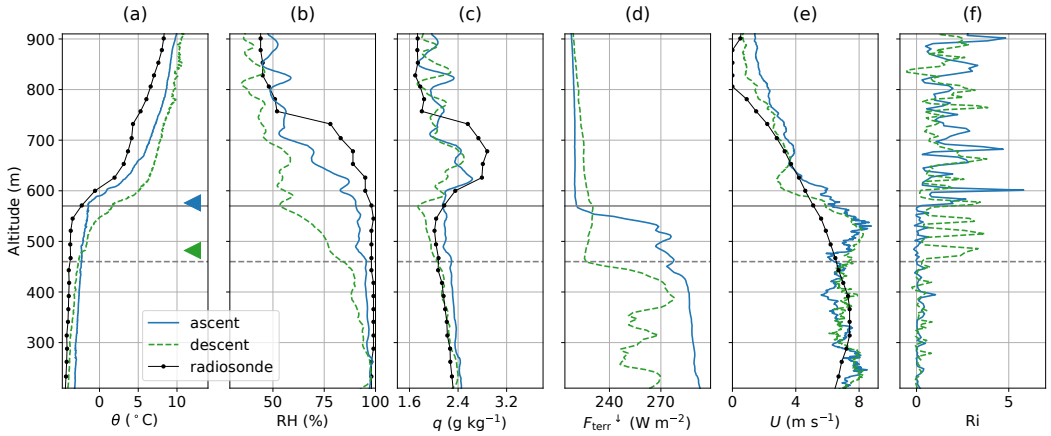

Fig. 6.9.: Same as Fig. 6.7, but for 7 June 2017.

top (for the radiosonde data, cloud top can be roughly estimated from the RH profile). The radiosonde profile and BELUGA ascent are shifted in time by about $70\,\mathrm{min}$ and the remarkable match in z_i should not be over-interpreted. For the BELUGA descent, the thermal stratification changes again (similar to the previous days). The temperature inversion weakens, and z_i is shifted downward by about $110\,\mathrm{m}$ to $480\,\mathrm{m}$, together with the cloud top. Thus, the cloud top and the SHI base are separated by $110\,\mathrm{m}$ on the descent. The terrestrial irradiance inside the cloud layer fluctuates strongly, especially on the descent, which suggests a patchy cloud with cloud holes. The horizontal wind velocity agrees qualitatively for all three profiles. Inside the ABL, a higher wind velocity of around $6\,\mathrm{m\,s^{-1}}$ is observed with the BELUGA observations, showing a local maximum of $8\,\mathrm{m\,s^{-1}}$ slightly below z_i. Above this maximum, U gradually decreases to $2\,\mathrm{m\,s^{-1}}$ in the free troposphere. According to the Richardson number, wind shear limits turbulence above the cloud top for both ascent and descent.

To resume, mean profiles of several cases have been observed where cloud tops coincide with z_i and the SHI base. Although some cloud tops show more or less strong horizontal wind shear, the stabilizing effect of the temperature inversion leads to a sudden increase in Ri just above the cloud layer, which suggests a rather low turbulent exchange with the humidity layers above. However, for one case a special situation provides a new aspect of this phenomenon: z_i and cloud top height had decreased while the humidity layer remained at its vertical position, leading to a humidity gap between cloud top and SHI.

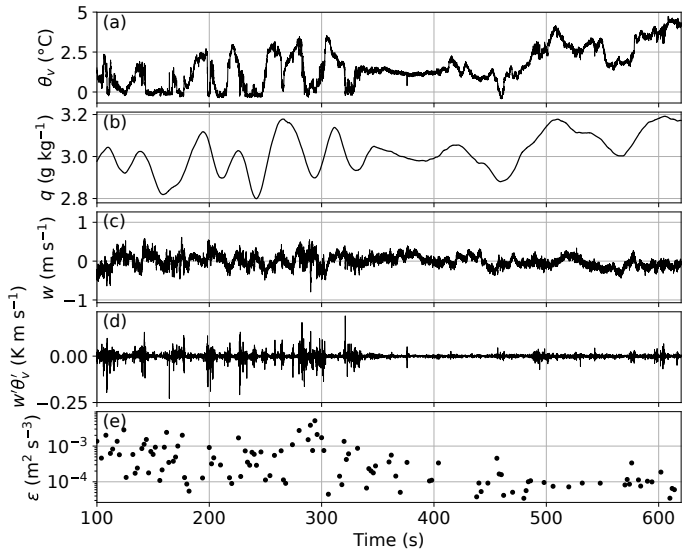

Fig. 6.10.: Constant-altitude time series of **(a)** virtual potential temperature θ_v, **(b)** specific humidity q, **(c)** vertical wind w, **(d)** covariance ${\theta_v}'w'$, and **(e)** dissipation rate ε for 6 June measured at $300\,\mathrm{m}$ altitude around z_i.

6.5 Turbulence at cloud top and around the SHI

6.5.1 Observations at constant altitude in the inversion layer

To get an insight into the transition from cloud top to the humidity layer above, measurements were taken at a constant height in the temperature inversion region. Figure 6.10 shows a $500\,\mathrm{s}$ time series measured on 6 June at a constant altitude around $z_i \approx 300\,\mathrm{m}$ (second last constant altitude segment in Fig. 6.4 for 6 June). The local dissipation rate ε is evaluated in $2\,\mathrm{s}$ segments to illustrate the evolving turbulence intensity.

Within the first third of the record, the virtual potential temperature θ_v (as approximately measured by the ultrasonic anemometer) shows strong variations on a typical timescale of $30\,\mathrm{s}$ to $50\,\mathrm{s}$ with amplitudes up to $3\,\mathrm{K}$. Based on the temperature gradient (Fig. 6.8), the changes in θ_v would correspond to a height variation of $\sim 10\,\mathrm{m}$. More likely, parts of the height-constant measurements ($\Delta z \approx 1\mathrm{m}$) are taken in potentially colder, drier, and more turbulent air masses at the inversion base, interrupted by measurements in potentially warmer, more humid, and less turbulent air masses at higher altitudes well within the T inversion. This variability is also visible in the wind direction (not shown here). Depending on the relative location of z_i to the measurement height, the covariance $w'\theta_v'$ is highly intermittent and no mean flux is derived from these observations.

The center part of the record is characterized by a comparably low variability leading to the conclusion that this part of the observations is performed entirely inside the descending temperature inversion. Finally, observations are performed well above z_i inside the stably stratified T inversion layer, characterized by values of ε one order of magnitude lower than at the inversion base. Here, variations in θ_v and q are again correlated and caused by changes in relative height.

The observations do not allow for drawing quantitative conclusions, such as time and area-averaged turbulent heat fluxes, from this record. However, these measurements vividly illustrate the difficulties in estimating turbulent fluxes based on covariance methods in the vicinity of the temperature inversion, although the measurement height is kept at a remarkably constant height level. Therefore, the methods for estimating turbulent fluxes based on mean vertical gradients and slant profiles are more suitable for this study and are used below.

6.5.2 Vertical profile measurements

Vertical profiles of turbulent energy and dissipation

The vertical distribution of turbulence parameters, such as local dissipation rate ε and the turbulent kinetic energy TKE, provide an insight into the coupling between the cloud layer and the SHI. The local ε values are derived as described in Sect. 4.2.2 from $2\,\mathrm{s}$ sub-records yielding a vertical resolution of about $2\,\mathrm{m}$. Regions without inertial sub-range scaling are excluded. Turbulent kinetic energy is calculated in a moving $50\,\mathrm{s}$ window. The observed TKE noise level is about $0.005\,\mathrm{m^2\,s^{-2}}$ and is usually reached at $z/z_\mathrm{i} \geq 1.1$.

Figure 6.11 shows ε and TKE for each first profile of 5, 6, and 7 June as a function of normalized height (the descent of 5 June is excluded due to data issues). The cloud and humidity layers are shaded for reference. For the presented cases, turbulence is most pronounced in the upper cloud layer and around cloud top with typical values of $\varepsilon \sim 10^{-3}\,\mathrm{m^2\,s^{-3}}$ and TKE $\sim 0.02\,\mathrm{m^2\,s^{-2}}$. For 5 and 6 June, the turbulence intensity is rather constant in the cloud. For 7 June, with increased wind velocity, a maximum of ε is evident just below cloud top.

Figure 6.11 also illustrates how the SHI and cloud layer are either separated or overlap and how they are connected by turbulent motion. At a certain height level, ε decreases to the low-turbulence free-troposphere level. The transition is gradual, indicating turbulent mixing in this region. On 5 June and the ascents of 6 and 7 June, the SHI and the cloud are directly coupled by turbulent mixing. For the

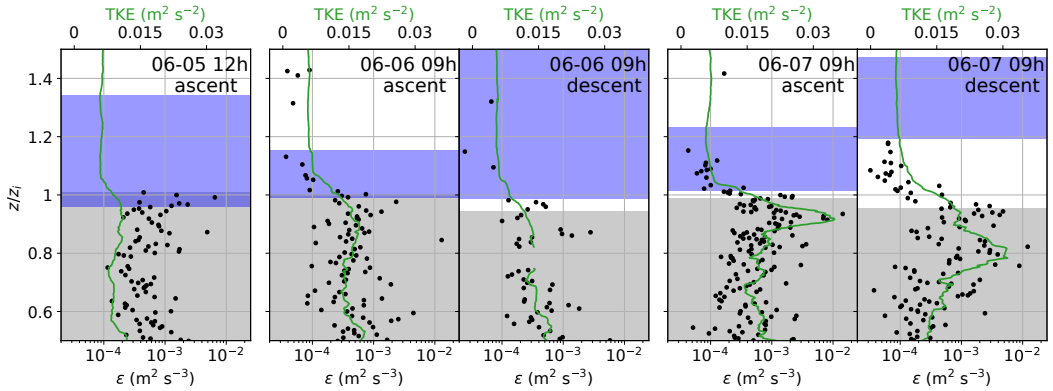

Fig. 6.11.: Vertical profiles of local dissipation rate ε and TKE for the first ascent and descent of 5, 6, and 7 June 2017. The height is normalized by the temperature inversion base z_i. The region of increased specific humidity is marked as blue shading, the cloud layer as grey shading.

descents of 6 and 7 June, most of the mixing takes place at the interface of the cloud top with the humidity gap between cloud and SHI. In this case, inside the SHI the turbulence intensity is reduced almost to the free-troposphere level and the SHI seems to be decoupled from the cloud layer via the humidity gap in between.

One has to speculate about the reason for the development of this humidity gap, which is most pronounced for the descent of 7 June. One explanation could be long-range advection of increased moisture in the free troposphere combined with a temporary collapse of the well-mixed cloud layer leading to a vertical separation of cloud top and SHI. However, this interesting feature leads to new research questions that require further observations and a more detailed LES analysis.

Vertical profiles of turbulent moisture and heat fluxes

The turbulent exchange of moisture can be quantified by the latent heat flux L (Eq. 2.16) whereas the virtual sensible heat flux H is given by Eq. (4.3). The direct calculation of H and L requires sufficient long, stationary, and homogeneous records at a certain height. The observations focus mainly on vertical profiling, and only a limited number of height-constant records around the cloud top and inversion region are available. As shown in Sect. 6.5.1, the conditions around the temperature inversion are highly instationary and, thus, I use the vertical profiles to study the fluxes in this region. I apply two approaches for estimating fluxes from vertical profiles: (i) describing the profile by applying the slant profile method with eddy covariance fluxes and (ii) relating the turbulent flux to mean gradients.

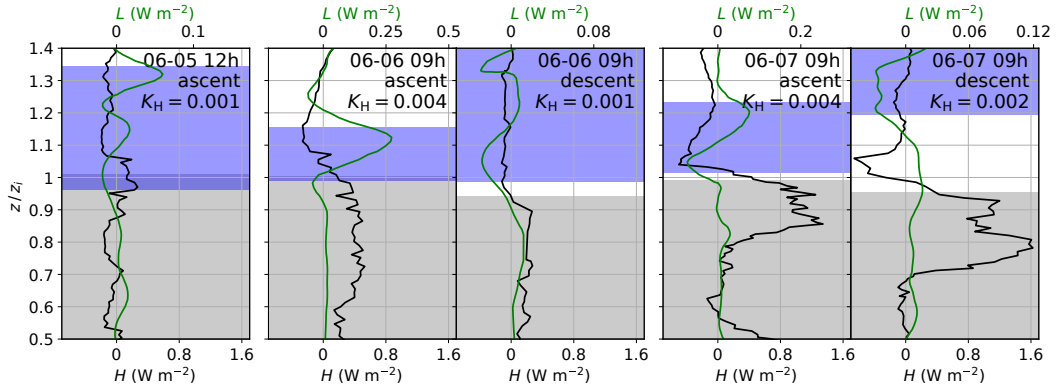

Fig. 6.12.: Same as Fig. 6.11, but for the virtual sensible heat flux H (eddy covariance method) and the latent heat flux L (flux gradient method).

For the observations, the slant profile method provides results for H; L is estimated with the flux gradient method as described in Sect. 4.3.1. Before estimating H from the slant profiles, the turbulent fluctuations are determined using a filter window of $10\,\mathrm{s}$, corresponding to a horizontal length scale of about $10\,\mathrm{m}$ to $70\,\mathrm{m}$ (depending on the horizontal wind velocity) and a vertical length scale of about $10\,\mathrm{m}$. After filtering, the fluxes are averaged over a moving $50\,\mathrm{s}$ window by applying Eq. (4.3).

Figure 6.12 shows five selected cases (cf. Fig. 6.11) with profiles of H based on the slant profile method and L based on the flux gradient method. The upper part of the cloud layer is mainly characterized by an upward-oriented heat flux ($H > 0$), most pronounced for the last two profiles with a local maximum between $0.8 < z/z_\mathrm{i} < 1$. Only for the first ascent of 5 June is the H flux almost height-constant with much lower values compared to the other days. For this day, θ_v exhibits larger variability around and slightly above z_i, which differs from the typical structure of a turbulent flow. This variability mainly causes the positive values of H around z_i, which, therefore, should not be misinterpreted. This is a similar effect to that discussed in Sect. 6.5.1. A negative peak of H around or slightly above z_i is visible for the descent of 6 June and both profiles of 7 June. On 7 June, a secondary, weaker negative peak in H is located at the lower part of the SHI.

Although it is known that in general $K = K(z)$, a constant K_H is estimated for each ascent and descent in the lower region of the SHI, which is the focus area of the study. In that region, negative H fluxes and positive θ_v gradients are observed. Applying Eq. (2.20) leads to mean values of K_H between 0.001 and $0.004\,\mathrm{m^2\,s^{-1}}$ for the five profiles. The $K_\mathrm{H}(= K_\mathrm{Q})$ values for each profile are used for calculating the L profile based on the flux gradient method.

A negative peak in L is observed for all days in the lower SHI region. The downward energy flux at cloud top is common for the entrainment region, where potentially warmer and usually drier air from the free troposphere is mixed downward into the (cloudy) ABL. However, here this downward flux in the lower SHI region means a downward transport of potentially warmer but more humid air into the region below. The situation is different for the descent profile of 7 June, with the vertical humidity gap between cloud top and SHI. Here, the negative peak in L at the lower SHI is accompanied by a positive L at cloud top. This profile does not suggest a significant transport of humidity into the cloud top. Instead, for the special case where the cloud and the SHI are separated, the gap in between receives moisture from both the SHI above and from the cloud layer below.

6.6 Simulated impact of the humidity layer on ABL and cloud structure

The observational data discussed so far provide insight into the turbulent structure of cloudy ABLs that are capped by humidity layers. What remains unclear is how the presence of such humidity layers might have impacted the general ABL and clouds as observed on this day. For this purpose, numerical experiments at cloud- and turbulence-resolving resolutions can be used to good effect, providing virtual data sets for detailed process studies and allowing sensitivity tests for hypothesis testing (Solomon et al., 2014). In this section, idealized LES are discussed that were generated to match the observed vertical structure of the ABL as closely as possible. The LES simulations are Lagrangian, following an air mass from a location $12\,\mathrm{h}$ upstream of the RV *Polarstern*. This allows for proper model spinup and also gives the SHI ample time to impact the turbulence and clouds below. A detailed technical description of the experimental design of the realizations is given by Neggers et al. (2019) and Egerer et al. (2021). Two simulations are discussed, one based on an initial profile without a SHI, the other with a SHI superimposed. The simulations are sampled when the air mass arrives at RV *Polarstern* on 7 June 2017 at 10:48 UTC. The LES output considered includes the mean thermodynamic and cloudy state, as well as the turbulent fluxes of heat H and moisture L, calculated as the covariance between vertical velocity and perturbations in static energy and humidity, respectively.

Figure 6.13 shows vertical profiles of the LES output (with and without an initial SHI) and the BELUGA ascent, where cloud top, z_i, and SHI base coincide. The LES

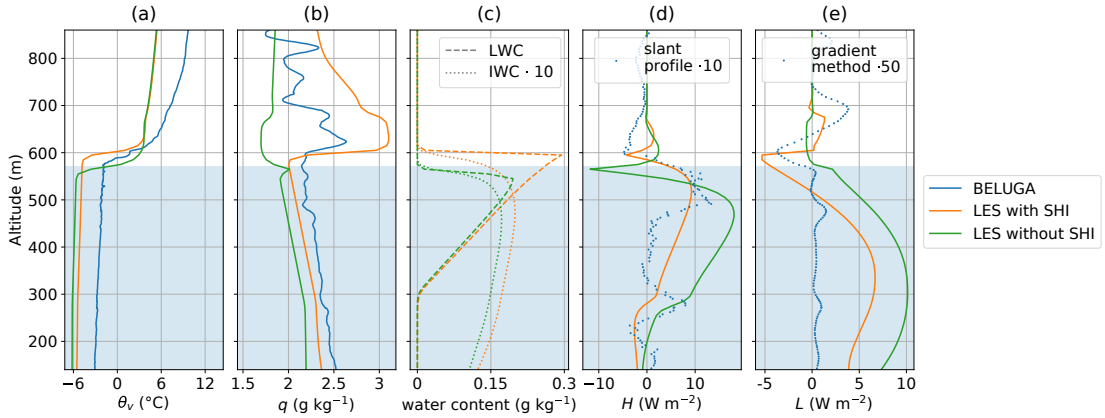

Fig. 6.13.: LES results (with and without an initial SHI) and BELUGA observations for 7 June 2017: vertical profiles of **(a)** virtual potential temperature θ_v, **(b)** specific humidity q, **(c)** LWC and IWC, **(d)** virtual sensible heat flux H, and **(e)** latent heat flux L. The light blue area is the cloud extent for the observations (cloud top is derived from BELUGA irradiance measurements, cloud base from lidar data).

profiles represent averages over the horizontal domain over a $900\,\mathrm{s}$ period. The temperature differences across the inversion as well as the lapse rates above are reasonably well reproduced by the LES (Fig. 6.13a). The experiment including an initial SHI features a temperature inversion base z_i, and similarly a mixed-layer depth that agrees well with the observations. Without the initial humidity layer, z_i is approximately $40\,\mathrm{m}$ lower. The vertical profile of specific humidity shows a similar vertical structure and a distinct increase in q above the cloud layer in both the model and the observations (Fig. 6.13b). The strength of the SHI of $\Delta q = 1.1\,\mathrm{g\,kg^{-1}}$ in the LES is close to the radiosonde SHI strength of $\Delta q = 0.9\,\mathrm{g\,kg^{-1}}$, but larger than the SHI observed with BELUGA of $\Delta q = 0.6\,\mathrm{g\,kg^{-1}}$. In the LES without initial SHI, specific humidity decreases by $\Delta q \approx 0.2\,\mathrm{g\,kg^{-1}}$ within the temperature inversion height range. Within the mixed layer, both experiments slightly underestimate θ_v and q compared to the BELUGA soundings. This is probably explained by the calibration of these experiments to the radiosonde soundings, which show a similar offset compared to BELUGA (cf. Fig. 6.9).

Compared to the balloon measurements, a thinner liquid cloud layer forms in the LES, as indicated in the LWC profiles in Fig. 6.13c. While the observed mixed-phase cloud is around $500\,\mathrm{m}$ thick, the simulations result in a liquid cloud of about $300\,\mathrm{m}$ vertical extent. Note that significant ice water is present below the liquid cloud base in the model, for which lidar readings are sensitive (Bühl et al., 2013). For this reason, the model bias in cloud base height could be artificial. Without a humidity layer, the liquid cloud is thinner, extending only $260\,\mathrm{m}$. The cloud top is simulated at around $600\,\mathrm{m}$ altitude for the scenario with SHI and at $560\,\mathrm{m}$ altitude for the

scenario without SHI, respectively. In the SHI case, the higher cloud top reflects the larger mixed-layer depth compared to the case without SHI.

The LES provides a positive (i.e., upward-directed) virtual sensible heat flux inside the cloud layer (Fig. 6.13d). The negative virtual heat flux at cloud top is seen with and without initial SHI. The LES, with or without an initial SHI, shows a positive moisture flux L between surface and cloud top (Fig. 6.13e). In the presence of an initial SHI, the cloud top region exhibits a negative moisture flux. This negative moisture flux coincides with the negative virtual sensible heat flux and indicates that downward humidity transport occurs between the humidity layer and the underlying mixed layer. Lacking the initial SHI, the total moisture flux is close to zero near the inversion. This means that in this case dry air, rather than humidity, is entrained into the mixed layer from above. The direction of fluxes is in agreement with the flux estimates in Sect. 6.5.2 for 7 June, where a SHI is present above cloud top on the ascent.

More research is necessary to investigate further how the additional entrained moisture of the humidity layer is processed in the cloud (e.g., through phase transition) and how exactly the humidity layer contributes to the cloud evolution (e.g., the role of clouds penetrating into the inversion or thermodynamically decoupled clouds).

6.7 Intermediate summary: SHIs observed during PASCAL

A persistent layer of increased specific humidity above a stratocumulus deck has been observed with BELUGA in the period from 5 to 7 June 2017. Before analyzing these SHIs, an in-depth discussion of the problems associated with humidity measurements in cloudy and cold environments led to the conclusion that the observed SHIs are a natural feature and not a result of measurement artifacts. The observations allow for the first time detailed analyses of the relative position of the SHI, cloud top, and the temperature inversion height z_i and give a first qualitative indication of how these different layers are coupled by turbulent transport.

Two different scenarios are observed: (i) the base of the SHI qualitatively coincides with z_i and the cloud top height and (ii) cloud top height and z_i had decreased with the SHI base remaining at a constant height, leading to a “humidity gap” between cloud top and SHI base. Turbulence, as described by local ε, decreases gradually above z_i suggesting that turbulent energy exchange is possible in that region. Vertical

profiles of latent heat fluxes qualitatively show a downward moisture transport at the base of the SHIs for all profiles. When the SHI coincides with the cloud top as in the first scenario (i), this suggests the cloud is being supplied with moisture from the overlying SHI. For the second scenario (ii), the sign of the latent heat fluxes suggests upward humidity transport from the cloud together with downward humidity transport from the SHI base, both feeding the vertical gap between the SHI base and the cloud top with moisture.

For one case study of the first type of scenario, LES were performed. The simulations support the observational findings by showing a negative moisture flux at the SHI base towards the cloud region below. Further, the LES show that the moisture supply does directly influence the dynamics of the cloudy ABL by increasing z_i and the cloud layer thickness.

For more general conclusions, further observations over a larger measurement period are necessary. Furthermore, I suggest a thorough LES study driven by the observations. These studies are capable of investigating the consequences of the two observed scenarios on ABL dynamics and cloud lifetime and will help to answer the question of how important the SHIs are for the Arctic cloudy ABL.

7 A low-level jet in the late-winter stable Arctic ABL

In this chapter, I analyze a stable ABL with a LLJ observed during PAMARCMiP with respect to the turbulent ABL structure. I study the evolution of the LLJ and the characteristic vertical turbulence structure of ABL conditions with and without a LLJ.

7.1 Arctic low-level jets (LLJs)

LLJs are vertically more or less bounded wind fields with local maximum wind velocities exceeding the geostrophic wind. They can be observed in the stably stratified ABL in heights below $1\,\mathrm{km}$ (Blackadar, 1957; Smedman et al., 1993). There is a lively debate about the origin of LLJs (Vihma et al., 2011; Jakobson et al., 2013; Tuononen et al., 2015; Guest et al., 2018) and details of the formation mechanisms are still not completely understood. Polar regions are preferable locations for the occurrence of LLJs (Tuononen et al., 2015) due to frequently observed (extremely) stably stratified and shallow ABLs, in particular during wintertime.

The stably stratified ABL usually exhibits comparably low turbulence. When neglecting cloud-related effects such as radiative cooling at cloud top, the only significant source for TKE is the surface roughness. However, due to the strong local wind shear below and above the wind maximum, a LLJ can introduce a significant amount of TKE (Smedman et al., 1993) and modulate the vertical distribution of TKE (Banta et al., 2006; Jakobson et al., 2013). These wind shear zones are usually considered a source of TKE production as long as the damping effect of the inversion is not dominating over the TKE production. In addition to TKE production, LLJs play an important role in the advection of momentum, turbulence, as well as aerosol particles and precursor gases (Stensrud, 1996; Algarra et al., 2019).

Here, the ABL evolution in terms of a LLJ is studied, as observed by a set of subsequent vertical wind and temperature profiles measured with BELUGA during PAMARCMiP. The central question of this study is how the LLJ affects the vertical distribution of turbulence and whether increased turbulence is observed at the

surface when the LLJ occurs. This could indicate that properties advected with the LLJ, such as increased aerosol concentration or precursor gases, might be mixed down to the surface.

7.2 Observations and analysis methods

The observational basis for this study is the $24\,\mathrm{h}$ profiling experiment with BELUGA during PAMARCMiP on 29/30 March 2018. The data of the HP and the standard meteorology package are used for the analysis. Continuously running meteorological measurements performed at $9\,\mathrm{m}$ height at VRS and three-dimensional wind data from an ultrasonic anemometer (METEK GmbH, Germany) mounted on a tower at $65\,\mathrm{m}$ height support the analysis of the profiles. The surrounding of VRS is flat and orographic effects on the ABL structure are considered minor.

The study focuses on nine flights between 10:00 UTC on 29 March 2018 and 1:00 UTC on 30 March 2018, which is in the transition between polar night and day. The period was mainly characterized by the persistent occurrence of a LLJ followed by a transition to a more classical stable ABL. Synoptic conditions during this period were influenced by high surface air pressure over central Greenland. All flights took place under cloudless conditions with only occasional thin clouds well above $1000\,\mathrm{m}$.

Figure 7.1 provides an overview of the nine BELUGA profiles up to $600\,\mathrm{m}$ to $1400\,\mathrm{m}$ combined with near-surface measurements. The near-surface conditions are rather variable in terms of temperature T and humidity (T between $-35\,^{\circ}\mathrm{C}$ and $-26\,^{\circ}\mathrm{C}$, specific humidity q between $0.15\,\mathrm{g\,kg^{-1}}$ to $0.3\,\mathrm{g\,kg^{-1}}$) with wind speeds below $2\,\mathrm{m\,s^{-1}}$, becoming more stable towards the end of the period. The specific humidity follows almost exactly the temporal evolution of the temperature. The wind direction is mainly from the west but from 16:00 UTC on changing over south to north and back to westerly winds from 19:00 UTC. Between 13:00 and 14:00 UTC, T and q drop abruptly by $-8\,\mathrm{K}$ and $0.2\,\mathrm{g\,kg^{-1}}$ together with a change in wind direction (from southeast to north) and reach their previous value one hour later.

In this study, I use the balloon-borne vertical profiles to relate the properties of a LLJ to the vertical structure of stability and turbulence. The literature reveals various definitions of a LLJ, mostly based on a local low-altitude wind velocity maximum greater than around $2\,\mathrm{m\,s^{-1}}$ (Blackadar, 1957; Andreas et al., 2000; Tuononen et al., 2015). I adopt this definition and define the following criteria for a LLJ: (i) the wind velocity maximum occurs below $250\,\mathrm{m}$ altitude and (ii) the difference between the maximum wind velocity in the LLJ core u_{LLJ} and the wind minimum u_{min} above

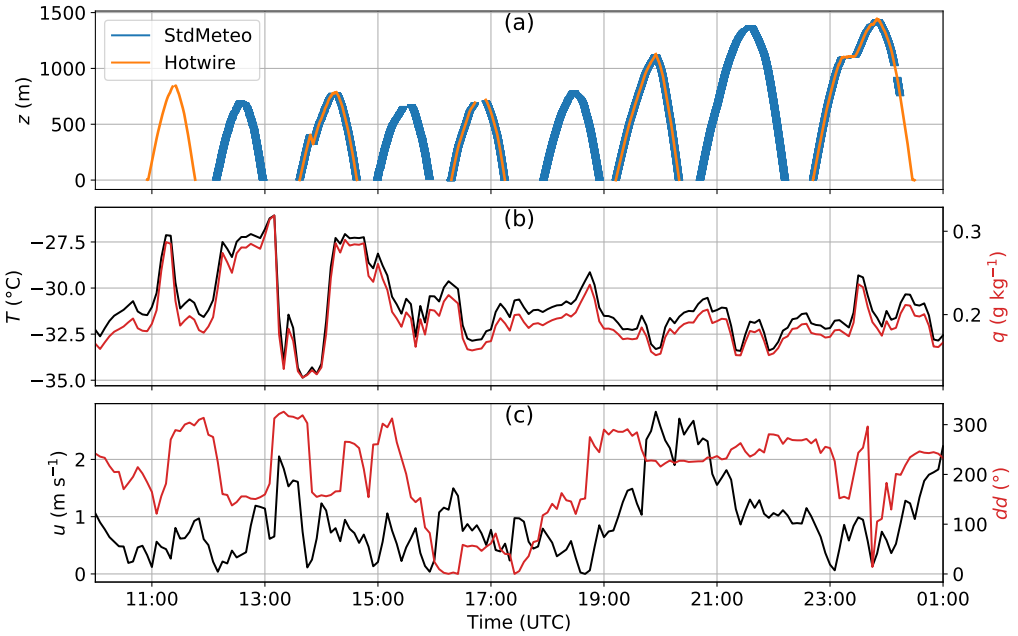

Fig. 7.1.: Time series for 29/30 March 2018 of **(a)** BELUGA flight altitude and **(b)** VRS near-surface measurements of temperature T and specific humidity q as well as **(c)** wind velocity u and wind direction dd.

and below (commonly the near-surface wind velocity) exceeds $2\,\mathrm{m\,s^{-1}}$. The LLJ strength is then defined as $\Delta u = u_{\mathrm{LLJ}} - u_{\mathrm{min}}$ with u_{min} being the higher value either above or below the jet core. The height of the LLJ core z_{LLJ} is typically located at the maximum height of the (strong) temperature inversion z_i.

7.3 Vertical structure of the ABL and LLJ

7.3.1 Evolution of the LLJ and ABL structure

First, the evolution of the mean ABL structure and the LLJ throughout the observation period is analyzed. Figure 7.2 provides an overview of the period based on BELUGA profiles (time-height contour plots), VRS observations in terms of meteorological measurements at $9\,\mathrm{m}$ and the sonic data at $65\,\mathrm{m}$ height. The observation period is divided into three sub-periods: (I) a LLJ period, (II) a transition period, and (III) a standard stable ABL.

In the first period (10:00 to 16:00 UTC), a clear LLJ emerges with a wind velocity maximum of about $10\,\mathrm{m\,s^{-1}}$ in a height of around $100\,\mathrm{m}$ to $150\,\mathrm{m}$, while the wind

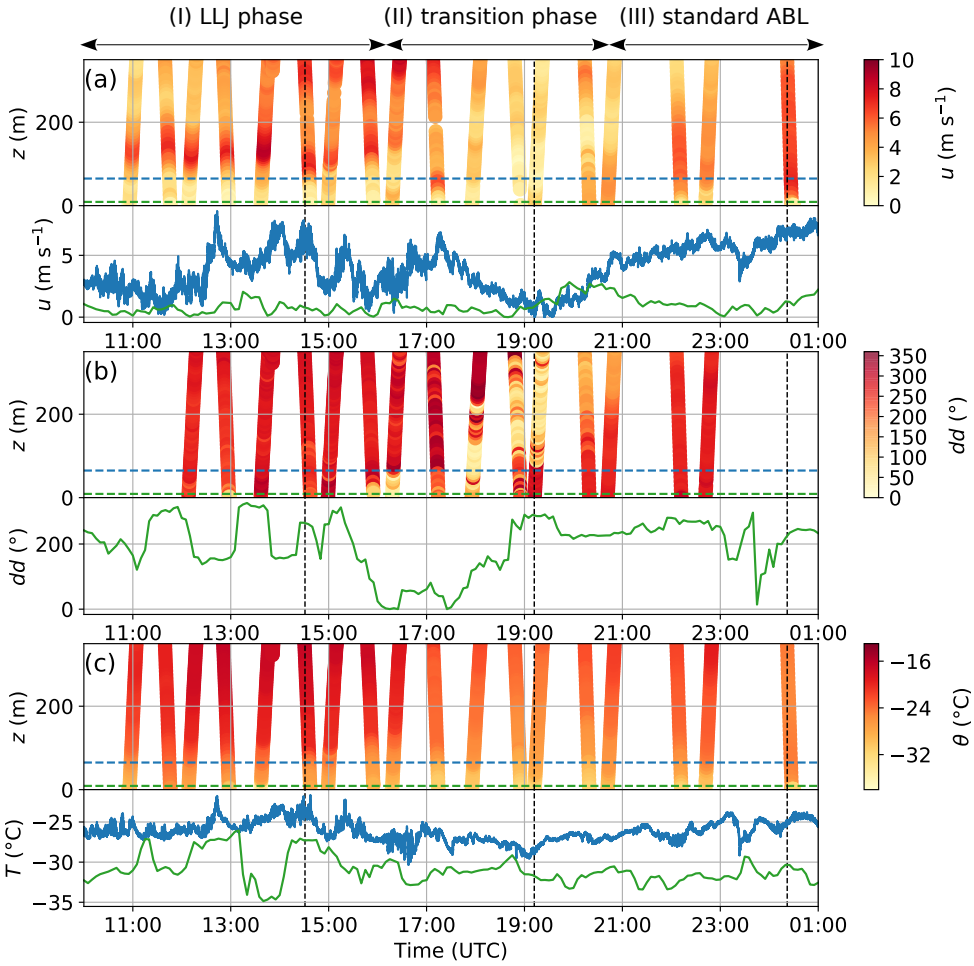

Fig. 7.2.: Time-height contour plots and time series observed at $9\,\mathrm{m}$ (green) and $65\,\mathrm{m}$ (blue) altitude for **(a)** wind velocity u, **(b)** wind direction dd, and **(c)** temperature T/ potential temperature θ. The data are from three different sources: (i) The ascends and descends are from BELUGA, (ii) the data shown at $9\,\mathrm{m}$ altitude are from VRS, and (iii) the data at $65\,\mathrm{m}$ altitude are from the mast. The dashed vertical lines represent the time of the example flights in Fig. 7.3.

velocity in the near-surface layer remains below $2\,\mathrm{m\,s^{-1}}$. The wind direction in the lower $400\,\mathrm{m}$ is west to northwest with the highest variability at surface level. A very stable surface layer develops with near-surface temperatures around $-30\,^{\circ}\mathrm{C}$, which increase by $10\,\mathrm{K}$ to $100\,\mathrm{m}$ height. The sharp surface temperature drop at 13:15 is not obvious at $65\,\mathrm{m}$ altitude and qualitatively correlates with a wind rotation to the north.

Between about 16:30 and 21:00 UTC, the wind velocity becomes more constant with height but generally decreases throughout the profile from about $5\,\mathrm{m\,s^{-1}}$ to less than $2\,\mathrm{m\,s^{-1}}$ with a highly variable wind direction. The LLJ disappears almost completely, and the strong surface temperature gradient now extends only the lowermost tens of meters. At 17:00, however, another smaller LLJ occurs with a maximum at a lower altitude compared to the previous LLJs of the first period. The temperature throughout the entire profile decreases by about $5\,\mathrm{K}$ to $10\,\mathrm{K}$. This period is labeled as a transition between the LLJ period and a standard stable ABL structure.

After 21:00 UTC, the wind velocity increases with a local maximum at around $100\,\mathrm{m}$, but much less pronounced compared to the LLJ structure observed in the first period. The wind direction is almost constant throughout the profile. The temperature profile is similar to the transition phase with a temperature inversion situated at lower altitude.

For a more detailed analysis of the stratification during the three periods, four selected individual profiles of u, θ, and ε are plotted in Fig. 7.3. Local energy dissipation rates ε calculated in $2\,\mathrm{s}$ segments (cf. Sect. 4.2.2) characterize the local turbulence on the vertical profile. The contribution of buoyancy and shear to the turbulence throughout the vertical profile (as expressed by the ε profiles) can be analyzed by the shear and buoyancy terms of the gradient Richardson number (Eq. 2.24). A well-developed LLJ is observed at 14:31 UTC. The wind velocity maximum of $9\,\mathrm{m\,s^{-1}}$ in $100\,\mathrm{m}$ coincides with the top of the strong surface-based temperature inversion. Above this inversion, the ABL is almost adiabatically stratified up to $150\,\mathrm{m}$ – the region with decreasing wind velocity. This region between $100\,\mathrm{m}$ and $150\,\mathrm{m}$ shows the highest local variability of wind velocity, although the wind shear is lower compared to the height range between $40\,\mathrm{m}$ and $100\,\mathrm{m}$. This observation manifests in the local energy dissipation, which is highest – apart from the lowermost surface layer – in the upper part of the LLJ. Here, with almost neutral stratification, the wind shear term in Eq. (2.24) dominates the buoyancy term by one order of magnitude. Below the LLJ core in $40\,\mathrm{m}$ to $100\,\mathrm{m}$, the turbulence generation due to wind shear is reduced (compared to above the LLJ) by the influence of the temperature inversion. A local minimum of ε is located between the

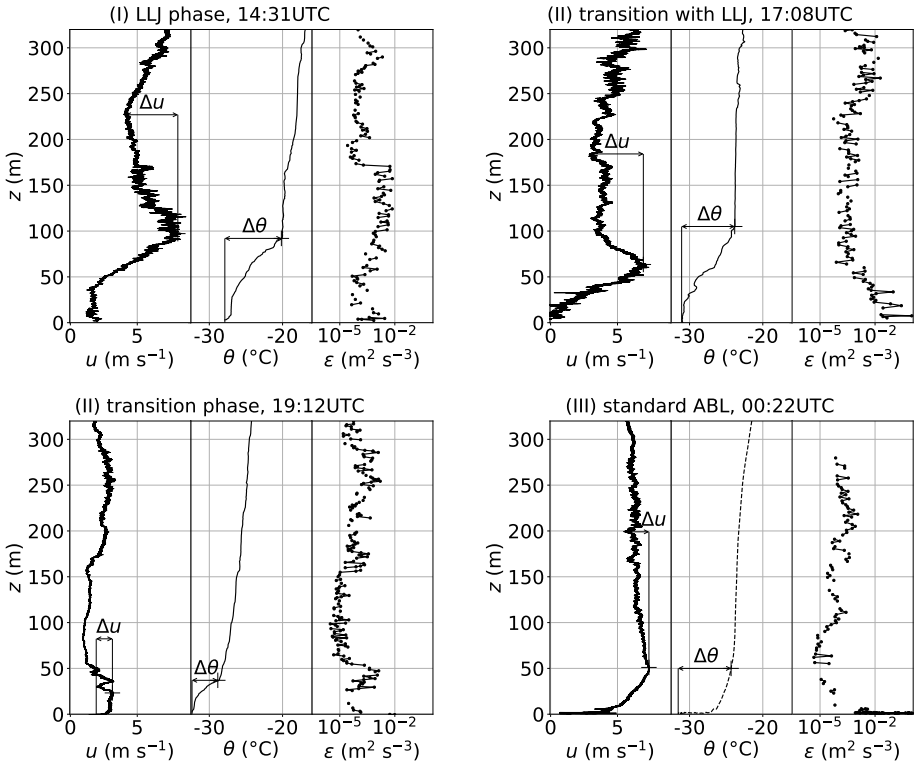

Fig. 7.3.: Example vertical profiles for each phase: wind velocity u with the definition of LLJ strength Δu and LLJ height z_{LLJ}, potential temperature θ with the temperature inversion strength $\Delta\theta$ and inversion height z_{i} and dissipation rate ε. For the transition phase, one profile with and one profile without LLJ is shown.

surface and the base of the LLJ where the damping effect of the strong temperature inversion coincides with a height-constant wind velocity. Above $160\,\mathrm{m}$, θ again slightly increases with height, and ε drops by two orders of magnitude.

The profile observed at 19:12 UTC in the transition phase shows the lowest wind velocity ($\approx 1\,\mathrm{m\,s^{-1}}$) between $50\,\mathrm{m}$ and $160\,\mathrm{m}$. The maximum wind speed is above $3\,\mathrm{m\,s^{-1}}$ in the near-surface layer, coinciding with a temperature inversion up to $40\,\mathrm{m}$. However, just above this inversion, there is a shallow, $20\,\mathrm{m}$ thick layer where the wind shear is strong enough to develop some turbulence indicated by a local maximum of ε up to $10^{-3}\,\mathrm{m^2\,s^{-3}}$. Above and below this maximum, stable stratification in combination with weak wind shear results in reduced turbulence. In the transition phase, one single profile includes a LLJ again (Fig. 7.3, upper right), with a slightly different structure compared to the observations in the first period. Here, the wind velocity increases with height directly above the surface with $u_{\mathrm{LLJ}} = 7\,\mathrm{m\,s^{-1}}$ at $60\,\mathrm{m}$ height. The lowermost $20\,\mathrm{m}$ are neutrally stratified followed by a temperature inversion at $z_i = 100\,\mathrm{m}$, which coincides with the wind minimum above the LLJ. Here, the ε profile is different from the LLJ cases, with maximum turbulence at the

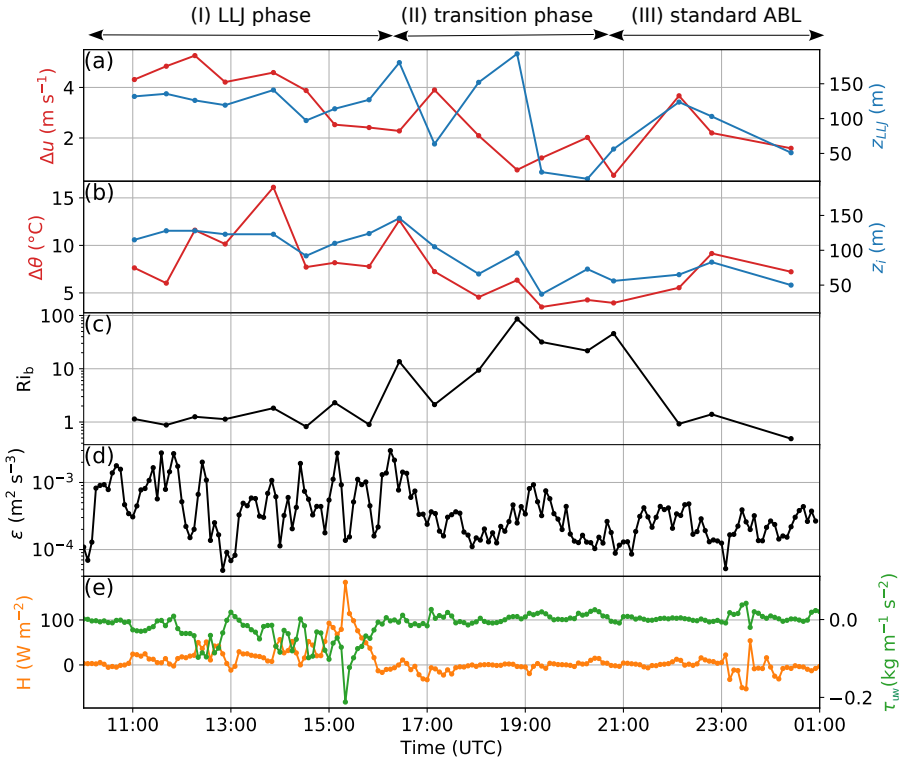

Fig. 7.4.: Temporal development of **(a)** the LLJ parameters strength Δu and height z_{LLJ} (or height of a low-level wind maximum), **(b)** the temperature inversion strength $\Delta\theta$ and height z_{i}, **(c)** bulk Richardson number Ri_b (between surface and z_i), **(d)** dissipation rate ε at $65\,\mathrm{m}$ ($5\,\mathrm{min}$ averages), and **(e)** turbulent fluxes H and τ_{uw} at $65\,\mathrm{m}$.

surface gradually decreasing towards the upper bound of the LLJ, allowing turbulent mixing between the surface and the LLJ core. The upper part of the LLJ is still located inside the temperature inversion, leading to less turbulence in that region than for the LLJ phase. Above the LLJ, the turbulence intensity remains low and slightly increases at higher altitude with the wind velocity increasing again.

In the period with a standard stable ABL structure, the surface layer up to $50\,\mathrm{m}$ shows the largest increase of u and θ, thus resulting in generally low values of ε compared to the previous periods. Above $50\,\mathrm{m}$, the ABL is slightly stably stratified with an almost height-constant wind velocity, weakest turbulence at the top of the surface-based inversion, and some variable turbulence at higher altitude. Throughout the profile, the values for buoyancy and shear increase or decrease to a similar degree, resulting in turbulence predominantly induced by surface roughness.

As a next step, the temporal evolution of LLJ and ABL parameters is examined. Figure 7.4 shows the time series of LLJ and temperature inversion strength and height,

as well as Ri_b derived from the profiles, combined with continuously measured turbulence parameters at $65\,\mathrm{m}$. Ri_b is calculated between z_i and values close to the surface. For the $65\,\mathrm{m}$ mast wind data, ε is estimated analog to the vertical profiles, but averaging over $5\,\mathrm{s}$ segments and using the vertical wind velocity component. The vertical wind velocity of the $65\,\mathrm{m}$ mast sonic anemometer for the flux calculation is tilt-corrected using the double-rotation algorithm described by Wilczak et al. (2001). Turbulent fluxes of virtual sensible heat H and momentum τ_{uw} are averaged over $30\,\mathrm{min}$ after linear detrending. Except for a few cases in the transition phase, the LLJ strength correlates with the temperature inversion strength ($R = 0.52$). The LLJ height correlates even more clearly with the inversion height ($R = 0.64$). Ri_b is increased in the transition period and around $\mathrm{Ri} = 1$ (weak turbulence) for the other two periods. Energy dissipation ε in the LLJ period is one order of magnitude higher than in phase II and III and shows much more variability. The turbulent fluxes of heat H and momentum τ_{uw} show increased values and variability, as well as individual events with high flux magnitude in the LLJ period, compared to low fluxes in the transition and standard ABL phase. The LLJ as observed at 17:04 UTC coincides with a short period of a weak upward oriented momentum flux and downward heat flux.

7.3.2 Normalized vertical profiles

Each of the three periods introduced in Sect. 7.3.1 features a distinct vertical structure of thermodynamic and turbulence parameters. Figure 7.5 shows normalized vertical profiles for each of the three periods. Whereas the height is normalized with z_i, u is normalized with u_{max} (below $300\,\mathrm{m}$), and θ and q are normalized with their values at z_i. The box plots are assigned to height intervals and include mean values for each profile within the respective period. The wind velocity profile shows a characteristic shape for the LLJ period and the standard stable ABL period, with low variability within the profiles. The transition phase exhibits much higher variability, and wind velocity increases with height. The θ and q profiles are similar for all phases with the lowest variability below z_i for the LLJ period. In each period, there is a maximum in ε close to the surface, which indicates surface-driven turbulence for all cases. The vertical turbulence profile is different for each period in relation to the wind profile and will be discussed in more detail.

In the LLJ period, the average ε structure has a characteristic shape with three local maxima: at the surface and just above and below z_i with a local minimum around z_i itself. Another local minimum of ε at $z/z_i \approx 0.3$ might indicate a decoupling of the LLJ from the surface. In the transition period, the average u profile is almost

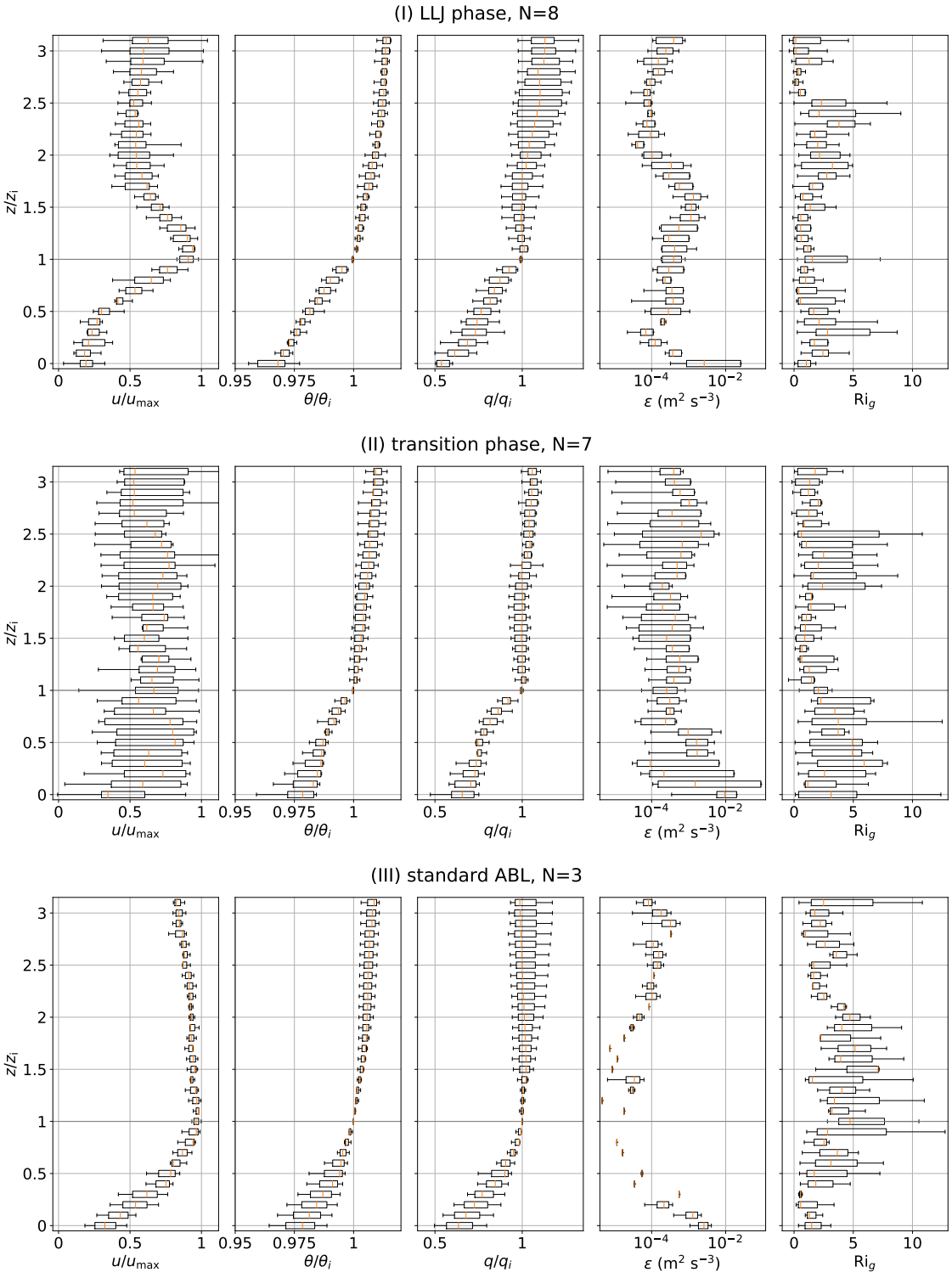

Fig. 7.5.: Normalized vertical profiles of u, θ, ε, Ri_g and q for phase I (with LLJ, top), phase II (transition, center) and phase III (stable ABL without LLJ, bottom). The box plots show variations within the individual N profiles in each phase. The height z is normalized with the temperature inversion base height z_i. The wind velocity is normalized with $u_{\max}$ (u_{LLJ} or maximum u below $300\,\mathrm{m}$). The quantities θ and q are normalized with their value at z_i. The boxes include the lower and upper quartile values of the data, with the orange line at the median.

height-constant but showing high internal variability. The ε profile is highly variable with height without any characteristic structure. The only common features are minimum values around z_i and maximum values close to the surface.

The last period is characterized by a gradual increase of the normalized velocity from the surface up to z_i followed by a slight decrease above. Turbulence shows comparable high values only close to the surface with a clear minimum around z_i where values close to the resolution limit are observed. The low variability within the profiles results partly from only two profiles with turbulence measurements in this phase. For the BELUGA profiles, the dimensionless gradient Richardson number Ri_g (Eq. 2.24) is used to quantify the relative importance of turbulence-generating wind shear and the damping temperature inversion. For estimating Ri_g, u and θ profiles are smoothed with a $10\,\mathrm{s}$ rolling mean before calculating the local gradients. The final Ri_g profile is then smoothed again with a rolling mean with a $10\,\mathrm{s}$ window. The profiles of Ri_g generally match the ε profiles with low Ri_g correlating with high ε but generally showing a high variability.

7.4 Discussion

In Sect. 7.3.2, it was argued that the wind shear associated with a LLJ enhances local turbulence, which manifests in increased local ε values. The contribution of buoyancy and shear to turbulence production can be quantified with the TKE budget equation (cf. Sect. 2.1.1), assuming stationary turbulence and considering only shear and buoyancy to generate TKE. The covariances in the shear and buoyancy terms can be replaced by local gradients via the turbulent transport theory (cf. Sect. 2.1.4). This results in

$$\frac{\partial \mathrm{TKE}}{\partial t} = 0 = \underbrace{-\frac{g}{\overline{\theta}_v} \cdot K_\mathrm{H} \cdot \frac{\partial \overline{\theta}_v}{\partial z}}_{\text{buoyancy}} \underbrace{+ K_\mathrm{m} \cdot \frac{\partial \overline{u}^2}{\partial z^2}}_{\text{shear}} \underbrace{-\varepsilon}_{\text{dissipation}} \tag{7.1}$$

for the TKE budget. The shear and buoyancy terms are calculated from the mean normalized profiles of u and θ in Fig. 7.5 for the LLJ phase (I). The profiles of the turbulent exchange coefficients K_m and K_H result from the K parameterization after Hanna (1968) with the mean profiles of ε and σ_u^2 (Eq. 2.19). The resulting exchange coefficients (Fig. 7.6a) are increased just above the LLJ core at $z/z_i = 1$ and otherwise rather constant. However, the overall magnitude of K depends on the averaging interval for σ_u^2 (here, a filter and averaging window of $20\,\mathrm{s}$ are applied) when deriving K from variances. Figure 7.6b shows the resulting shear and

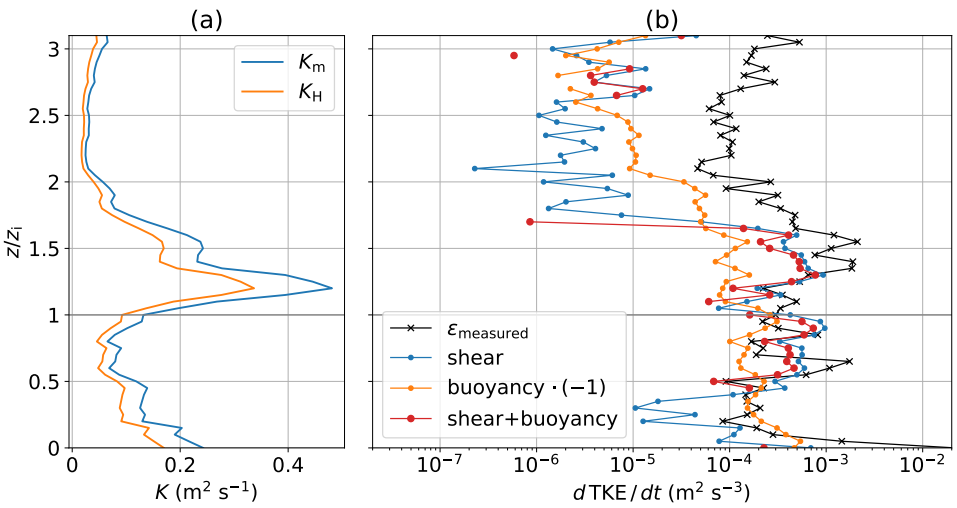

Fig. 7.6.: Mean vertical profiles for all flights of the LLJ phase: **(a)** turbulent exchange coefficients K_m and K_H and **(b)** measured ε and calculated buoyancy and shear terms of the TKE budget equation. Negative values are not depicted.

buoyancy terms in Eq. (7.1). In this case, the buoyancy term represents turbulence consumption due to the stable stratification, while wind shear always produces turbulence. Above and below the jet core (for $0.5 < z/z_i < 1.5$), the shear term is around one order of magnitude greater than the buoyancy term, apart from a buoyancy influence at the jet core at around $z/z_i = 1$. The sum of both terms results in turbulence generation in the height range $0.5 < z/z_i < 1.5$ of similar magnitude compared to the measured TKE dissipation ε. Above and below, buoyancy dominates, resulting in no turbulence generation. This analysis confirms that the LLJ-related wind shear alone can explain a great part of the increased turbulence around the LLJ core. The residual difference between the measured turbulence ε and turbulence production through buoyancy and shear (especially above $z/z_i \approx 1.7$) might result from TKE budget terms not considered here, such as TKE advection by the mean wind.

Another question regarding turbulence is the spatial distribution of the typical length scales involved in this problem. The length scales $\mathcal{L} \propto \sigma^3/\varepsilon$ (Wyngaard, 2010) have to be considered as local length scales since the estimation of σ_u depends on the limited averaging time. The estimation of σ_u and vertical gradients for Ri_g requires high- or low-pass filtered data series and must be averaged over time periods in the order of $10\,\mathrm{s}$ to $60\,\mathrm{s}$. In contrast, local dissipation rates can be estimated for short intervals of a few seconds from original wind velocity data. Figure 7.7 shows the relation between the different local turbulence parameters for all BELUGA profiles on 29 March. Averaging intervals for ε are $5\,\mathrm{s}$, whereas σ_u^3 and Ri_g use filter windows

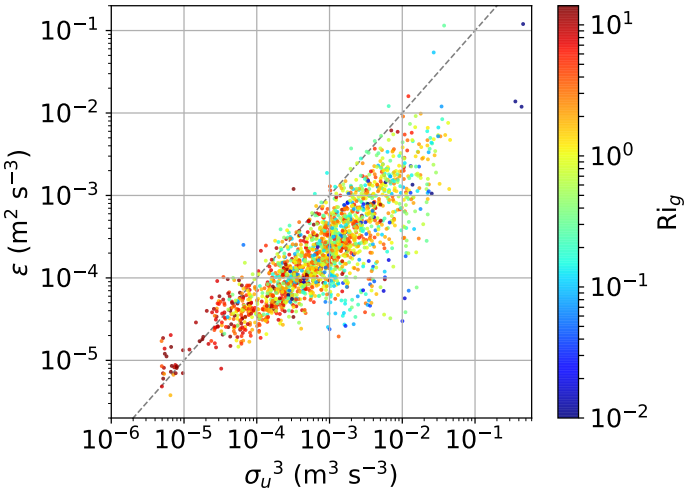

Fig. 7.7.: Relation of turbulence parameters for all BELUGA flights on 29 March 2018 with the HP: Richardson Number Ri$_g$, σ_u^3, and local dissipation rate ε. The dashed line shows the linear 1:1 relation.

and averaging intervals of $30\,\mathrm{s}$. The relation of measured ε and σ_u^3 is almost linear as predicted by theory. Resulting local length scales $\mathcal{L}$ are mainly between $1\,\mathrm{m}$ to $10\,\mathrm{m}$ (this applies for $85\,\%$ of the data points) with slightly larger length scales in strongly turbulent regions. An averaging interval for σ_u^3 of $30\,\mathrm{s}$ includes length scales up to $150\,\mathrm{m}$ at $5\,\mathrm{m\,s^{-1}}$ mean wind. Strong turbulence, as indicated by high σ_u^3 and dissipation rates, is generally found at low Richardson numbers, although there is much scatter of critical Richardson numbers across the range of ε and σ_u^3. The transition between weak and strong turbulence is gradual. Some data points deviate from the linear relationship with disproportionally low ε at low Richardson numbers. To conclude, it was found that σ_u^3 and ε are equally well suited to describe local turbulence and that for the case presented, the averaging and filter intervals of $30\,\mathrm{s}$ for σ_u are sufficient.

7.5 Intermediate summary: turbulence structure around a LLJ

In this chapter, the transition of a stable ABL with a LLJ into a standard stable ABL in the late-winter central Arctic was analyzed with respect to the turbulence structure. The LLJ was observed to persist for several hours, with a characteristic vertical structure of u, θ, and turbulence parameters. The strength and height of the

LLJ are connected with temperature inversion height and strength. The presence of a LLJ enhances turbulent mixing directly above and below the jet core compared to a stable ABL without a LLJ. However, a stably stratified constant-wind region close to the surface might decouple the LLJ from the surface. Only one LLJ case was different, where the increase of wind velocity starts directly from the surface and allows thoroughly turbulent mixing from the LLJ core down to the surface.

To conclude, a LLJ is capable of enhancing turbulent mixing between the ABL and the surface, provided that the LLJ base is located at the surface. In a cloud-free stable Arctic ABL, the LLJ might be the only source of turbulence apart from the surface roughness. This might be important for the vertical mixing of species advected to the Arctic, such as moisture or aerosol particles. For future studies, I suggest a combined analysis of the occurrence of surface-based LLJs and increased near-surface values of moisture, aerosol particles, or other substances to find a potential correlation. Ideally, this would be complemented by vertical profile measurements of all parameters.

8 Summary and Outlook

8.1 Summary

This thesis introduces the new tethered balloon system BELUGA for vertical profile measurements in the cloudy Arctic ABL. The lowermost levels of the Arcitc ABL, including low-level clouds, are challenging to measure with aircraft and ground-based remote sensing; tethered balloons can close this gap. BELUGA is a modular system and is comprised of the tethered balloon itself and multiple instrument packages for high-resolution and collocated in-situ vertical profiling. The flexible combination of the instruments allows the pursuit of specific scientific goals and adaption to different environmental conditions. The instruments are carried by a helium-filled tethered balloon, which has proven to reliably operate in the Arctic environment, including cloudy conditions, wind speeds of up to $15\,\mathrm{m\,s^{-1}}$ and light icing. The typical ceiling of the balloon is about $1.5\,\mathrm{km}$. Currently, three instrument packages are available for the study of turbulent and radiative parameters: (i) an ultrasonic-based turbulence probe, which measures the three-dimensional wind vector for turbulence observations including vertical turbulent energy fluxes, (ii) a small and lightweight hot-wire-based turbulence probe, which allows for energy dissipation rate measurements, and (iii) an upward- and downward-looking broadband radiation package, which allows net irradiance measurements and the determination of radiative heating rates. Standard meteorological parameters are always measured. Collocated measurements of turbulent and radiative fluxes can be combined to link turbulent mixing and cloud top radiative cooling, which is associated with negative heat fluxes. After a technical introduction of the instrument packages, including a description of their performance and limitations, I introduced the methods to calculate and analyze turbulent properties such as turbulent kinetic energy, local dissipation rates, and turbulent energy fluxes in cloudy conditions.

The new BELUGA system was first deployed during the Arctic field campaign PASCAL from an ice floe in June 2017. The capability of the new system is illustrated by three measurement examples, which describe (i) a single cloud layer, (ii) a cloudless situation, and (iii) a multilayer cloud case. The BELUGA vertical profile measurements of thermodynamic, turbulence, and radiation properties during these

three atmospheric situations emphasize the value of collocated measurements with a high vertical resolution. Linkages between cloud-top cooling and turbulence inside clouds are demonstrated. After these examples describing the general performance of BELUGA, two phenomena characteristic for the Arctic ABL are discussed that are closely related to each other.

A detailed case study addresses a layer of increased specific humidity above a persistent stratocumulus deck in three-period during PASCAL. Based on slant profiles, the turbulent virtual sensible heat flux and the latent heat flux are estimated by applying the eddy covariance method and the flux gradient method. The observations allow for a detailed analysis of the relative position of the SHI and cloud top and turbulent transport between these layers. The SHI can either be located directly adjacent to the cloud layer or further above, leading to a "humidity gap" between cloud and SHI. Turbulent coupling connects the cloud layer with the layer above, which is either the SHI or the humidity gap. Moisture is transported downwards from the SHI to the layer below. In other words: when the SHI coincides with the cloud top, this suggests the cloud is being supplied with moisture from the overlying SHI. For the scenario with a humidity gap, both the cloud and the SHI feed this gap with moisture. LES support the observational findings and show that an overlying SHI supplies moisture to the cloud. The conclusions of this study support the hypothesis that SHIs contribute to the longevity of Arctic mixed-phase clouds. The impact of SHIs might be even stronger if clouds penetrate the inversion layer, which has been observed in the Arctic, although not in this study.

In a second campaign, BELUGA was used to study the late-winter stable Arctic ABL in northern Greenland during PAMARCMiP at VRS. For PAMARCMiP, a smaller balloon was used to profile the ABL on a daily basis in a cloud-free two-week period, with an additional extensive measurement effort to capture one diurnal cycle.

A LLJ occurring during the $24\,\mathrm{h}$ profiling experiment is analyzed in a second case study. In the observation period, the stable ABL transitioned from a state with a LLJ into a standard stable ABL. The observed LLJ persisted for several hours, with a characteristic vertical structure of thermodynamic stratification and turbulence. If a LLJ is present, turbulence is enhanced directly above and below the jet maximum. However, the LLJ base must reach down to the surface to the enhance turbulent mixing at the surface and connect the LLJ with the surface. This might allow mixing down advected tracers such as moisture or aerosol particles from higher levels to the surface, although otherwise the strong inversion would hinder effective mixing.

Energy or mass advected into the Arctic is distributed vertically within the ABL by turbulent transport, which is generally limited in the Arctic due to the sta-

ble stratification. Both studies, covering the SHIs and a LLJ, analyze turbulent motions and transport in a particularly stable environment, being either the temperature/humidity inversion or the stable ABL conditions favoring the occurrence of LLJs. I show that in these environments, turbulent mixing is possible. In the SHI case, the mixing is enhanced by the cloud-internal turbulence probably due to radiative cloud-top cooling, and advected moisture is made available for ABL clouds. In the LLJ case, the turbulent motion results from wind shear induced by the LLJ wind profile and might transport advected substances down to the surface. The in-situ, high-resolution measurements of BELUGA are evidence of the turbulent motions driving the ABL development and provide the observational basis for future research studying the physical processes driving the evolution of the turbulent Arctic ABL.

8.2 Outlook

This work demonstrated the potential of the new tethered balloon setup, which is constantly being improved and expanded. Further additional instrument packages for BELUGA are under development, including a comprehensive aerosol and cloud microphysical sensor system. The current data analysis highlighted the importance of high-quality humidity measurements for a precise definition of cloud boundaries and for quantifying humidity transport. An improvement for future measurements would be a fast-response humidity sensor that operates reliably under cold and cloudy conditions. Those observations would allow for quantifying the vertical moisture transport by applying the eddy covariance method.

For general conclusions beyond case studies, more observations over a larger measurement period and covering different locations and seasons are necessary. Not being a part of this thesis, the improved and extended BELUGA system has been deployed on two further Arctic field campaigns:

- In the framework of the Arctic Ocean 2018 (AO2018) campaign, an ice floe camp was established close to the North pole with the Swedish icebreaker *Oden* as the basis in late-summer 2018. BELUGA was launched in a 4-week period with highly variable weather conditions. The turbulence and radiation instruments of BELUGA were combined with an aerosol optical particle counter and additionally with a cloud water sampler on a helikite.
- BELUGA was operated during leg four of the year-long Arctic drift campaign Multidisciplinary drifting Observatory for the Study of Arctic Climate

(MOSAiC) in July 2020. The tethered balloon itself had been revised and can carry an even larger payload of up to 17 kg. In addition to the UP and the BP, an aerosol payload for number concentration and size distribution, a Video Ice Particle Sampler, and an ozone sonde have been deployed. During MOSAiC leg one to three (November 2019 to May 2020), the HP was operated regularly with a balloon of a different research group.

These measurements deliver an extended compilation of statistics of stratification and turbulence profiles under different cloud conditions for the central Arctic. As a perspective, a long-term deployment of BELUGA at an Arctic research station could be realized to compare measurements in different seasons and establish robust statistics.

Scientific questions building on the measurements will be elaborated in upcoming publications, studying the interactions between aerosols, clouds, radiation, and turbulence. The role of moisture advection and humidity inversions for cloud development and lifetime will be further evaluated. Based on the observations during PASCAL, PAMARCMiP, AO2018, MOSAiC and future deployment of BELUGA, the following research questions will be pursued:

- How do SHIs affect ABL dynamics and cloud lifetime and how important are the SHIs for the Arctic cloudy ABL? For this, I suggest a thorough LES study driven by BELUGA observations.
- Does a LLJ favor turbulent transport of advected moisture and aerosol from higher levels down to the surface? Collocated profiling of turbulence, humidity, and aerosols is necessary to answer this question.
- How does the local thermodynamic environment, as compared to remote processes, influence Arctic ABL processes?
- How do cloud microphysical, radiative, and turbulent processes interact during the lifetime of mixed-phase clouds in the central Arctic?

Finally, the observations and the enhanced understanding of atmospheric processes need to be translated into model parameterizations to improve the performance of climate models in terms of ABL process representation. This will contribute to an improved understanding of the mechanisms behind Arctic amplification and will help to better predict future changes in the Arctic climate system.

Appendix

A

Measurement principle of hot-wire and ultrasonic anemometers

This section provides a brief overview of the measurement principles of hot-wire anemometers and ultrasonic anemometers, which are the central instruments for turbulence observations in this study. Hot-wire anemometry is based on the heat conduction of a thin, electrically heated sensing wire, which is cooled by the airflow (Bruun, 1995). The voltage V in the measurement circuit with the sensing wire is related to the flow speed U (King and Barnes, 1914):

$$V^2 = \mathrm{A} + \mathrm{B} \cdot U^{0.5} \tag{A.1}$$

with calibration constants A and B. The main advantage of hot-wire anemometers is the high temporal resolution of $100\,\mathrm{Hz}$ up to $100\,\mathrm{kHz}$, which enables turbulence measurements down to Kolmogorov scales. Further, the sensors and electronics are very compact. On the other hand, the wire sensors are fragile, and the calibration is not straightforward (Jørgensen, 2005), which is why hot-wire wind velocity measurements are frequently calibrated against simultaneous measurements with, e.g., a gust probe. Hot-wire anemometers typically measure the one-dimensional wind vector, but also sensor arrays for two-dimensional or three-dimensional wind measurements exist.

The principle of ultrasonic anemometry is based on the fact that the transit time of an ultrasonic pulse in a measuring section depends on the flow passing through the measuring section (Maruca et al., 2017). Ultrasonic (or sonic) anemometers measure the transit time of a pulse between pairs of transducers (Fig. A.1). The transit time t_x over a length D_x between a pair of transducers depends on the velocity component of the airflow v_x:

$$v_x = \frac{D_x}{2} \cdot \left(\frac{1}{t_{x12}} - \frac{1}{t_{x21}} \right). \tag{A.2}$$

Typical sonic anemometers consist of three pairs of transducers, yielding the three-dimensional wind vector. As the speed of sound also depends on temperature, sonics

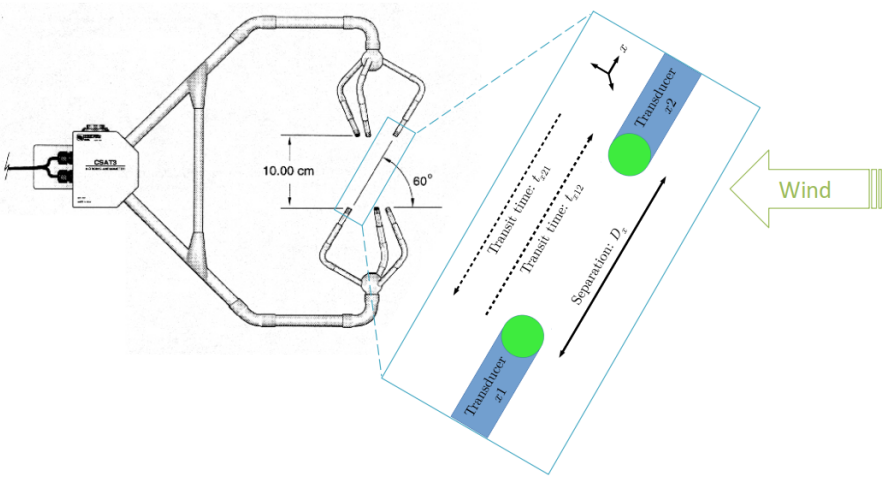

Fig. A.1.: Measurement principle of an ultrasonic anemometer. Modified after Maruca et al. (2017) and https://www.eas.ualberta.ca/jdwilson/EAS327/sonic.jpg.

additionally provide the sonic temperature, which equals approximately the virtual temperature. The temporal resolution of sonic anemometer measurements is lower than for hot-wire anemometers; in return, the system is more robust. Due to the increasing influence of the instrument framework at high airspeeds, sonic anemometers are mainly used at lower speeds, e.g., on masts (Foken, 2003) or slow-moving platforms (Canut et al., 2016). A comprehensive overview of the measuring principles of the above-mentioned instruments is given in Wendisch and Brenguier (2013).

Flight overview tables

B

B.1 PASCAL flight overview

Tab. B.1.: BELUGA flight overview during PASCAL, including cloud conditions and instrumentation: standard meteorology package (SM), ultrasonic anemometer package (UP), hot-wire anemometer package (HP), broadband radiation packages (B1/B2), spectrometer (Sp), aerosol filter sampler (Ae).

Date	No	Start	End	Instruments	Weather
2017-06-05	1	12:35	14:50	B1+B2+SM+UP	Low single layer cloud,
	2	17:24	20:12	B1+B2+SM	snowfall
2017-06-06	1	09:30	11:50	UP+SM+B2+B1	Low single layler cloud, later fog
2017-06-07	1	09:20	12:00	UP+SM+B1+B2	Low single layler cloud,
	2	13:15	14:45	HP+Sp+B1	later broken
2017-06-08	1	09:20	14:00	UP+SM+B1+B2	First clear, occasionally
	2	14:05	15:45	UP+SM+HP+B2	fog patches/ low clouds
2017-06-09	1	08:50	09:30	UP+SM+B1+B2	Overcast, decoupled
	2	09:30	10:20	UP+SM	clouds, could not get above inversion
2017-06-10	1	10:41	11:15	SM+HP+B1	High wind speed, clear
	2	14:15	18:00	Ae+HP	sky, later overcast
	3	14:15	18:00	B1	
2017-06-11	1	13:00	14:12	SM+HP+B2	Low clouds, sometimes
	2	14:28	16:24	SM+HP+B1+B2	broken, strong wind
2017-06-12	1	09:20	12:08	UP+SM+B1+B2	Low level clouds, fog, low wind
2017-06-14	1	09:00	11:30	UP+SM+B1+B2	Multi layer clouds 200m to 4km

B.2 PAMARCMiP flight overview

Tab. B.2.: BELUGA flight overview during PAMARCMiP, including cloud conditions and instrumentation: standard meteorology package (SM), hot-wire package (HP), broadband radiation package (BP), optical particle counter (OPC), Single Channel Tricolor Absorption Photometer (STAP).

Date	No	Start	End	Alt (m)	Instruments	Weather
2018-03-21	1	17:40	18:30	800	SM	
	2	18:40	19:40	300	SM + HP	
2018-03-22	1	13:33	14:00	400	SM	
	2	15:48	16:52	1100	SM + HP	
2018-03-23	1	12:10	15:00	900	SM + HP	
	2	15:15	15:30	100	SM + BP	
2018-03-24	1	13:40	14:50	650	SM + HP	
	2	15:30	16:10	600	SM + BP	
2018-03-25	1	13:10	15:00	700	SM + HP	
	2	15:37	16:13	600	SM	
2018-03-26	1	11:02	12:36	800	BP + SM	
	2	13:10	14:00	500	STAP + SM	
	3	14:00	15:30	1100	SM + HP	
	4	16:40	17:09	500	STAP + SM	
2018-03-27	1	11:15	12:30	1100	STAP + SM	
	2	13:00	15:00	1200	SM + HP	
	3	15:30	16:00	500	STAP + SM	
2018-03-28	1	11:23	12:10	550	SM + HP	
	2	12:40	13:20	550	STAP + SM	
	3	13:30	15:08	550	SM + BP	
2018-03-29	1	10:49	11:50	900	HP	
	2	12:00	13:10	750	BP + SM	
	3	13:25	14:30	800	HP + SM	
	4	14:45	15:30	700	BP + SM	
	5	16:15	17:20	750	HP + SM	
	6	17:45	19:00	800	BP + SM	
	7	19:10	20:30	1150	HP + SM	
	8	20:40	22:20	1400	BP + SM	

	9	22:35	00:30	1450	HP + SM
2018-03-30	1	02:50	03:25	450	BP + SM
	2	03:30	04:00	100	HP + SM
	3	05:45	06:45	900	HP + SM
	4	07:00	07:30	500	BP + SM
	5	08:00	09:00	860	SM + STAP
	6	09:00	10:00	1000	HP + SM
2018-04-01	1	10:30	11:20	850	SM + STAP
	2	11:20	12:15	900	SM + STAP
	3	12:45	13:40	1000	SM + OPC
	4	13:40	15:00	1300	SM + HP
	5	15:15	15:50	800	SM + BP
2018-04-02	1	10:00	11:00	900	SM + STAP
	2	11:00	12:30	1200	SM + HP
2018-04-03	1	17:00	17:50	900	SM + BP
	2	18:10	19:00	1250	SM + HP
	3	19:05	20:10	2x900	SM + STAP
	4	20:15	20:45	600	SM + HP
2018-04-04	1	10:20	12:30	1000	SM + HP
	2	12:45	14:15	2x900	SM + STAP
	3	14:15	15:00	900	SM + BP

List of Acronyms

AA Arctic amplification
ABL atmospheric boundary layer
ACLOUD Arctic CLoud Observations Using airborne measurements during polar Day
ASCOS Arctic Summer Cloud Ocean Study
BELUGA Balloon-bornE moduLar Utility for profilinG the lower Atmosphere
BP broadband radiation package
HP hot-wire anemometer package
IMU inertial measurement unit
IWC ice water content
LES large-eddy simulations
LLJ low-level jet
LWC liquid water content
MOSAiC Multidisciplinary drifting Observatory for the Study of Arctic Climate
PAMARCMiP Polar Airborne Measurements and Arctic Regional Climate Model SImulation Project
PASCAL Physical Feedbacks of Arctic Boundary Layer, Sea Ice, Cloud and Aerosol
PSD power spectral density
SHEBA Surface Heat Budget of the Arctic Ocean
SHI specific humidity inversion
UAV uncrewed aerial vehicle
UP ultrasonic anemometer package
VRS Villum Research Station

List of Symbols

A		Autocorrelation coefficient
α		Kolmogorov constant
C_n		Universal constant for structure function of n^{th} order
$\mathrm{c_p}$	$[\mathrm{J\,kg^{-1}\,K^{-1}}]$	Specific heat capacity
D^n	$[(\mathrm{m\,s^{-1}})^{\mathrm{n}}]$	Structure function of n^{th} order
dd	$[^\circ]$	Wind direction
ΔH	[%]	Systematic error of the turbulent virtual heat flux
E	$[\sigma^2\,\mathrm{m}]$	Spectral energy (wave number space)
e_s	[Pa]	Saturation vapor pressure
ε	$[\mathrm{m^2\,s^{-3}}]$	TKE dissipation rate
η	[mm]	Kolmogorov scale
F_{net}	$[\mathrm{W\,m^{-2}}]$	Net irradiance
f_{c}	[Hz]	Cut-off frequency
f_{Ny}	[Hz]	Nyquist frequency
f_{s}	[Hz]	Sampling frequency
g	$[\mathrm{m\,s^{-2}}]$	Acceleration of gravity
γ	$[\mathrm{K\,km^{-1}}]$	Standard adiabatic lapse rate
H	$[\mathrm{W\,m^{-2}}]$	Turbulent virtual sensible heat flux
H_{S}	$[\mathrm{W\,m^{-2}}]$	Turbulent sensible heat flux
IWC	$[\mathrm{g\,kg^{-1}}]$	Ice water content
K_{x}	$[\mathrm{m^2\,s^{-1}}]$	Turbulent exchange coefficient for parameter x
k	$[\mathrm{m^{-1}}]$	Wave number
L	$[\mathrm{W\,m^{-2}}]$	Turbulent latent heat flux
L_{v}	$[\mathrm{J\,kg^{-1}}]$	Latent heat of evaporation
LWC	$[\mathrm{g\,kg^{-1}}]$	Liquid water content
$\mathcal{L}$	[m]	Integral length scale
N	[Hz]	Brunt-Väisälä frequency
ν	$[\mathrm{m^2\,s^{-1}}]$	Kinematic viscosity
$\vec{\Omega}$	$[^\circ\,\mathrm{s^{-1}}]$	Rotational velocities
Pr_t		Turbulent Prandtl number
p	[hPa]	Pressure
p_0	[hPa]	Near-surface pressure
p_{b}	[hPa]	Barometric pressure
p_{dyn}	[Pa]	Dynamic pressure

ϕ	[°]	Roll angle
ψ	[°]	Yaw angle
q	[$\mathrm{g\,kg^{-1}}$]	Specific humidity
R		Pearson correlation coefficient
R_d	[$\mathrm{J\,kg\,K^{-1}}$]	Specific gas constant of dry air
RH	[%]	Relative humidity
Ri		Richardson number
Ri_b		Bulk Richardson number
Ri_c		Critical Richardson number
Ri_g		Gradient Richardson number
r	[m]	Spatial distance
ρ	[$\mathrm{kg\,m^{-3}}$]	Density
S_x	[$\sigma^2\,\mathrm{Hz^{-1}}$]	Power spectral density for parameter x (frequency space)
$S_\mathrm{x}^{(\mathrm{n})}$	[$\sigma^2\,\mathrm{Hz^{-1}}$]	Spectral noise floor for parameter x
σ_x	[x]	Standard deviation of parameter x
$\sigma_\mathrm{x}^{(\mathrm{n})}$	[x]	Standard deviation due to uncorrelated noise for parameter x
${\sigma_\mathrm{x}}^2$	[x^2]	Variance of parameter x
ς_H	[%]	Random error of the turbulent virtual heat flux
T	[°C]	Temperature
T_0	[°C]	Near-surface temperature
T_m	[s]	Averaging interval
T_v	[°C]	Virtual temperature
TKE	[$\mathrm{m^2\,s^{-2}}$]	Turbulent kinetic energy
t	[s]	Time
t^*	[s]	Time lag
τ	[s]	Time period for averaging local parameters
τ_uw	[$\mathrm{kg\,m^{-1}\,s^{-2}}$]	Momentum flux
τ_x	[s]	Integral time scale for variable x
θ	[°C]	Potential temperature
θ_v	[°C]	Potential virtual temperature
ϑ	[°]	Pitch angle
U	[$\mathrm{m\,s^{-1}}$]	Mean horizontal wind
$\vec{u} = (u, v, w)$	[$\mathrm{m\,s^{-1}}$]	Wind vector with u in mean horizontal wind direction and w in vertical direction
x	[m]	Spatial coordinate
z	[m]	Height
z_b	[m]	Barometric height
z_i	[m]	Inversion height
ζ	[$\mathrm{K\,h^{-1}}$]	Radiative heating rate

List of Figures

List of Tables

Bibliography

Abarbanel, H. D. I., D. D. Holm, J. E. Marsden, and T. Ratiu (1984). "Richardson Number Criterion for the Nonlinear Stability of Three-Dimensional Stratified Flow". In: *Physical Review Letters* 52 (26), pp. 2352–2355. DOI: 10.1103/PhysRevLett.52.2352.

Adachi, K., N. Oshima, S. Ohata, A. Yoshida, N. Moteki, and M. Koike (2021). "Compositions and mixing states of aerosol particles by aircraft observations in the Arctic springtime, 2018". In: *Atmospheric Chemistry and Physics* 21.5, pp. 3607–3626. DOI: 10.5194/acp-21-3607-2021.

Albrecht, B. A., R. S. Penc, and W. H. Schubert (1985). "An Observational Study of Cloud-Topped Mixed Layers". In: *Journal of Atmospheric Sciences* 42.8, pp. 800–822. DOI: 10.1175/1520-0469(1985)042<0800:AOSOCT>2.0.CO;2.

Algarra, I., J. Eiras-Barca, G. Miguez-Macho, R. Nieto, and L. Gimeno (2019). "On the assessment of the moisture transport by the Great Plains low-level jet". In: *Earth System Dynamics* 10.1, pp. 107–119. DOI: 10.5194/esd-10-107-2019.

Aliabadi, A. A., R. Staebler, M. Liu, and A. Herber (2016). "Characterization and Parametrization of Reynolds Stress and Turbulent Heat Flux in the Stably-Stratified Lower Arctic Troposphere Using Aircraft Measurements". In: *Boundary-Layer Meteorology*, pp. 1–28. DOI: 10.1007/s10546-016-0164-7.

Andreas, E. L., K. J. Claffey, and A. P. Makshtas (2000). "Low-level atmospheric jets and inversions over the western Weddell Sea". In: *Boundary-Layer Meteorology* 97 (3), pp. 459–486. DOI: 10.1023/A:1002793831076.

Angevine, W. M., S. K. Avery, and G. L. Kok (1993). "Virtual heat flux measurements from a boundary-layer profiler-RASS compared to aircraft measurements". In: *Journal of Applied Meteorology* 32.12, pp. 1901–1907. DOI: 10.1175/1520-0450(1993)032<1901:VHFMFA>2.0.CO;2.

Ballinger, T. J., J. E. Overland, M. Wang, U. S. Bhatt, E. Hanna, I. Hanssen-Bauer, S. .-J. Kim, R. L. Thoman, and J. E. Walsh (2020). "Surface Air Temperature". In: *Arctic Report Card 2020*. Ed. by R. L. Thoman, J. Richter-Menge, and M. L. Druckenmiller. National Oceanic and Atmospheric Administration (NOAA), pp. 21–27. DOI: 10.25923/gcw8-2z06.

Balsley, B. B., D. A. Lawrence, D. C. Fritts, L. Wang, K. Wan, and J. Werne (2018). "Fine Structure, Instabilities, and Turbulence in the Lower Atmosphere: High-Resolution In Situ Slant-Path Measurements with the DataHawk UAV and Comparisons with Numerical Modeling". In: *Journal of Atmospheric and Oceanic Technology* 35.3, pp. 619–642. DOI: 10.1175/JTECH-D-16-0037.1.

Banta, R. M. (2008). "Stable-boundary-layer regimes from the perspective of the low-level jet". In: *Acta Geophysica* 56 (1), pp. 58–87. DOI: 10.2478/s11600-007-0049-8.

Banta, R. M., Y. L. Pichugina, and W. A. Brewer (2006). "Turbulent Velocity-Variance Profiles in the Stable Boundary Layer Generated by a Nocturnal Low-Level Jet". In: *Journal of the Atmospheric Sciences* 63.11, pp. 2700–2719. DOI: 10.1175/JAS3776.1.

Båserud, L., J. Reuder, M. O. Jonassen, T. A. Bonin, P. B. Chilson, M. A. Jiménez, and P. Durand (2019). "Potential and Limitations in Estimating Sensible-Heat-Flux Profiles from Consecutive Temperature Profiles Using Remotely-Piloted Aircraft Systems". In: *Boundary-Layer Meteorology* 174.1, pp. 145–177. DOI: 10.1007/s10546-019-00478-9.

Batchelor, G. (1953). *The Theory of Homogeneous Turbulence*. Cambridge Science Classics. Cambridge University Press. ISBN: 9780521041171.

Bates, T. S., P. K. Quinn, J. E. Johnsons, A. Corless, F. J. Brechtel, S. E. Stalin, C. Meinig, and J. F. Burkhart (2013). "Measurements of atmospheric aerosol vertical distributions above Svalbard, Norway, using unmanned aerial systems (UAS)". In: *Atmospheric Measurement Techniques* 6, pp. 2115–2120. DOI: doi:10.5194/amt-6-2115-2013.

Becker, R., M. Maturilli, R. Philipona, and K. Behrens (2018). "In-situ sounding of radiation flux profiles through the Arctic lower troposphere". In: *Atmospheric Measurement Techniques Discuss.*, pp. 1–18. DOI: https://doi.org/10.5194/amt-2018-173,inreview.

Bhumralkar, C. M. (1976). "Parameterization of the planetary boundary layer in atmospheric general circulation models". In: *Reviews of Geophysics* 14.2, pp. 215–226. DOI: https://doi.org/10.1029/RG014i002p00215.

Biltoft, C. A. (2001). "Some thoughts on local isotropy and the 4/3 lateral to longitudinal velocity spectrum ratio". In: *Boundary-layer meteorology* 100.3, pp. 393–404.

Blackadar, A. K. (1957). "Boundary Layer Wind Maxima and Their Significance for the Growth of Nocturnal Inversions". In: *Bulletin of the American Meteorological Society* 38.5, pp. 283–290. DOI: 10.1175/1520-0477-38.5.283.

Boeke, R. C., P. C. Taylor, and S. A. Sejas (2021). "On the Nature of the Arctic's Positive Lapse-Rate Feedback". In: *Geophysical Research Letters* 48.1. e2020GL091109 2020GL091109, e2020GL091109. DOI: https://doi.org/10.1029/2020GL091109.

Brooks, I. M., M. Tjernström, P. O. G. Persson, M. D. Shupe, R. A. Atkinson, G. Canut, C. E. Birch, T. Mauritsen, J. Sedlar, and B. J. Brooks (2017). "The turbulent structure of the Arctic summer boundary layer during the Arctic Summer Cloud-Ocean Study". In: *Journal of Geophysical Research: Atmospheres* 122.18, pp. 9685–9704. DOI: 10.1002/2017JD027234.

Brunke, M. A., S. T. Stegall, and X. Zeng (2015). "A climatology of tropospheric humidity inversions in five reanalyses". In: *Atmospheric Research* 153, pp. 165–187. DOI: https://doi.org/10.1016/j.atmosres.2014.08.005.

Bruun, H. H. (1995). *Hot-Wire Anemometry*. Oxford University Press, Oxford, U.K., p. 507.

Bühl, J., A. Ansmann, P. Seifert, H. Baars, and R. Engelmann (2013). "Toward a quantitative characterization of heterogeneous ice formation with lidar/radar: Comparison of CALIPSO/CloudSat with ground-based observations". In: *Geophysical Research Letters* 40.16, pp. 4404–4408. DOI: 10.1002/grl.50792.

Bühl, J., P. Seifert, R. Engelmann, and A. Ansmann (2019). "Impact of vertical air motions on ice formation rate in mixed-phase cloud layers". In: *npj Climate and Atmospheric Science* 2 (1), pp. 1–5. DOI: 10.1038/s41612-019-0092-6.

Calmer, R., G. C. Roberts, J. Preissler, K. J. Sanchez, S. Derrien, and C. O'Dowd (2018). "Vertical wind velocity measurements using a five-hole probe with remotely piloted aircraft to study aerosol–cloud interactions". In: *Atmospheric Measurement Techniques* 11.5, pp. 2583–2599. DOI: 10.5194/amt-11-2583-2018.

Canut, G., F. Couvreux, M. Lothon, D. Legain, B. Piguet, A. Lampert, W. Maurel, and E. Moulin (2016). "Turbulence fluxes and variances measured with a sonic anemometer mounted on a tethered balloon". In: *Atmospheric Measurement Techniques* 9.9, pp. 4375–4386. DOI: 10.5194/amt-9-4375-2016.

Cheng, Y., C. Sayde, Q. Li, J. Basara, J. Selker, E. Tanner, and P. Gentine (2017). "Failure of Taylor's hypothesis in the atmospheric surface layer and its correction for eddy-covariance measurements". In: *Geophysical Research Letters* 44.9, pp. 4287–4295. DOI: https://doi.org/10.1002/2017GL073499.

Cohen, J., X. Zhang, J. Francis, T. Jung, R. Kwok, J. Overland, et al. (2020). "Divergent consensuses on Arctic amplification influence on midlatitude severe winter weather". In: *Nature Climate Change* 10 (1), pp. 20–29. DOI: 10.1038/s41558-019-0662-y.

Coumou, D., G. D. Capua, S. Vavrus, L. Wang, and S. Wang (2018). "The influence of Arctic amplification on mid-latitude summer circulation". In: *Nature Communications* 9 (1), pp. 1–12. DOI: 10.1038/s41467-018-05256-8.

Creamean, J. M., G. de Boer, H. Telg, F. Mei, D. Dexheimer, M. D. Shupe, A. Solomon, and A. McComiskey (2021). "Assessing the vertical structure of Arctic aerosols using balloon-borne measurements". In: *Atmospheric Chemistry and Physics* 21.3, pp. 1737–1757. DOI: 10.5194/acp-21-1737-2021.

Curry, J. A., P. V. Hobbs, M. D. King, D. A. Randall, P. Minnis, G. A. Isaac, et al. (2000). "FIRE Arctic Clouds Experiment". In: *Bulletin of the American Meteorological Society* 81, pp. 5–29. DOI: 10.1175/1520-0477(2000)081<0005:FACE>2.3.CO;2.

Curry, J. A., E. E. Ebert, and G. F. Herman (1988). "Mean and turbulence structure of the summertime Arctic cloudy boundary layer". In: *Quarterly Journal of the Royal Meteorological Society* 114.481, pp. 715–746. DOI: 10.1002/qj.49711448109.

Curry, J. A., J. Maslanik, G. Holland, and J. Pinto (2004). "Applications of Aerosondes in the Arctic". In: *Bulletin of the American Meteorological Society* 85.12, pp. 1855–1862. DOI: 10.1175/BAMS-85-12-1855.

Curry, J. A. (1986). "Interactions among Turbulence, Radiation and Microphysics in Arctic Stratus Clouds". In: *Journal of the Atmospheric Sciences* 43.1, pp. 90–106. DOI: 10.1175/1520-0469(1986)043<0090:IATRAM>2.0.CO;2.

Davidson, P. (2004). *Turbulence: An Introduction for Scientists and Engineers*. OUP Oxford. ISBN: 9780191589850.

de Boer, G., E. W. Eloranta, and M. D. Shupe (2009). "Arctic Mixed-Phase Stratiform Cloud Properties from Multiple Years of Surface-Based Measurements at Two High-Latitude Locations". In: *Journal of the Atmospheric Sciences* 66.9, pp. 2874–2887. DOI: 10.1175/2009JAS3029.1.

de Boer, G., M. Ivey, B. Schmid, D. Lawrence, D. Dexheimer, F. Mei, et al. (2018). "A bird's-eye view: Development of an operational ARM unmanned aerial capability for atmospheric research in Arctic Alaska". In: *Bulletin of the American Meteorological Society* 99.6, pp. 1197–1212. DOI: 10.1175/BAMS-D-17-0156.1.

Deardorff, J. W. (1976). "On the entrainment rate of a stratocumulus-topped mixed layer". In: *Quarterly Journal of the Royal Meteorological Society* 102.433, pp. 563–582. DOI: 10.1002/qj.49710243306.

Devasthale, A., J. Sedlar, and M. Tjernström (2011). "Characteristics of water-vapour inversions observed over the Arctic by Atmospheric Infrared Sounder (AIRS) and radiosondes". In: *Atmospheric Chemistry and Physics* 11.18, pp. 9813–9823. DOI: 10.5194/acp-11-9813-2011.

Dexheimer, D., M. Airey, E. Roesler, C. Longbottom, K. Nicoll, S. Kneifel, F. Mei, R. G. Harrison, G. Marlton, and P. D. Williams (2019). "Evaluation of ARM tethered-balloon system instrumentation for supercooled liquid water and distributed temperature sensing in mixed-phase Arctic clouds". In: *Atmospheric Measurement Techniques* 12.12, pp. 6845–6864. DOI: 10.5194/amt-12-6845-2019.

Dirksen, R. J., M. Sommer, F. J. Immler, D. F. Hurst, R. Kivi, and H. Vömel (2014). "Reference quality upper-air measurements: GRUAN data processing for the Vaisala RS92 radiosonde". In: *Atmospheric Measurement Techniques* 7.12, pp. 4463–4490. DOI: 10.5194/amt-7-4463-2014.

Donth, T., E. Jäkel, A. Ehrlich, B. Heinold, J. Schacht, A. Herber, M. Zanatta, and M. Wendisch (2020). "Combining atmospheric and snow radiative transfer models to assess the solar radiative effects of black carbon in the Arctic". In: *Atmospheric Chemistry and Physics* 20.13, pp. 8139–8156. DOI: 10.5194/acp-20-8139-2020.

Driedonks, A. G. M. and H. Tennekes (1984). "Entrainment effects in the well-mixed atmospheric boundary layer". In: *Boundary-Layer Meteorology* 30.1, pp. 75–105. DOI: 10.1007/BF00121950.

Duda, D. P., G. L. Stephens, S. K. Cox, D. P. Duda, G. L. Stephens, and S. K. Cox (1991). "Microphysical and radiative properties of marine stratocumulus from tethered balloon measurements". In: *Journal of Applied Meteorology* 30.2, pp. 170–186. DOI: 10.1175/1520-0450(1991)030<0170:MARPOM>2.0.CO;2.

Dyer, A. J. (1967). "The turbulent transport of heat and water vapour in an unstable atmosphere". In: *Quarterly Journal of the Royal Meteorological Society* 93.398, pp. 501–508. DOI: 10.1002/qj.49709339809.

Edwards, D., G. Anderson, T. Oakley, and P. Gault (2014). *Met Office Intercomparison of Vaisala RS92 and RS41 Radiosondes*. Technical report. Exeter, UK: UK Met Office. 92 pp.

Egerer, U., A. Ehrlich, M. Gottschalk, H. Griesche, R. A. J. Neggers, H. Siebert, and M. Wendisch (2021). "Case study of a humidity layer above Arctic stratocumulus and potential turbulent coupling with the cloud top". In: *Atmospheric Chemistry and Physics* 21.8, pp. 6347–6364. DOI: 10.5194/acp-21-6347-2021.

Egerer, U., M. Gottschalk, H. Siebert, A. Ehrlich, and M. Wendisch (2019a). "The new BELUGA setup for collocated turbulence and radiation measurements using a tethered balloon: first applications in the cloudy Arctic boundary layer". In: *Atmospheric Measurement Techniques* 12.7, pp. 4019–4038. DOI: 10.5194/amt-12-4019-2019.

Egerer, U., M. Gottschalk, H. Siebert, M. Wendisch, and A. Ehrlich (2019b). *Tethered balloon-borne measurements of turbulence and radiation during the Arctic field campaign PASCAL in June 2017*. Data set. Leibniz-Institut für Troposphärenforschung e.V., Leipzig. DOI: 10.1594/PANGAEA.899803.

Egerer, U. and H. Siebert (2019). *Measurements on the 10m meteorological and turbulence mast during the Arctic field campaign PASCAL in June 2017*. Data set. Leibniz-Institut für Troposphärenforschung e.V., Leipzig. DOI: 10.1594/PANGAEA.899233.

Egerer, U., H. Siebert, J. Voigtländer, and M. Gottschalk (2019c). *Tethered balloon-borne measurements of turbulence and radiation during the Arctic field campaign PAMARCMiP in March/ April 2018*. Data set. Leibniz-Institut für Troposphärenforschung e.V., Leipzig. DOI: 10.1594/PANGAEA.900240.

Ehrlich, A. and M. Wendisch (2015). "Reconstruction of high-resolution time series from slow-response broadband terrestrial irradiance measurements by deconvolution". In: *Atmospheric Measurement Techniques* 8.9, pp. 3671–3684. DOI: 10.5194/amt-8-3671-2015.

Ehrlich, A., M. Wendisch, C. Lüpkes, M. Buschmann, H. Bozem, D. Chechin, et al. (2019). "A comprehensive in situ and remote sensing data set from the Arctic CLoud Observations Using airborne measurements during polar Day (ACLOUD) campaign". In: *Earth System Science Data* 11.4, pp. 1853–1881. DOI: 10.5194/essd-11-1853-2019.

Emeis, S. (2017). "Upper limit for wind shear in stably stratified conditions expressed in terms of a bulk Richardson number". In: *Meteorologische Zeitschrift* 26.4, pp. 421–430. DOI: 10.1127/metz/2017/0828.

Feldl, N., S. Po-Chedley, H. K. Singh, S. Hay, and P. J. Kushner (2020). "Sea ice and atmospheric circulation shape the high-latitude lapse rate feedback". In: *npj Climate and Atmospheric Science* 3 (1), pp. 1–9. DOI: 10.1038/s41612-020-00146-7.

Ferrero, L., C. Ritter, D. Cappelletti, B. Moroni, G. Močnik, M. Mazzola, et al. (2019). "Aerosol optical properties in the Arctic: The role of aerosol chemistry and dust composition in a closure experiment between Lidar and tethered balloon vertical profiles". In: *Science of The Total Environment* 686, pp. 452–467. DOI: https://doi.org/10.1016/j.scitotenv.2019.05.399.

Foken, T. (2003). *Angewandte Meteorologie: Mikrometeorologische Methoden*. Berlin, Heidelberg: Springer Berlin Heidelberg. ISBN: 978-3-662-05743-8. DOI: https://doi.org/10.1007/978-3-662-05743-8.

Frehlich, R., Y. Meillier, M. L. Jensen, and B. Balsley (2003). "Turbulence Measurements with the CIRES Tethered Lifting System during CASES-99: Calibration and Spectral Analysis of Temperature and Velocity". In: *Journal of the Atmospheric Sciences* 60.20, pp. 2487–2495. DOI: 10.1175/1520-0469(2003)060<2487:TMWTCT>2.0.CO;2.

Frisch, U. (1995). *Turbulence: The Legacy of A. N. Kolmogorov*. Cambridge University Press. DOI: 10.1017/CBO9781139170666.

Galperin, B., S. Sukoriansky, and P. S. Anderson (2007). "On the critical Richardson number in stably stratified turbulence". In: *Atmospheric Science Letters* 8.3, pp. 65–69. DOI: https://doi.org/10.1002/asl.153.

Garratt, J. (1994). *The Atmospheric Boundary Layer*. Cambridge Atmospheric and Space Science Series. Cambridge University Press. ISBN: 9780521467452.

Goosse, H., J. E. Kay, K. C. Armour, A. Bodas-Salcedo, H. Chepfer, D. Docquier, et al. (2018). "Quantifying climate feedbacks in polar regions". In: *Nature Communications* 9 (1), p. 1919. DOI: 10.1038/s41467-018-04173-0.

Gottschalk, M., U. Egerer, A. Ehrlich, H. Siebert, and M. Wendisch (2018). "Measured radiative heating rates in single and multi-layer Arctic clouds". 2nd $(AC)^3$ Science Conference, Bremerhaven.

Granskog, M. A., I. Fer, A. Rinke, and H. Steen (2018). "Atmosphere-ice-ocean-ecosystem processes in a thinner Arctic sea ice regime: The Norwegian Young Sea ICE (N-ICE2015) expedition". In: *Journal of Geophysical Research: Oceans* 123.3, pp. 1586–1594. DOI: 10.1002/2017JC013328.

Griesche, H., P. Seifert, A. Ansmann, H. Baars, C. Barrientos Velasco, J. Bühl, R. Engelmann, M. Radenz, Y. Zhenping, and A. Macke (2020a). "Application of the shipborne remote sensing supersite OCEANET for profiling of Arctic aerosols and clouds during *Polarstern* cruise PS106". In: *Atmospheric Measurement Techniques* 13.10, pp. 5335–5358. DOI: 10.5194/amt-13-5335-2020.

Griesche, H., P. Seifert, R. Engelmann, M. Radenz, and J. Bühl (2020b). *Cloudnet target categorization during PS106*. Data set. Leibniz-Institut für Troposphärenforschung e.V., Leipzig. DOI: 10.1594/PANGAEA.919344.

– (2020c). *OCEANET-ATMOSPHERE Cloud radar Mira-35 during PS106*. Data set. Leibniz-Institut für Troposphärenforschung e.V., Leipzig. DOI: 10.1594/PANGAEA.919556.

– (2020d). *OCEANET-ATMOSPHERE low level stratus clouds during PS106*. Data set. Leibniz-Institut für Troposphärenforschung e.V., Leipzig. DOI: 10.1594/PANGAEA.920246.

Gryning, S.-E., E. Batchvarova, R. Floors, C. Münkel, H. Skov, and L. L. Sørensen (2021). "Observed and modelled cloud cover up to 6 km height at Station Nord in the high Arctic". In: *International Journal of Climatology* 41.3, pp. 1584–1598. DOI: https://doi.org/10.1002/joc.6894.

Guest, P., P. O. G. Persson, S. Wang, M. Jordan, Y. Jin, B. Blomquist, and C. Fairall (2018). "Low-Level Baroclinic Jets Over the New Arctic Ocean". In: *Journal of Geophysical Research: Oceans* 123.6, pp. 4074–4091. DOI: https://doi.org/10.1002/2018JC013778.

Hanna, S. R. (1968). "A Method of Estimating Vertical Eddy Transport in the Planetary Boundary Layer Using Characteristics of the Vertical Velocity Spectrum". In: *Journal of Atmospheric Sciences* 25.6, pp. 1026–1033. DOI: 10.1175/1520-0469(1968)025<1026:AMOEVE>2.0.CO;2.

Hartmann, M., K. Adachi, O. Eppers, C. Haas, A. Herber, R. Holzinger, et al. (2020). "Wintertime Airborne Measurements of Ice Nucleating Particles in the High Arctic: A Hint to a Marine, Biogenic Source for Ice Nucleating Particles". In: *Geophysical Research Letters* 47.13. e2020GL087770 10.1029/2020GL087770, e2020GL087770. DOI: https://doi.org/10.1029/2020GL087770.

Herber, A. (2019). *Meteorological observations during POLAR 5 campaign PAMARCMIP 2018*. data set. Alfred Wegener Institute, Helmholtz Centre for Polar and Marine Research, Bremerhaven. DOI: 10.1594/PANGAEA.898788.

Högström, U., J. C. Hunt, and A. S. Smedman (2002). "Theory and measurements for turbulence spectra and variances in the atmospheric neutral surface layer". In: *Boundary-Layer Meteorology* 103 (1), pp. 101–124. DOI: 10.1023/A:1014579828712.

Ingleby, B. (2017). "An assessment of different radiosonde types 2015/2016". In: *ECMWF Technical memorandum* 807, 69 pp.

IPCC (2013). *Climate Change 2013: The Physical Science Basis. Contribution of Working Group I to the Fifth Assessment Report of the Intergovernmental Panel on Climate Change*. Cambridge, United Kingdom and New York, NY, USA: Cambridge University Press, p. 1535. ISBN: ISBN 978-1-107-66182-0. DOI: 10.1017/CBO9781107415324.

– (2019). *IPCC Special Report on the Ocean and Cryosphere in a Changing Climate*. Ed. by H.-O. Pörtner, D. Roberts, V. Masson-Delmotte, P. Zhai, M. Tignor, E. Poloczanska, et al. Cambridge, United Kingdom and New York, NY, USA: Cambridge University Press.

Jakobson, L., T. Vihma, E. Jakobson, T. Palo, A. Männik, and J. Jaagus (2013). "Low-level jet characteristics over the Arctic Ocean in spring and summer". In: *Atmospheric Chemistry and Physics* 13.21, pp. 11089–11099. DOI: 10.5194/acp-13-11089-2013.

Jensen, M. P., D. J. Holdridge, P. Survo, R. Lehtinen, S. Baxter, T. Toto, and K. L. Johnson (2016). "Comparison of Vaisala radiosondes RS41 and RS92 at the ARM Southern Great Plains site". In: *Atmospheric Measurement Techniques* 9, pp. 3115–3129. DOI: doi:10.5194/amt-9-3115-2016.

Jonassen, M. O., P. Tisler, B. Altstädter, A. Scholtz, T. Vihma, A. Lampert, G. König-Langlo, and C. Lüpkes (2015). "Application of remotely piloted aircraft systems in observing the atmospheric boundary layer over Antarctic sea ice in winter". In: *Polar Research* 34.1, p. 25651. DOI: 10.3402/polar.v34.25651.

Kaimal, J. C. and J. J. Finnigan (1994). *Atmospheric Boundary Layer Flows: Their Structure and Measurement*. Oxford University Press. ISBN: 9780195362770.

Kaimal, J. C., J. C. Wyngaard, Y. Izumi, and O. R. Coté (1972). "Spectral characteristics of surface-layer turbulence". In: *Quarterly Journal of the Royal Meteorological Society* 98.417, pp. 563–589. DOI: https://doi.org/10.1002/qj.49709841707.

Katzwinkel, J., H. Siebert, and R. A. Shaw (2012). "Observation of a Self-Limiting, Shear-Induced Turbulent Inversion Layer Above Marine Stratocumulus". In: *Boundary-Layer Meteorology* 145.1, pp. 131–143. DOI: 10.1007/s10546-011-9683-4.

Kay, J. E., T. L'Ecuyer, H. Chepfer, N. Loeb, A. Morrison, and G. Cesana (2016). "Recent Advances in Arctic Cloud and Climate Research". In: *Current Climate Change Reports* 2 (4), pp. 159–169. DOI: 10.1007/s40641-016-0051-9.

Kayser, M., M. Maturilli, R. M. Graham, S. R. Hudson, A. Rinke, L. Cohen, J.-H. Kim, S.-J. Park, W. Moon, and M. A. Granskog (2017). "Vertical thermodynamic structure of the troposphere during the Norwegian young sea ICE expedition (N-ICE2015)". In: *Journal of Geophysical Research: Atmospheres* 122.20, pp. 10, 855–10, 872. DOI: https://doi.org/10.1002/2016JD026089.

King, L. V. and H. T. Barnes (1914). "On the convection of heat from small cylinders in a stream of fluid: Determination of the convection constants of small platinum wires, with applications to hot-wire anemometry". In: *Proceedings of the Royal Society of London. Series A, Containing Papers of a Mathematical and Physical Character* 90.622, pp. 563–570. DOI: 10.1098/rspa.1914.0089.

Knudsen, E. M., B. Heinold, S. Dahlke, H. Bozem, S. Crewell, I. V. Gorodetskaya, et al. (2018). "Meteorological conditions during the ACLOUD/PASCAL field campaign near Svalbard in early summer 2017". In: *Atmospheric Chemistry and Physics* 18.24, pp. 17995–18022. DOI: 10.5194/acp-18-17995-2018.

Knust, R. (2017). "Polar research and supply vessel POLARSTERN operated by the Alfred-Wegener-Institute." In: *Journal of large-scale research facilities* 3. DOI: https://doi.org/10.17815/jlsrf-3-163.

Knuth, S. L. and J. J. Cassano (2014). "Estimating Sensible and Latent Heat Fluxes Using the Integral Method from in situ Aircraft Measurements". In: *Journal of Atmospheric and Oceanic Technology* 31.9, pp. 1964–1981. DOI: 10.1175/JTECH-D-14-00008.1.

Kolmogorov, A. N. (1941a). "Dissipation of Energy in Locally Isotropic Turbulence". In: *Akademiia Nauk SSSR Doklady* 32, p. 16.

– (1941b). "The Local Structure of Turbulence in Incompressible Viscous Fluid for Very Large Reynolds' Numbers". In: *Akademiia Nauk SSSR Doklady* 30, pp. 301–305.

– (1962). "A refinement of previous hypotheses concerning the local structure of turbulence in a viscous incompressible fluid at high Reynolds number". In: *Journal of Fluid Mechanics* 13.1, pp. 82–85. DOI: 10.1017/S0022112062000518.

Kral, S. T., J. Reuder, T. Vihma, I. Suomi, K. F. Haualand, G. H. Urbancic, et al. (2020). "The Innovative Strategies for Observations in the Arctic Atmospheric Boundary Layer Project (ISOBAR) – Unique fine-scale observations under stable and very stable conditions". In: *Bulletin of the American Meteorological Society*, pp. 1–64. DOI: 10.1175/BAMS-D-19-0212.1.

Kroonenberg, A. van den, T. Martin, M. Buschmann, J. Bange, and P. Vörsmann (2008). "Measuring the Wind Vector Using the Autonomous Mini Aerial Vehicle M^2AV". In: *Journal of Atmospheric and Oceanic Technology* 25.11, pp. 1969–1982. DOI: 10.1175/2008JTECHA1114.1.

Kupiszewski, P., C. Leck, M. Tjernström, S. Sjogren, J. Sedlar, M. Graus, M. Müller, B. Brooks, E. Swietlicki, S. Norris, and A. Hansel (2013). "Vertical profiling of aerosol particles and trace gases over the central Arctic Ocean during summer". In: *Atmospheric Chemistry and Physics* 13.24, pp. 12405–12431. DOI: 10.5194/acp-13-12405-2013.

L'Ecuyer, T. S., Y. Hang, A. V. Matus, and Z. Wang (2019). "Reassessing the Effect of Cloud Type on Earth's Energy Balance in the Age of Active Spaceborne Observations. Part I: Top of Atmosphere and Surface". In: *Journal of Climate* 32.19, pp. 6197–6217. DOI: 10.1175/JCLI-D-18-0753.1.

Lampert, A., B. Altstädter, K. Bärfuss, L. Bretschneider, J. Sandgaard, J. Michaelis, et al. (2020). "Unmanned Aerial Systems for Investigating the Polar Atmospheric Boundary Layer—Technical Challenges and Examples of Applications". In: *Atmosphere* 11.4. DOI: 10.3390/atmos11040416.

Lawson, R. P., K. Stamnes, J. Stamnes, P. Zmarzly, J. Koskuliks, C. Roden, Q. Mo, M. Carrithers, and G. L. Bland (2011). "Deployment of a tethered-balloon system for microphysics and radiative measurements in mixed-phase clouds at Ny-Ålesund and South pole". In: *Journal of Atmospheric and Oceanic Technology* 28.5, pp. 656–670. DOI: 10.1175/2010JTECHA1439.1.

Lenschow, D. H., J. Mann, and L. Kristensen (1994). "How long is long enough when measuringfluxes and other turbulence statistics?" In: *Journal of Atmospheric and Oceanic Technology* 11.3, pp. 661–673. DOI: 10.1175/1520-0426(1994)011<0661:HLILEW>2.0.CO;2.

Lenschow, D. H. (1986). "Aircraft measurements in the boundary layer". In: *Probing the atmospheric boundary layer*. Ed. by D. H. Lenschow. Boston: American Meteorological Society. Chap. 5, pp. 39–55.

Lenschow, D. H., X. S. Li, C. J. Zhu, and B. B. Stankov (1988). "The stably stratified boundary layer over the great plains: I. Mean and Turbulence Structure". In: *Boundary-Layer Meteorology* 42, pp. 95–121. DOI: https://doi.org/10.1007/BF00119877.

Li, D. (2019). "Turbulent Prandtl number in the atmospheric boundary layer - where are we now?" In: *Atmospheric Research* 216, pp. 86–105. DOI: doi.org/10.1016/j.atmosres.2018.09.015.

Lovejoy, S., A. F. Tuck, S. J. Hovde, and D. Schertzer (2007). "Is isotropic turbulence relevant in the atmosphere?" In: *Geophysical Research Letters* 34.15. DOI: https://doi.org/10.1029/2007GL029359.

Luce, H., L. Kantha, H. Hashiguchi, and D. Lawrence (2019). "Estimation of Turbulence Parameters in the Lower Troposphere from ShUREX (2016–2017) UAV Data". In: *Atmosphere* 10 (7), p. 384. DOI: 10.3390/atmos10070384.

Macke, A. and H. Flores (2018). "The expeditions PS106/1 and 2 of the research vessel POLARSTERN to the Arctic ocean in 2017". In: *Reports on polar and marine research, Bremerhaven, Alfred Wegener Institute for Polar and Marine Research* 719. DOI: 10.2312/BzPM_0719_2018.

Mahrt, L., J. Sun, W. Blumen, T. Delany, and S. Oncley (1998). "Nocturnal boundary-layer regimes." In: *Boundary-Layer Meteorology* 88, pp. 255–278. DOI: https://doi.org/10.1023/A:1001171313493.

Maruca, B. A., R. Marino, D. Sundkvist, N. H. Godbole, S. Constantin, V. Carbone, and H. Zimmerman (2017). "Overview of and first observations from the TILDAE High-Altitude Balloon Mission". In: *Atmospheric Measurement Techniques* 10.4, pp. 1595–1607. DOI: 10.5194/amt-10-1595-2017.

Maslanik, J. and J. Stroeve (1999a). *Near-Real-Time DMSP SSMIS Daily Polar Gridded Sea Ice Concentrations, Version 1*. nt_20170609_f18_nrt_n. Boulder, Colorado USA. NASA National Snow and Ice Data Center Distributed Active Archive Center. DOI: https://doi.org/10.5067/U8C09DWVX9LM. (Visited on 08/03/2018).

– (1999b). *Near-Real-Time DMSP SSMIS Daily Polar Gridded Sea Ice Concentrations, Version 1*. nt_20180329_f18_nrt_n. Boulder, Colorado USA. NASA National Snow and Ice Data Center Distributed Active Archive Center. DOI: https://doi.org/10.5067/U8C09DWVX9LM. (Visited on 11/11/2020).

Mauritsen, T. (2007). "On the Arctic Boundary Layer: From Turbulence to Climate". PhD thesis. Meteorologiska institutionen (MISU), Stockholm.

Mauritsen, T. and G. Svensson (2007). "Observations of Stably Stratified Shear-Driven Atmospheric Turbulence at Low and High Richardson Numbers". In: *Journal of the Atmospheric Sciences* 64.2, pp. 645–655. DOI: 10.1175/JAS3856.1.

Mayer, S., M. O. Jonassen, A. Sandvik, and J. Reuder (2012). "Profiling the Arctic Stable Boundary Layer in Advent Valley, Svalbard: Measurements and Simulations". In: *Boundary-Layer Meteorology* 143 (3), pp. 507–526. DOI: 10.1007/s10546-012-9709-6.

Mazzola, M., M. Busetto, L. Ferrero, A. P. Viola, and D. Cappelletti (2016). "AGAP: an atmospheric gondola for aerosol profiling". In: *Rendiconti Lincei* 27 (1), pp. 105–113. DOI: 10.1007/s12210-016-0514-x.

McCarthy, J. (1973). "A method for correcting airborne temperature data for sensor response time". In: *Journal of Applied Meteorology* 12.1, pp. 211–214. DOI: 10.1175/1520-0450(1973)012<0211:AMFCAT>2.0.CO;2.

Mellor, G. L. and T. Yamada (1974). "A Hierarchy of Turbulence Closure Models for Planetary Boundary Layers". In: *Journal of Atmospheric Sciences* 31.7, pp. 1791–1806. DOI: 10.1175/1520-0469(1974)031<1791:AHOTCM>2.0.CO;2.

Miles, J. W. (1961). "On the stability of heterogeneous shear flows". In: *Journal of Fluid Mechanics* 10.4, pp. 496–508. DOI: 10.1017/S0022112061000305.

Miloshevich, L. M., A. Paukkunen, H. Vömel, and S. J. Oltmans (2004). "Development and Validation of a Time-Lag Correction for Vaisala Radiosonde Humidity Measurements". In: *Journal of Atmospheric and Oceanic Technology* 21.9, pp. 1305–1327. DOI: 10.1175/1520-0426(2004)021<1305:DAVOAT>2.0.CO;2.

Miloshevich, L. M., H. Vömel, D. N. Whiteman, and T. Leblanc (2009). "Accuracy assessment and correction of Vaisala RS92 radiosonde water vapor measurements". In: *Journal of Geophysical Research: Atmospheres* 114.D11305. DOI: 10.1029/2008JD011565.

Morrison, H., G. de Boer, G. Feingold, J. Harrington, M. D. Shupe, and K. Sulia (2012). "Resilience of persistent Arctic mixed-phase clouds". In: *Nature Geoscience* 5.1 (1), pp. 11–17. DOI: 10.1038/ngeo1332.

Muschinski, A., R. G. Frehlich, and B. B. Balsley (2004). "Small-scale and large-scale intermittency in the nocturnal boundary layer and the residual layer". In: *Journal of Fluid Mechanics* 515, p. 319.

Naakka, T., T. Nygård, and T. Vihma (2018). "Arctic Humidity Inversions: Climatology and Processes". In: *Journal of Climate* 31, pp. 3765–3787. DOI: DOI:10.1175/JCLI-D-17-0497.1.

Neggers, R. A. J., J. Chylik, U. Egerer, H. Griesche, V. Schemann, P. Seifert, H. Siebert, and A. Macke (2019). "Local and Remote Controls on Arctic Mixed-Layer Evolution". In: *Journal of Advances in Modeling Earth Systems* 11.7, pp. 2214–2237. DOI: https://doi.org/10.1029/2019MS001671.

Nicholls, S. and J. Leighton (1986). "An observational study of the structure of stratiform cloud sheets: Part I. Structure". In: *Quarterly Journal of the Royal Meteorological Society* 112.472, pp. 431–460. DOI: 10.1002/qj.49711247209.

Nowak, J. L., H. Siebert, K.-E. Szodry, and S. P. Malinowski (2021). "Coupled and decoupled stratocumulus-topped boundary layers: turbulence properties". In: *Atmospheric Chemistry and Physics Discussions* 2021, pp. 1–41. DOI: 10.5194/acp-2021-214.

Obukhov, A. M. (1962). "Some specific features of atmospheric turbulence". In: *Journal of Geophysical Research (1896-1977)* 67.8, pp. 3011–3014. DOI: https://doi.org/10.1029/JZ067i008p03011.

Osborne, E., J.Richter-Menge, and M. Jeffries (2018). *Arctic Report Card 2018*. National Oceanic and Atmospheric Administration (NOAA). URL: https://www.arctic.noaa.gov/Report-Card.

Overland, J. E. (1985). "Atmospheric boundary layer structure and drag coefficients over sea ice". In: *Journal of Geophysical Research: Oceans* 90.C5, pp. 9029–9049. DOI: https://doi.org/10.1029/JC090iC05p09029.

Perovich, D., W. Meier, M. Tschudi, S. Hendricks, A. A. Petty, D. Divine, et al. (2020). "Sea Ice". In: *Arctic Report Card 2020*. Ed. by R. L. Thoman, J. Richter-Menge, and M. L. Druckenmiller. National Oceanic and Atmospheric Administration (NOAA), pp. 44–53. DOI: 10.25923/n170-9h57.

Persson, P. O. G., C. W. Fairall, E. L. Andreas, P. S. Guest, and D. K. Perovich (2002). "Measurements near the Atmospheric Surface Flux Group tower at SHEBA: Near-surface conditions and surface energy budget". In: *Journal of Geophysical Research: Oceans* 107.C10, SHE 21-1-SHE 21–35. DOI: https://doi.org/10.1029/2000JC000705.

Petty, G. W. (2021). "Sampling error in aircraft flux measurements based on a high-resolution large eddy simulation of the marine boundary layer". In: *Atmospheric Measurement Techniques* 14.3, pp. 1959–1976. DOI: 10.5194/amt-14-1959-2021.

Pithan, F., A. Ackerman, W. M. Angevine, K. Hartung, L. Ickes, M. Kelley, et al. (2016). "Select strengths and biases of models in representing the Arctic winter boundary layer over sea ice: the Larcform 1 single column model intercomparison". In: *Journal of Advances in Modeling Earth Systems* 8.3, pp. 1345–1357. DOI: https://doi.org/10.1002/2016MS000630.

Pithan, F. and T. Mauritsen (2014). "Arctic amplification dominated by temperature feedbacks in contemporary climate models". In: *Nature Geoscience* 7 (3), pp. 181–184. DOI: 10.1038/ngeo2071.

Pithan, F., G. Svensson, R. Caballero, D. Chechin, T. W. Cronin, A. M. L. Ekman, R. Neggers, M. D. Shupe, A. Solomon, M. Tjernström, and M. Wendisch (2018). "Role of air-mass transformations in exchange between the Arctic and mid-latitudes". In: *Nature Geoscience* 11.11, pp. 805–812. DOI: 10.1038/s41561-018-0234-1.

Pleavin, T. D. (2013). "Large eddy simulations of Arctic stratus clouds". PhD thesis. University of Leeds.

Pope, S. B. (2000). *Turbulent Flows*. Cambridge University Press. DOI: 10.1017/CBO9780511840531.

Jørgensen, F. E. (2005). *How to measure turbulence with hot-wire anemometers – a practical guide*. Dantec Dynamics A/S.

Reynolds, O. (1895). "IV. On the dynamical theory of incompressible viscous fluids and the determination of the criterion". In: *Philosophical Transactions of the Royal Society of London. (A.)* 186, pp. 123–164. DOI: 10.1098/rsta.1895.0004.

Richardson, L. F. (1922). *Weather Prediction by Numerical Process*. Cambridge University Press.

Richardson, L. F. and W. N. Shaw (1920). "The supply of energy from and to atmospheric eddies". In: *Proceedings of the Royal Society of London. Series A, Containing Papers of a Mathematical and Physical Character* 97.686, pp. 354–373. DOI: 10.1098/rspa.1920.0039.

Richter-Menge, J., M. L. Druckenmiller, and M. Jeffries (2019). *Arctic Report Card 2019*. National Oceanic and Atmospheric Administration (NOAA). URL: https://www.arctic.noaa.gov/Report-Card.

Schmithüsen, H. (2017). *Upper air soundings during POLARSTERN cruise PS106.1 (ARK-XXXI/1.1), Alfred Wegener Institute, Helmholtz Center for Polar and Marine Research, Bremerhaven, PANGAEA*. Data set. Alfred Wegener Institute, Helmholtz Center for Polar and Marine Research, Bremerhaven. DOI: 10.1594/PANGAEA.882736.

Sedlar, J. and M. D. Shupe (2014). "Characteristic nature of vertical motions observed in Arctic mixed-phase stratocumulus". In: *Atmospheric Chemistry and Physics* 14.7, pp. 3461–3478. DOI: 10.5194/acp-14-3461-2014.

Sedlar, J., M. D. Shupe, M. Tjernström, J. Sedlar, M. D. Shupe, and M. Tjernström (2012). "On the Relationship between Thermodynamic Structure and Cloud Top, and Its Climate Significance in the Arctic". In: *Journal of Climate* 25.7, pp. 2374–2393. DOI: 10.1175/JCLI-D-11-00186.1.

Sedlar, J. and M. Tjernström (2009). "Stratiform Cloud—Inversion Characterization During the Arctic Melt Season". In: *Boundary-Layer Meteorology* 132.3, pp. 455–474. DOI: 10.1007/s10546-009-9407-1.

Sedlar, J., M. Tjernström, T. Mauritsen, M. D. Shupe, I. M. Brooks, P. O. G. Persson, C. E. Birch, C. Leck, A. Sirevaag, and M. Nicolaus (2011). "A transitioning Arctic surface energy budget: The impacts of solar zenith angle, surface albedo and cloud radiative forcing". In: *Climate Dynamics* 37.7-8, pp. 1643–1660. DOI: 10.1007/s00382-010-0937-5.

Sedlar, J., M. Tjernström, A. Rinke, A. Orr, J. Cassano, X. Fettweis, G. Heinemann, M. Seefeldt, A. Solomon, H. Matthes, T. Phillips, and S. Webster (2020). "Confronting Arctic Troposphere, Clouds, and Surface Energy Budget Representations in Regional Climate Models With Observations". In: *Journal of Geophysical Research: Atmospheres* 125.6, e2019JD031783. DOI: https://doi.org/10.1029/2019JD031783.

Shupe, M. D., I. M. Brooks, and G. Canut (2012). "Evaluation of turbulent dissipation rate retrievals from Doppler Cloud Radar". In: *Atmospheric Measurement Techniques* 5.6, pp. 1375–1385. DOI: 10.5194/amt-5-1375-2012.

Shupe, M. D., P. O. G. Persson, I. M. Brooks, M. Tjernström, J. Sedlar, T. Mauritsen, S. Sjogren, and C. Leck (2013). "Cloud and boundary layer interactions over the Arctic sea ice in late summer". In: *Atmospheric Chemistry and Physics* 13.18, pp. 9379–9399. DOI: 10.5194/acp-13-9379-2013.

Shupe, M. D. (2011). "Clouds at Arctic Atmospheric Observatories. Part II: Thermodynamic Phase Characteristics". In: *Journal of Applied Meteorology and Climatology* 50.3, pp. 645–661. DOI: 10.1175/2010JAMC2468.1.

Shupe, M. D. and J. M. Intrieri (2004). "Cloud Radiative Forcing of the Arctic Surface: The Influence of Cloud Properties, Surface Albedo, and Solar Zenith Angle". In: *Journal of Climate* 17.3, pp. 616–628. DOI: 10.1175/1520-0442(2004)017<0616:CRFOTA>2.0.CO;2.

Shupe, M. D., V. P. Walden, E. Eloranta, T. Uttal, J. R. Campbell, S. M. Starkweather, and M. Shiobara (2011). "Clouds at Arctic atmospheric observatories. Part I: occurrence and macrophysical properties". In: *Journal of Applied Meteorology Clim.* 50.3, pp. 626–644. DOI: 10.1175/2010JAMC2467.1.

Siebert, H., K. Lehmann, and R. A. Shaw (2007). "On the use of hot-wire anemometers for turbulence measurements in clouds". In: *Journal of Atmospheric and Oceanic Technology* 24.6, pp. 980–993. DOI: 10.1175/JTECH2018.1.

Siebert, H., K. Lehmann, and M. Wendisch (2006). "Observations of small-scale turbulence and energy dissipation rates in the cloudy boundary layer". In: *Journal of the Atmospheric Sciences* 63.5, pp. 1451–1466. DOI: 10.1175/JAS3687.1.

Siebert, H. and U. Teichmann (2000). "Behaviour of an ultrasonic anemometer under cloudy conditions". In: *Boundary-Layer Meteorology* 94.1, pp. 165–169. DOI: 10.1023/A:1002446723575.

Sikand, M., J. Koskulics, K. Stamnes, B. Hamre, J. J. Stamnes, and R. P. Lawson (2013). "Estimation of mixed-phase cloud optical depth and position using in situ radiation and cloud microphysical measurements obtained from a tethered-balloon platform". In: *Journal of the Atmospheric Sciences* 70.1, pp. 317–329. DOI: 10.1175/JAS-D-12-063.1.

Smedman, A.-S., M. Tjernström, and U. Högrström (1993). "Analsyis of the turbulence structure of a marine Low-Level Jet". In: *Boundary-Layer Meteorology* 66, pp. 195–126.

Smit, H., R. Kivi, H. Vömel, and A. Paukkunen (2013). "Thin Film Capacitive Sensors, In: Kämpfer N. (eds) Monitoring Atmospheric Water Vapour". In: Kämpfer, N. *Monitoring Atmospheric Water Vapour*. Ed. by N. Kämpfer. Vol. 10. ISSI Scientific Report Series. Springer, New York, NY. DOI: 10.1007/978-1-4614-3909-7_2.

Smith, D. M., J. A. Screen, C. Deser, J. Cohen, J. C. Fyfe, J. Garcia-Serrano, et al. (2019). "The Polar Amplification Model Intercomparison Project (PAMIP) contribution to CMIP6: investigating the causes and consequences of polar amplification". In: *Geoscientific Model Development* 12.3, pp. 1139–1164. DOI: 10.5194/gmd-12-1139-2019.

Solomon, A., M. D. Shupe, O. Persson, H. Morrison, T. Yamaguchi, P. M. Caldwell, and G. de Boer (2014). "The Sensitivity of Springtime Arctic Mixed-Phase Stratocumulus Clouds to Surface-Layer and Cloud-Top Inversion-Layer Moisture Sources". In: *Journal of Atmospheric Sciences* 71, pp. 574–595. DOI: DOI:10.1175/JAS-D-13-0179.1.

Solomon, A., M. D. Shupe, P. O. G. Persson, and H. Morrison (2011). "Moisture and dynamical interactions maintaining decoupled Arctic mixed-phase stratocumulus in the presence of a humidity inversion". In: *Atmospheric Chemistry and Physics* 11.19, pp. 10127–10148. DOI: 10.5194/acp-11-10127-2011.

Sotiropoulou, G., J. Sedlar, M. Tjernström, M. D. Shupe, I. M. Brooks, and P. O. G. Persson (2014). "The thermodynamic structure of summer Arctic stratocumulus and the dynamic coupling to the surface". In: *Atmospheric Chemistry and Physics* 14.22, pp. 12573–12592. DOI: 10.5194/acp-14-12573-2014.

Sotiropoulou, G., J. Sedlar, R. Forbes, and M. Tjernström (2016). "Summer Arctic clouds in the ECMWF forecast model: an evaluation of cloud parametrization schemes". In: *Quarterly Journal of the Royal Meteorological Society* 142.694, pp. 387–400. DOI: 10.1002/qj.2658.

Sotiropoulou, G., M. Tjernström, J. Savre, A. M. L. Ekman, K. Hartung, and J. Sedlar (2018). "Large-eddy simulation of a warm-air advection episode in the summer Arctic". In: *Quarterly Journal of the Royal Meteorological Society* 144.717, pp. 2449–2462. DOI: 10.1002/qj.3316.

Stein, A., R. Draxler, G. Rolph, B. Stunder, M. Cohen, and F. Ngan (2015). "NOAA's HYSPLIT atmospheric transport and dispersion modeling system". In: *Bulletin of the American Meteorological Society* 96, pp. 2059–2077. DOI: http://dx.doi.org/10.1175/BAMS-D-14-00110.1.

Stensrud, D. J. (1996). "Importance of Low-Level Jets to Climate: A Review". In: *Journal of Climate* 9, pp. 1698–1711.

Stuecker, M. F., C. M. Bitz, K. C. Armour, C. Proistosescu, S. M. Kang, S. P. Xie, et al. (2018). "Polar amplification dominated by local forcing and feedbacks". In: *Nature Climate Change* 8 (12), pp. 1076–1081. DOI: 10.1038/s41558-018-0339-y.

Stull, R. B. (1988). *An introduction to boundary layer meteorology.* Kluwer Academic Publishers, Dordrecht, The Netherlands.

Sun, B., A. Reale, S. Schroeder, D. J. Seidel, and B. Ballish (2013). "Toward improved corrections for radiation-induced biases in radiosonde temperature observations". In: *Journal of Geophysical Research: Atmospheres* 118.10, pp. 4231–4243. DOI: 10.1002/jgrd.50369.

Tan, I. and T. Storelvmo (2019). “Evidence of Strong Contributions From Mixed-Phase Clouds to Arctic Climate Change”. In: *Geophysical Research Letters* 46 (5), pp. 2894–2902. DOI: 10.1029/2018GL081871.

Taylor, G. I. (1938). “The Spectrum of Turbulence”. In: *Proceedings of the Royal Society A: Mathematical, Physical and Engineering Sciences* 164.919, pp. 476–490. DOI: 10.1098/rspa.1938.0032.

Taylor, G. I. (1935). “Statistical theory of turbulenc”. In: *Proceedings of the Royal Society A: Mathematical, Physical and Engineering Sciences* 151.873, pp. 421–444. DOI: 10.1098/rspa.1935.0158.

Tennekes, H. and J. Lumley (1972). *A First Course in Turbulence*. MIT Press. MIT Press. ISBN: 9780262200196.

Tetzlaff, A., C. Lüpkes, and J. Hartmann (2015). “Aircraft-based observations of atmospheric boundary-layer modification over Arctic leads”. In: *Quarterly Journal of the Royal Meteorological Society* 141.692, pp. 2839–2856. DOI: 10.1002/qj.2568.

Timmermans, M.-L. and Z. Labe (2020). “Sea Surface Temperature”. In: *Arctic Report Card 2020*. Ed. by R. L. Thoman, J. Richter-Menge, and M. L. Druckenmiller. National Oceanic and Atmospheric Administration (NOAA), pp. 53–57. DOI: 10.25923/v0fs-m920.

Tjernström, M., C. Leck, C. E. Birch, J. W. Bottenheim, B. J. Brooks, I. M. Brooks, et al. (2014). “The Arctic Summer Cloud Ocean Study (ASCOS): overview and experimental design”. In: *Atmospheric Chemistry and Physics* 14.6, pp. 2823–2869. DOI: 10.5194/acp-14-2823-2014.

Tjernström, M. (1993). “Turbulence Length Scales in Stably Stratified Free Shear Flow Analyzed from Slant Aircraft Profiles”. In: *Journal of Applied Meteorology and Climatology* 32.5, pp. 948–963. DOI: 10.1175/1520-0450(1993)032<0948:TLSISS>2.0.CO;2.

Tjernström, M., M. D. Shupe, I. M. Brooks, P. Achtert, J. Prytherch, and J. Sedlar (2019). “Arctic Summer Airmass Transformation, Surface Inversions, and the Surface Energy Budget”. In: *Journal of Climate* 32.3, pp. 769–789. DOI: 10.1175/JCLI-D-18-0216.1.

Tjernström, M., G. Svensson, L. Magnusson, I. M. Brooks, J. Prytherch, J. Vüllers, and G. Young (2021). “Central Arctic weather forecasting: Confronting the ECMWF IFS with observations from the Arctic Ocean 2018 expedition”. In: *Quarterly Journal of the Royal Meteorological Society* 147.735, pp. 1278–1299. DOI: https://doi.org/10.1002/qj.3971.

Tuononen, M., V. A. Sinclair, and T. Vihma (2015). “A climatology of low-level jets in the mid-latitudes and polar regions of the Northern Hemisphere”. In: *Atmospheric Science Letters* 16.4, pp. 492–499. DOI: https://doi.org/10.1002/asl.587.

Uttal, T., J. A. Curry, M. G. McPhee, D. K. Perovich, R. E. Moritz, J. A. Maslanik, et al. (2002). “Surface heat budget of the Arctic ocean”. In: *Bulletin of the American Meteorological Society* 83.2, pp. 255–276. DOI: 10.1175/1520-0477(2002)083<0255:SHBOTA>2.3.CO;2.

Van der Hoven, I. (1957). “POWER SPECTRUM OF HORIZONTAL WIND SPEED IN THE FREQUENCY RANGE FROM 0.0007 TO 900 CYCLES PER HOUR”. In: *Journal of Atmospheric Sciences* 14.2, pp. 160–164. DOI: 10.1175/1520-0469(1957)014<0160:PSOHWS>2.0.CO;2.

Vickers, D. and L. Mahrt (2004). “Evaluating Formulations of Stable Boundary Layer Height”. In: *Journal of Applied Meteorology* 43.11, pp. 1736–1749. DOI: 10.1175/JAM2160.1.

Vickers, D. and L. Mahrt (1997). “Quality Control and Flux Sampling Problems for Tower and Aircraft Data”. In: *Journal of Atmospheric and Oceanic Technology* 14.3, pp. 512–526. DOI: 10.1175/1520-0426(1997)014<0512:QCAFSP>2.0.CO;2.

Vihma, T., R. Pirazzini, I. Fer, I. A. Renfrew, J. Sedlar, M. Tjernström, et al. (2014). “Advances in understanding and parameterization of small-scale physical processes in the marine Arctic climate system: a review”. In: *Atmospheric Chemistry and Physics* 14.17, pp. 9403–9450. DOI: 10.5194/acp-14-9403-2014.

Vihma, T., T. Kilpeläinen, M. Manninen, A. Sjöblom, E. Jakobson, T. Palo, J. Jaagus, and M. Maturilli (2011). “Characteristics of Temperature and Humidity Inversions and Low-Level Jets over Svalbard Fjords in Spring”. In: *Advances in Meteorology* 2011, pp. 1–14. DOI: 10.1155/2011/486807.

Villum Research Station (2018). *On-line data: Meteorological parameters*. URL: https://villumresearchstation.dk/data/#c44022 (visited on 01/18/2021).

Vüllers, J., P. Achtert, I. M. Brooks, M. Tjernström, J. Prytherch, A. Burzik, and R. Neely III (2021). “Meteorological and cloud conditions during the Arctic Ocean 2018 expedition”. In: *Atmospheric Chemistry and Physics* 21.1, pp. 289–314. DOI: 10.5194/acp-21-289-2021.

Walden, V. P., S. R. Hudson, L. Cohen, S. Y. Murphy, and M. A. Granskog (2017). “Atmospheric components of the surface energy budget over young sea ice: Results from the N-ICE2015 campaign”. In: *Journal of Geophysical Research: Atmospheres* 122.16, pp. 8427–8446. DOI: 10.1002/2016JD026091.

Wang, J., L. Zhang, A. Dai, F. Immler, M. Sommer, and H. Vömel (2013). “Radiation Dry Bias Correction of Vaisala RS92 Humidity Data and Its Impacts on Historical Radiosonde Data”. In: *Journal of Atmospheric and Oceanic Technology* 30.2, pp. 197–214. DOI: 10.1175/JTECH-D-12-00113.1.

Wendisch, M. and J.-L. Brenguier, eds. (2013). *Airborne measurements for environmental research*. Weinheim, Germany: Wiley-VCH Verlag GmbH & Co. KGaA. ISBN: 9783527653218. DOI: 10.1002/9783527653218.

Wendisch, M., A. Macke, A. Ehrlich, C. Lüpkes, M. Mech, D. Chechin, et al. (2019). “The Arctic Cloud Puzzle: Using ACLOUD/PASCAL Multiplatform Observations to Unravel the Role of Clouds and Aerosol Particles in Arctic Amplification”. In: *Bulletin of the American Meteorological Society* 100.5, pp. 841–871. DOI: 10.1175/BAMS-D-18-0072.1.

Wendisch, M. and P. Yang (2012). *Theory of atmospheric radiative transfer - A comprehensive introduction*. Weinheim; Germany: Wiley-VCH Verlag GmbH & Co.KGaA, p. 321. ISBN: 9783527408368.

Wilczak, J. M., S. P. Oncley, and S. A. Stage (2001). “Sonic anemometer tilt correction algorithms”. In: *Boundary-Layer Meteorology* 99.1, pp. 127–150. DOI: 10.1023/A:1018966204465.

Wild, M., M. Z. Hakuba, D. Folini, P. Dörig-Ott, C. Schär, S. Kato, and C. N. Long (2019). "The cloud-free global energy balance and inferred cloud radiative effects: an assessment based on direct observations and climate models". In: *Climate Dynamics* 52 (7-8), pp. 4787–4812. DOI: 10.1007/s00382-018-4413-y.

Wood, R. (2012). "Stratocumulus Clouds". In: *Monthly Weather Review* 140.8, pp. 2373–2423. DOI: 10.1175/MWR-D-11-00121.1.

Wyngaard, J. C. (2010). *Turbulence in the atmosphere*. Cambridge University Press. DOI: 10.1017/CBO9780511840524.

Yeung, P. K. and Y. Zhou (1997). "Universality of the Kolmogorov constant in numerical simulations of turbulence". In: *Physical Review E* 56 (2), pp. 1746–1752. DOI: 10.1103/PhysRevE.56.1746.

Zhang, Y., Z. Gao, D. Li, Y. Li, N. Zhang, X. Zhao, and J. Chen (2014). "On the computation of planetary boundary-layer height using the bulk Richardson number method". In: *Geoscientific Model Development* 7.6, pp. 2599–2611. DOI: 10.5194/gmd-7-2599-2014.

Zusammenfassung der Dissertation

A new set of tethered balloon-borne instrument payloads for collocated turbulence and radiation measurements in the cloudy Arctic boundary layer – first applications

der Fakultät für Physik und Geowissenschaften der Universität Leipzig

eingereicht von

Dipl.-Ing. Ulrike Egerer

angefertigt am

Leibniz-Institut für Troposphärenforschung

Juni 2021

The effects of global warming are most pronounced in the Arctic, which is referred to as Arctic amplification. The atmospheric and surface processes involved in Arctic amplification and their interactions are not fully understood, causing major uncertainties in model projections of the future Arctic climate (Smith et al., 2019). The Arctic atmospheric boundary layer (ABL), where most atmospheric processes are effective, connects the free troposphere with the underlying sea ice by modulating the surface energy budget (Sedlar et al., 2020). Turbulent processes in the ABL, in particular turbulent energy fluxes, play a major role because they distribute energy vertically within the ABL. As another factor, clouds modify the outgoing and incoming radiation and affect the vertical energy transport and turbulent mixing (Brooks et al., 2017). This feeds back on the clouds, making the cloud-radiation-turbulence interactions an intertwined and complicated system (Wendisch et al., 2019).

In the central Arctic ABL, only few in-situ vertical profile observations of turbulence parameters exist. Much of the current knowledge is based on aircraft observations (e.g., Tetzlaff et al., 2015) and ground-based remote sensing (e.g., Sedlar and Shupe, 2014). However, in particular the lowermost levels, including low-level clouds, are difficult to measure with crewed aircraft, uncrewed aerial vehicles, and ground-based remote sensing. Tethered balloon measurements can probe the whole vertical profile of the ABL starting from the surface, are less affected by icing, and the slow ascent rate enables a high vertical resolution. However, so far no collocated balloon-borne vertical profile measurements of turbulence and radiation have been reported in the Arctic, although the combined analysis is vital for understanding the complex Arctic ABL.

This doctoral thesis introduces a new tethered balloon system for analyzing the vertical structure of turbulence, thermodynamic stratification, and radiation in the Arctic ABL. The central question is how these processes interact in the cloudy Arctic ABL. Observations during the field campaigns Physical Feedbacks of Arctic Boundary Layer, Sea Ice, Cloud and Aerosol (PASCAL) in June 2017 and Polar Airborne Measurements and Arctic Regional Climate Model SImulation Project (PAMARCMiP) in March 2018 provide insights into ABL processes throughout the vertical profile. Two particular phenomena typical for the Arctic ABL are analyzed in detail with a focus on turbulence in stably stratified layers of the ABL. The major outcomes of the present work are:

- The new tethered balloon system *Balloon-bornE moduLar Utility for profilinG the lower Atmosphere* (BELUGA) is introduced. BELUGA enables collocated measurements of turbulent and radiative parameters and energy fluxes up to $1.5\,\mathrm{km}$ height. The payload of BELUGA comprises three modular instrument packages for high-resolution meteorological, turbulence, and broadband radiation measurements. Data processing routines and methods for analyzing local turbulence parameters and turbulent fluxes have been developed. The high vertical resolution is highlighted as a major advantage of tethered balloon-borne observations. During the campaigns, BELUGA has proven its robust performance in cloudy conditions of the Arctic ABL.

- In a first study, I analyze a specific humidity inversion (SHI) above a persistent stratocumulus cloud observed during PASCAL. An in-depth discussion of the problems associated with humidity measurements in cloudy environments leads to the conclusion that the observed SHIs do not result from measurement artifacts, which is a major concern when studying SHIs. I analyze two different scenarios for the SHI in relation to the cloud top capped by a temperature inversion: (i) the SHI coincides with the cloud top, and (ii) the SHI is vertically separated from the cloud top. In both cases, the cloud layer is coupled to the layer above by turbulent mixing. For the first case, several profiles reveal downward virtual sensible and latent heat fluxes at the cloud top, indicating entrainment of humid air from the SHI into the cloud layer. For the second case, the area between cloud top and SHI is supplied with moisture from below and above. The findings support the hypothesis that SHIs above clouds contribute to the longevity of Arctic mixed-phase clouds by supplying moisture to the cloud.

- A second study analyzes the development of a low-level jet (LLJ) in the late-winter stable Arctic ABL during PAMARCMiP. The observed LLJ exhibits a characteristic vertical structure of turbulence. The presence of a LLJ enhances turbulent mixing directly above and below the jet core, compared to a stable ABL without a LLJ. However, a stably stratified constant-wind region close to the surface might decouple the LLJ from the surface. I conclude that a LLJ is capable of enhancing turbulent mixing between the ABL and the surface, provided that

the LLJ base is located at the surface. This can be important for the vertical distribution of substances advected to the Arctic, such as moisture or aerosol particles.

For the two latter studies, I show that turbulent mixing is possible in a particularly stable environment. By vertical mixing of advected substances, turbulence shapes the vertical structure of the ABL in the Arctic. The findings of the two studies provide valuable results to better understand atmospheric processes in the Arctic ABL. Beyond that, the new tethered balloon system sets the stage for a series of observations in the Arctic ABL. Together with upcoming extended measurements and derived model parameterizations, the BELUGA observations of this thesis will contribute to reducing the uncertainties in describing the Arctic climate system.

References

Brooks, I. M., M. Tjernström, P. O. G. Persson, M. D. Shupe, R. A. Atkinson, G. Canut, C. E. Birch, T. Mauritsen, J. Sedlar, and B. J. Brooks (2017). "The turbulent structure of the Arctic summer boundary layer during the Arctic Summer Cloud-Ocean Study". In: *Journal of Geophysical Research: Atmospheres* 122.18, pp. 9685–9704. DOI: 10.1002/2017JD027234.

Sedlar, J. and M. D. Shupe (2014). "Characteristic nature of vertical motions observed in Arctic mixed-phase stratocumulus". In: *Atmospheric Chemistry and Physics* 14.7, pp. 3461–3478. DOI: 10.5194/acp-14-3461-2014.

Sedlar, J., M. Tjernström, A. Rinke, A. Orr, J. Cassano, X. Fettweis, G. Heinemann, M. Seefeldt, A. Solomon, H. Matthes, T. Phillips, and S. Webster (2020). "Confronting Arctic Troposphere, Clouds, and Surface Energy Budget Representations in Regional Climate Models With Observations". In: *Journal of Geophysical Research: Atmospheres* 125.6, e2019JD031783. DOI: https://doi.org/10.1029/2019JD031783.

Smith, D. M., J. A. Screen, C. Deser, J. Cohen, J. C. Fyfe, J. Garcia-Serrano, et al. (2019). "The Polar Amplification Model Intercomparison Project (PAMIP) contribution to CMIP6: investigating the causes and consequences of polar amplification". In: *Geoscientific Model Development* 12.3, pp. 1139–1164. DOI: 10.5194/gmd-12-1139-2019.

Tetzlaff, A., C. Lüpkes, and J. Hartmann (2015). "Aircraft-based observations of atmospheric boundary-layer modification over Arctic leads". In: *Quarterly Journal of the Royal Meteorological Society* 141.692, pp. 2839–2856. DOI: 10.1002/qj.2568.

Wendisch, M., A. Macke, A. Ehrlich, C. Lüpkes, M. Mech, D. Chechin, et al. (2019). "The Arctic Cloud Puzzle: Using ACLOUD/PASCAL Multiplatform Observations to Unravel the Role of Clouds and Aerosol Particles in Arctic Amplification". In: *Bulletin of the American Meteorological Society* 100.5, pp. 841–871. DOI: 10.1175/BAMS-D-18-0072.1.

List of Publications

Part of this thesis

Several text passages and graphics are adapted directly from these papers.

1. **Egerer, U.**, Gottschalk, M., Siebert, H., Ehrlich, A., and Wendisch, M.: The new BELUGA setup for collocated turbulence and radiation measurements using a tethered balloon: first applications in the cloudy Arctic boundary layer, *Atmospheric Measurement Techniques*, 12, 4019–4038, https://doi.org/10.5194/amt-12-4019-2019, 2019.

   For this paper, I was responsible for the turbulence instruments and data analysis. With the support of Holger Siebert, I developed the instruments (sonic anemometer package, hot-wire anemometer package), tested the instruments on a test campaign in Melpitz in winter 2016/17, calibrated individual sensors, and scripted data analysis programs. Together with Matthias Gottschalk, who was in charge of the radiation instruments, we prepared and performed the PASCAL measurements (with the support of many others during the campaign). I post-processed and published the turbulence data and developed the turbulence data analysis methods together with Holger Siebert. Matthias Gottschalk analyzed the radiation data with the support of André Ehrlich and Manfred Wendisch. Matthias Gottschalk and I drafted the paper with support and contributions from all co-authors.

2. **Egerer, U.**, Ehrlich, A., Gottschalk, M., Griesche, H., Neggers, R. A. J., Siebert, H., and Wendisch, M.: Case study of a humidity layer above Arctic stratocumulus and potential turbulent coupling with the cloud top, *Atmospheric Chemistry and Physics*, 21, 6347–6364, https://doi.org/10.5194/acp-21-6347-2021, 2021.

   In this study, I was in charge of analyzing turbulence and humidity data and merging and interpreting the results of the different data sources. I performed the literature study of humidity measurements and re-calibrated the humidity sensor together with Holger Siebert. Both of us developed the methods and ideas to interpret the turbulent exchange. Roel Neggers performed and

analyzed the LES. Hannes Griesche provided the remote sensing data. I drafted the manuscript with contributions from all co-authors.

3. **Egerer, U.**, Siebert, H., Hellmuth, O. and Sørensen, L. L.: The role of a low-level jet for stirring the stable atmospheric surface layer in the Arctic, in preparation for *Journal of Geophysical Research: Atmospheres*.

   For this study, I was responsible for the turbulence instruments and measurements during PAMRACMiP. Holger Siebert and I improved the instruments and prepared the campaign. I was in charge of the 24h measurements, which are the data basis for this paper. Holger Siebert and I developed the research question and drafted the manuscript.

Not part of this thesis

4. Neggers, R. A. J., Chylik, J., **Egerer, U.**, Griesche, H., Schemann, V., Seifert, P., Siebert, H. and Macke, A.: Local and remote controls on Arctic mixed-layer evolution, *Journal of Advances in Modeling Earth Systems*, 11, 2214– 2237, https://doi.org/10.1029/2019MS001671, 2019.

   I contributed to this study by discussing the link between observations and the LES model. In addition, I provided feedback on how the model output fits the observations and was involved in proofreading the manuscript.

5. Wendisch, M., Macke, A., Ehrlich, A., Lüpkes, C., Mech, M., Chechin, D., Dethloff, K., Velasco, C. B., Bozem, H., Brückner, M., Clemen, H., Crewell, S., Donth, T., Dupuy, R., Ebell, K., **Egerer, U.**, Engelmann, R., Engler, C., Eppers, O., Gehrmann, M., Gong, X., Gottschalk, M., Gourbeyre, C., Griesche, H., Hartmann, J., Hartmann, M., Heinold, B., Herber, A., Herrmann, H., Heygster, G., Hoor, P., Jafariserajehlou, S., Jäkel, E., Järvinen, E., Jourdan, O., Kästner, U., Kecorius, S., Knudsen, E. M., Köllner, F., Kretzschmar, J., Lelli, L., Leroy, D., Maturilli, M., Mei, L., Mertes, S., Mioche, G., Neuber, R., Nicolaus, M., Nomokonova, T., Notholt, J., Palm, M., van Pinxteren, M., Quaas, J., Richter, P., Ruiz-Donoso, E., Schäfer, M., Schmieder, K., Schnaiter, M., Schneider, J., Schwarzenböck, A., Seifert, P., Shupe, M. D., Siebert, H., Spreen, G., Stapf, J., Stratmann, F., Vogl, T., Welti, A., Wex, H., Wiedensohler, A., Zanatta, M., and Zeppenfeld, S.: The Arctic Cloud Puzzle: Using ACLOUD/PASCAL Multiplatform Observations to Unravel the Role of Clouds and Aerosol Particles in Arctic Amplification, *Bulletin of the American Meteorological Society*, 100(5), 841-871, https://doi.org/10.1175/BAMS-D-18-0072.1, 2019.

Here, I contributed with a text passage describing the BELUGA setup, the turbulence instruments, and two measurement examples. I also participated in proofreading the paper.

6. Siebert, H., Szodry, K., **Egerer, U.**, Wehner, B., Henning, S., Chevalier, K., Lückerath, J., Welz, O., Weinhold, K., Lauermann, F., Gottschalk, M., Ehrlich, A., Wendisch, M., Fialho, P., Roberts, G., Allwayin, N., Schum, S., Shaw, R. A., Mazzoleni, C., Mazzoleni, L., Nowak, J. L., Malinowski, S. P., Karpinska, K., Kumala, W., Czyzewska, D., Luke, E. P., Kollias, P., Wood, R., and Mellado, J. P.: Observations of Aerosol, Cloud, Turbulence, and Radiation Properties at the Top of the Marine Boundary Layer over the Eastern North Atlantic Ocean: The ACORES Campaign, *Bulletin of the American Meteorological Society*, 102(1), E123-E147., https://doi.org/10.1175/BAMS-D-19-0191.1, 2021.

   For this paper, I supported the ACTOS turbulence measurements.

Committees

Doctorate commission

Prof. Dr. Johannes Quaas (chairman)
Institute for Meteorology, University of Leipzig, Leipzig, Germany

Prof. Dr. Manfred Wendisch (supervisor)
Institute for Meteorology, University of Leipzig, Leipzig, Germany

Prof. Dr. Andreas Macke
Leibniz Institute for Tropospheric Research, Leipzig, Germany

Supervision committee

Prof. Dr. Manfred Wendisch
Institute for Meteorology, University of Leipzig, Leipzig, Germany

Dr. Holger Siebert
Leibniz Institute for Tropospheric Research, Leipzig, Germany

Dr. André Ehrlich
Institute for Meteorology, University of Leipzig, Leipzig, Germany

Declaration of primary authorship

I hereby declare that the present dissertation "A new set of tethered balloon-borne instrument payloads for collocated turbulence and radiation measurements in the cloudy Arctic boundary layer – first applications" has been prepared by myself without any unauthorized assistance and without the use of any aids other than those indicated. The ideas taken directly or indirectly from external sources have been identified as such in the work.

I affirm that other persons - apart from the persons named in the publication list - were not involved in the intellectual production of the present thesis. No assistance of an external advisor or other persons receiving direct or indirect monetary benefits was used.

I confirm that the submitted thesis or parts thereof have not been submitted in the same or similar form to any other examination authority for the purpose of a doctorate or any other examination procedure, either in Germany or abroad. No earlier unsuccessful attempts at a doctoral degree have taken place.

Leipzig, 16.06.2021

U. Egerer

Acknowledgements

Completing this work would not have been possible without the support of an amazing network of inspiring people. To all of them, I would like to express my deepest gratitude.

- First, thank you to my supervisors for the tremendous support throughout the last years. Holger Siebert introduced me to the field of atmospheric turbulence, was always receptive to my concerns, guided me through all kinds of challenges, and created a pleasant work environment. Manfred Wendisch had always some motivating words and gave valuable strategic advice.

- The thesis was funded by the project "ArctiC Amplification: Climate Relevant Atmospheric and SurfaCe Processes, and Feedback Mechanisms *(AC)*^{3}". The *(AC)*^{3} community enriched both my personal and professional development, accompanying me through all stages of the PhD work.

- All of the fieldwork would have been impossible without help of others. Special thanks to Matthias Gottschalk, Kai Szodry, Felix Lauermann, and Thomas Conrath (the core balloon team during PASCAL), and the Polarstern crew and scientists. During PARMARCMiP, I worked closely with Holger Siebert, Jens Voigtländer, and Zhouxing Zou, and the 24-hour experiment received tremendous support from numerous scientists and the Station Nord soldiers.

- The TROPOS cloud group became my second home during the PhD project. Thank you so much for the entertaining coffee and lunch breaks. Special thanks to my amazing office colleagues Silvia Henning, Thomas Conrath, and Markus Hartmann.

- My fellow PhD students made the time at TROPOS a fun and extraordinary experience, including climbing trips, Tropobatics training, and barbecues. Many thanks to Markus (also for proofreading parts of the thesis), Steffi, Sebastian Z., and many more.

- Many skills and competences I owe to my former Diplom supervisor Jürgen Frey, who awakened my interest in airborne measurements, and Akaflieg Dresden.

- The past five years had many ups and downs, and especially during hard times, I appreciated my family in the background who is there whenever needed. Thanks to my parents and grandparents for supporting any extraordinary idea. Thanks to Binski for providing topical feedback on top of emotional care.
- Thank you to my friends for making my life beyond work so exciting and versatile.
- To Sebastian S.: Thank you for making the unthinkable become reality.